Colloidal Quantum Dots and J-Aggregating Cyanine Dyes for Infrared Photodetection

Thesis advisor

Vladimir Bulović, Federico Capasso

Author

Timothy Paul Osedach

Colloidal Quantum Dots and J-Aggregating Cyanine Dyes for Infrared Photodetection

Abstract

The emergence of nanostructured semiconducting materials enables new approaches toward the realization of photodetectors that operate in the technologically important near- and short-wave infrared (NIR and SWIR) spectral ranges. In particular, organic semiconductors and colloidal quantum dots (QDs) possess numerous advantages over conventional crystalline semiconductors including highly tunable optical and electronic characteristics, the prospect for low-temperature processing, and compatibility with inexpensive and flexible substrates. Photodetectors based on such materials may lead to low-cost IR focal plane arrays for night-vision imaging as well as a multitude of novel applications in biological and chemical sensing. This thesis describes the development and detailed characterization of several photodetectors that incorporate colloidal QD and organic semiconductor thin films as active layers. The electronic properties of PbS QDs are thoroughly investigated in a field effect transistor (FET) geometry and several QD-based photoconductive structures exhibiting SWIR photosensitivity are demonstrated. We describe a novel QD-sensitized lateral heterojunction photoconductor in which the functions of optical absorption and charge transport are dissociated into different physical layers that can be indepen-

dently optimized. This structure is advantageous because it obviates the need for aggressive chemical treatments to the QD film that may compromise the quality of QD surface passivation. Photovoltaic device architectures are addressed, noting their advantages of being operable without an external applied bias and at fast response speeds. We present detailed experimental and theoretical characterization of a photovoltaic structure that is sensitized at NIR wavelengths by a J-aggregating cyanine dye. The high absorption coefficient of the J-aggregate film, combined with the use of a reflective anode and optical spacer layer, enables an external quantum efficiency (EQE) of $16.1 \pm 0.1\%$ ($\lambda = 756$ nm) to be achieved at zero-bias in a device that incorporates an 8.1 ± 0.3 nm-thick dye film. The merits and drawbacks of the various device architectures and nanostructured material systems are discussed and the outlook for nanostructured photodetectors that exhibit infrared sensitivity is presented.

Contents

List of Figures

List of Tables

Citations to Previously Published Work

Most of Chapter 4 is published as:

> "Interfacial Recombination for Fast Operation of a Planar Organic/QD Infrared Photodetector", T. P. Osedach, N. Zhao, S. M. Geyer, L.-Y. Chang, D. D. Wanger, A. C. Arango, M. G. Bawendi and V. Bulović, Adv. Mat. **22**, 5250–5254 (2010)

Chapter 5 is in preparation as:

> "Bias-Stress Effect in 1,2-Ethanedithiol-Treated PbS Quantum Dot Field Effect Transistors", T. P. Osedach, N. Zhao, T. L. Andrew, P. R. Brown, D. D. Wanger, D. B. Strasfeld, L.-Y. Chang, M. G. Bawendi, V. Bulović, in preparation

Chapter 6 appears in its entirety as:

> "Lateral heterojunction photodetector consisting of molecular organic and colloidal quantum dot thin films", T. P. Osedach, S. M. Geyer, J. C. Ho, A. C. Arango, M. G. Bawendi and V. Bulović, Appl. Phys. Lett. **94**, 043307 (2009)

Chapter 7 is in preparation as:

> "Near-Infrared Photodetector Consisting of J-Aggregating Cyanine Dye and Metal Oxide Thin Films", T. P. Osedach, A. Iacchetti, R. R. Lunt, T. L. Andrew, P. R. Brown, G. M. Akselrod, V. Bulović, in preparation

Acknowledgments

The work presented herein was conducted in the Organic and Nanostructured Electronics Laboratory (ONElab) at M.I.T. from June of 2007 to December of 2011. I would gratefully like to acknowledge financial support from the National Science Foundation Graduate Research Fellowship Program as well as the Link Foundation Energy Fellowship Program. The M.I.T. Institute for Soldier Nanotechnologies (ISN) also contributed essential support in terms of funding and experimental shared user facilities. I also made use of the shared user facilities at the Center for Materials Science and Engineering (CMSE) and Microsystems and Technology Laboratory (MTL).

This thesis would not have been possible without the support of a great many people. I first and foremost thank my advisor Prof. Vladimir Bulović for creating such a friendly and positive environment in which to work. His guidance, feedback and unwavering support were critical to the completion of this thesis. It has been a great privilege to work with such an excellent role model of a scientist, teacher and leader. It is also a pleasure to thank my co-advisor, Prof. Federico Capasso, for supporting my research at M.I.T. and providing critical feedback and encouragement. His passion for device physics has been a great source of inspiration. I always left discussions with new insights about my experiments and re-energized about addressing the challenges presented by my research. I am sincerely thankful to Prof. Moungi Bawendi for openly welcoming me into his group as a collaborator and for showing tremendous interest and support for my research. His detailed understanding of the underlying physics and the experimental aspects related to working with quantum dots was vital to much of this work. My thesis committee member, Prof. Marko Loncar, also contributed useful discussions and feedback to this work. His friendly correspondence

and genuine interest in my research was a tremendous source of encouragement.

I am indebted to all of the students and post-docs of ONElab who I have worked with over the years. It has been an immense honor to work with so many truly outstanding colleagues, each of whom contributed in unique ways to making the lab a stimulating and enjoyable place to work. In particular, I would like to thank Alexi Arango, who initially welcomed me into the group and attentively mentored me on my projects early on. His passion for solar energy as well as his dedication to the improvement and maintenance of the laboratory continues to inspire me. My good fortune to share an office with him for many years has certainly shaped me into a better person. Johnny Lunt provided crucial guidance on the planning of my projects as well my career. From now on, whenever I encounter a difficulty in the lab I shall think to myself, "let's put a multimeter on it." I am greatly indebted to Ni Zhao, who mentored me through many difficult research challenges and helped me remember to find time to have fun. I am also greatly indebted to Trisha Andrew for brightening up the lab with her unique sense of humor and for her mentorship during my final stretch of graduate school. Finally, I would like to thank Angela Glass and Monica Pegis for handling the vital logistical and administrative activities that made this work possible.

I also would like to extend my thanks to the many collaborators I've had the pleasure of working with over the years including the students and post-docs of the Bawendi group, who synthesized most of the QD materials used in this work. I would particularly like to thank Scott Geyer and Darcy Wanger for experimental support related to working with quantum dots, as well as for many useful discussions

and detailed feedback on my work. I would also like to thank our visiting student Antonio Iacchetti for his support with experiments and for sharing his wisdom about organic photodetectors.

I am grateful to my undergraduate advisors, Prof. Robert Krchnavek and Prof. Peter Jansson, whose passion for teaching and dedication to science are largely what inspired me to undertake this endeavor. Their continued encouragement, guidance and friendship have been a critical source of support. I am also grateful to my classmates and friends who I shared this journey with. In particular, I would like to thank Sasha Stolyarov, Alex Nemiroski and the M.I.T. Isshinryu Karate club.

Finally, I would like to thank my parents, Maureen and Paul, and my siblings, Jessica and Derek, for their patience and support throughout this process.

Dedicated to my father Paul,
my mother Maureen,
my sister Jessica,
and my brother Derek.

Chapter 1

Introduction

Although invisible to the human eye, infrared radiation is critically important to a number of industrial, scientific and medical applications. This thesis explores the use of emerging nanostructured materials to realize photodetectors that are sensitive in the near- and short-wave infrared (NIR and SWIR) spectral ranges. The specific materials that are addressed include colloidal nanocrystal "quantum dots" and J-aggregating cyanine dyes. These materials offer many advantages that are attractive for photodetection, including highly tunable optical characteristics, the prospect for low-temperature processing, and compatibility with inexpensive and flexible substrates. The goals of this thesis are two-fold: (1) The detailed characterization of nanostructured materials of interest, in order to elucidate the fundamental physics that govern their electronic and optical properties, and (2) the experimental integration of these nanostructured materials into novel photodetector device structures. In this chapter, we review the development and recent advances in nanostructured NIR/SWIR infrared photodetection and present an overview of this thesis.

1.1 Overview of Nanostructured Photodetectors

This thesis concerns nanostructured materials that meet the following criteria: (1) Consist of thin semiconducting films (<2 μm), (2) incorporate nanometer-scale materials with excitonic or quantum-confinement character and (3) can be fabricated entirely with low-temperature (< 300 °C) processing techniques, such as solution-processing or low-temperature thermal sublimation. Encompassed under this definition are organic semiconductors and several inorganic materials, including colloidal nanocrystal quantum dots (QDs) and nanowires. These materials exhibit several characteristics that make them highly attractive for use in optoelectronic devices [44, 31]. In particular, their optical and electronic properties are often highly tunable, enabling them to be engineered to suit specific applications. They also offer the prospect for inexpensive processing over large areas and onto arbitrary substrates, including flexible substrates such as plastic and paper [45].

In the past several decades, research into utilizing nanostructured materials for optoelectronic device applications has primarily focused on light-emitting diodes for lighting and displays [46], and photovoltaic cells for solar energy harvesting [47, 48]. Indeed, these efforts have made impressive advances. OLED displays are becoming increasingly common-place in consumer electronics ranging from cell phones to televisions and nanostructured solar cells with power conversion efficiencies approaching 10% have been reported [49, 50, 51, 52].

It has only been in the past decade that interest in utilizing these materials for photodetection has emerged as an active area of research in industry and academia. Early reports highlighted their many advantages for photodetection [53, 54, 55, 56],

among which are the ability to engineer active layer materials to target specific wavelengths, short optical absorption lengths ($1/\alpha < 100$ nm) enabling ultra-thin device structures (and therefore potentially fast response speeds), and facile integration with silicon electronics as well as inexpensive and flexible substrates [57].

More recently, interest in these devices has increased in proportion with progress in the exploration of nanostructured materials that exhibit sensitivity in the NIR and SWIR spectral ranges (defined here to span 0.7-1.0 μm and 1.0-3.0 μm, respectively). Materials that are absorptive in these ranges are highly attractive for photovoltaics, as they enable harvesting of the considerable solar energy that lies beyond visible wavelengths. Such materials are also attractive for photodetection, however, where they can potentially be employed in a multitude of applications [58].

The most common uses for NIR/SWIR photodetection include optical communication [59] and a variety of imaging applications [1, 2]. Several examples of NIR and SWIR imaging are shown in Figure 1.1. Many of these applications presently rely on expensive epitaxially-grown photodetector structures, such as the InGaAs p-i-n photodiode [60]. The development of low-cost alternatives to such crystalline inorganic structures may therefore greatly expand the scope of applications for infrared photodetection. For example. several major automobile companies are exploring the use of infrared imagers (ordinarily reserved mostly for military applications) to improve a driver's ability to detect obstacles (animals, pedestrians, cyclists, etc.) at night [2, 3]. Low-cost nanostructured imagers may enable this vision to become widely implemented.

The unique attributes of nanostructured materials also suggest entirely new areas

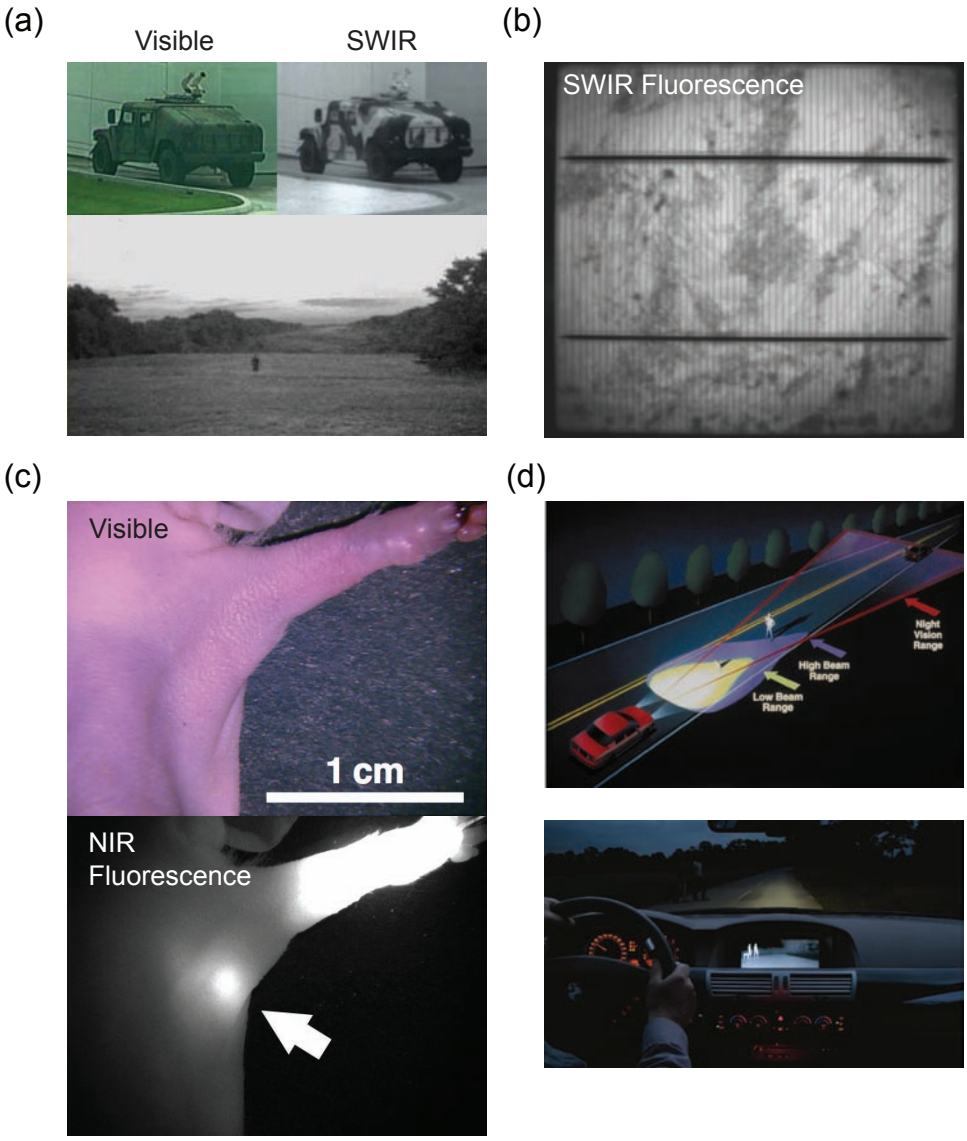

Figure 1.1: (a) Top: visible versus SWIR imaging of camouflaged vehicle. Bottom: SWIR night vision image of a man standing in a field in total darkness on a moonless night (from Goodrich Corporation). (b) SWIR fluorescence imaging for inspection of defects on silicon photovoltaic module (from Goodrich Corporation). (c) Imaging of NIR-emitting quantum dots in an animal specimin (from Ref. [1]). (d) Top: Schematic illustrating the use of night vision to augment the visual range of drivers (from Ref. [2]). Bottom: Depiction of dashboard night vision for automobiles (from Ref. [3]).

of application. The ability to inexpensively fabricate devices over large areas, for example, may enable the realization of next-generation medical instruments for X-ray imaging [61, 62]. On the other hand, the ability to readily integrate devices onto a variety of substrates has inspired reports on a wide range of biological [63, 64] and chemical sensing [65, 66, 67] modalities, including lab-on-a-chip devices for point-of-care medical diagnostics [68].

Typical photodetector device structures consist of thin films (usually less than 200 nm-thick) of nanostructured materials incorporated into planar photoconductor or sandwich-type photodiode configurations (i.e. donor/acceptor heterojunction or Schottky). Reported devices have incorporated a wide variety of nanostructured materials, including small molecules, polymers, carbon nanotubes and QDs. The chemical structures for several specific materials are shown Figure 1.2.

In some of these reports, the photosensitivity metric of specific detectivity (D^*) has exceeded 10^{12} Jones, thus rivaling conventional inorganic technologies such as the crystalline silicon photodiode [23, 18]. In the case of QD photoconducting structures, these advances were attained largely through the engineering of QD surface state passivation in order to maximize photoconductive gain [23, 69]. As a consequence, these devices exhibit very slow response speeds. In the case of photodiodes, photosensitivity is often limited by the electrical noise intrinsic to the device. In some systems, the use of organic "blocking layers" to significantly reduce dark current has enabled this limitation to be surmounted [29, 18]. In general, photoconductors enable higher overall photosensitivity, but photodiodes are advantageous as they can be operated low or zero-bias, and at much faster speeds. The characteristics of several organic-

based and QD-based photodetector structures are tabulated in Tables 1.1 and 1.2, respectively.

1.2 Overview of Thesis

This thesis describes the development and detailed characterization of several photodetectors that are optically sensitized by thin films of nanostructured materials. The specific materials that are addressed include colloidal QDs and J-aggregating cyanine dyes. An overview is as follows:

Chapter 2 reviews the underlying physics that describe the optical and electronic properties of various nanostructured materials, including organic semiconductors and colloidal QDs. The basic operation of the devices architectures described in this thesis are also discussed, including field-effect transistors (FETs), photoconductors and photodiodes. Chapter 3 describes the various fabrication and device characterization techniques that were employed in this work.

In Chapter 4, PbS QD-based photoconductors sensitive at SWIR wavelengths are introduced and several approaches for improving their performance characteristics described. In Chapter 5, the charge transport characteristics of PbS QD films are thoroughly characterized in an FET geometry, including a detailed study of the bias-stress effect in this system. Chapter 6 describes a novel lateral heterojunction photoconductor, in which the functions of charge transport and optical absorption are dissociated into different physical layers. Chapter 7 describes a photodiode structure that is optically sensitized in the NIR by a J-aggregating cyanine dye. Finally, a summary is presented in Chapter 8, as well as an outlook for nanostructured pho-

todetectors that exhibit infrared sensitivity.

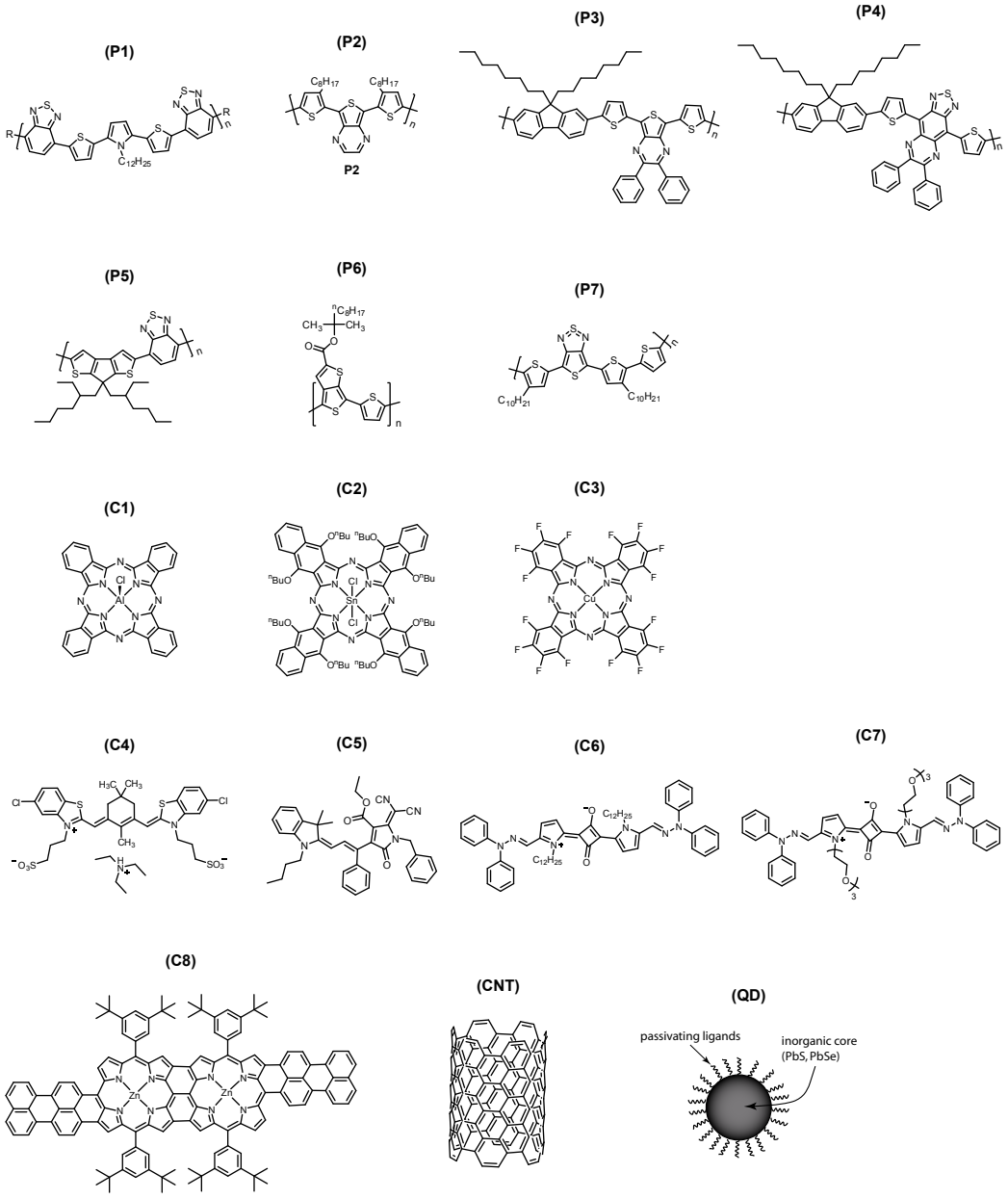

Figure 1.2: Variety of nanostructured materials with NIR or SWIR absorption that have been utilized as active materials in photodetector device structures: **(P1)** PTPTB [4]. **(P2)** PB30TP [5]. **(P3)** APFO-Green1 [6]. **(P4)** APFO-Green2 [7]. **(P5)** PCPDTBT [8] **(P6)** PTT [9]. **(P7)** PDDTT [10]. **(C1)** ClAlPc [11]. **(C2)** Cl_2SnNc [12]. **(C3)** $F_{16}CuPc$ [13, 14]. **(C4)** J-aggregating cyanine dye, U3 [15]. **(C5)** Merocyanine dye [16]. **(C6)** Alkyl functionalized squaraine, AlkSQ [17]. **(C7)** Glycol functionalized squaraine, GlySQ [18]. **(C8)** Zinc porphyrin, Pfused [19, 20]. **(CNT)** Carbon nanotube [21]. **(QD)** Schematic of a PbS [22, 23, 24, 25, 26, 27] or PbSe [28, 29, 30] quantum dot.

Table 1.1: Performance characteristics of nanostructured photodetector structures that are sensitized at NIR/SWIR wavelengths by organic semiconductors.

Material System[a]	**Type**[b]	**Year**	λ [nm]	V_{bias} [V]	EQE (λ) [% (nm)]	D^* [cm $\text{Hz}^{1/2}$ W^{-1}]	f_{3dB} or τ_{fall}[c]
P1/$PC_{61}BM$	PD	2002 [4]	400-800	0	2 (700)	-	-
P4:$PC_{61}BM$	PD	2005 [7]	400-800	0	8 (700)	-	-
P2/$PC_{61}BM$	PD	2005 [5]	400-900	0	3 (800)	-	-
P3/BTPF70	PD	2005 [6]	600-1000	0	9 (800)	-	-
P5/$PC_{71}BM$	PD	2007 [8]	400-1000	0	33 (710)	-	-
P6/$PC_{61}BM$	PD	2007 [9]	400-1000	0	19 (850)	-	1-4 MHz
CNT:P3HT/C_{60}	PD	2009 [21]	400-1450	-0.7	2.0 (1300)	1×10^{10}	7.2 ns
P7/$PC_{61}BM$	PD	2009 [10]	300-1450	0	26 (800)	2.1×10^{10}	-
C6	PC	2009 [17]	600-950	60	200 (670)	-	3 ms
C8/C_{60}	PD	2010 [19]	400-1400	0	6.5 (1350)	2.3×10^{10}	2.1 ns
C2/C_{60}	PD	2010 [12]	800-1100	0	17 (1000)	-	-
C5/$PC_{71}BM$	PD	2010 [16]	400-850	0	16 (750)	-	-
C3/CuPc	PD	2011 [13]	550-850	-9	9.2 (808)	4.6×10^{10}	80 ns
C7/$PC_{61}BM$	PD	2011 [18]	400-850	-1	15 (700)	3.4×10^{12}	1 MHz
C8:Bipy:$PC_{61}BM$/C_{60}	PD	2011 [20]	900-1500	0	10.5 (1400)	8.2×10^{10}	-
C3:PTCDI-C8/TiOPc	PD	2011 [14]	200-900	-3	20 (900)	1×10^{12}	56 ns
C4/ZnO	PD	2012 [15]	500-800	0	16 (756)	4.3×10^{11}	91.5 kHz

[a] Includes the active materials in the device structure. Electrodes, blocking layers and injection layers are not indicated. $PC_{61}BM$ = phenyl C_{61} butyric acid methyl ester. BTPF70 = 3'-(3,5-bis-tri-fluoromethylphenyl)-1'-4-nitrophenyl)pyrazolino[70]fullerene. $PC_{71}BM$ = phenyl C_{71} butyric acid methyl ester. P3HT = poly(3-hexylthiophene). CuPc = copper phthalocyanine. Bipy = 4-4'-Bipyridyl. PTCDI-C8 = N,N'-Dioctyl-3,4,9,10-perylenedicarboximide. TiOPc = oxo-titanium phthalocyanine.

[b] "PD" indicates a photodiode structure and "PC" indicates a photoconductor.

[c] τ_{fall} is the time constant describing the decay of photocurrent following a short pulse of illumination. f_{3dB} is the frequency of modulated light at which the photodetector response is attenuated by 3 dB.

Table 1.2: Performance characteristics of nanostructured photodetector structures that are sensitized at NIR/SWIR wavelengths by colloidal quantum dots.

Material System[a]	**Type**[b]	**Year**	λ [nm]	V_{bias} [V]	EQE (λ) [% (nm)]	D^* [cm $\text{Hz}^{1/2}$ W^{-1}]	f_{3dB} or τ_{fall}[c]
PbS **QD**:MEH-PPV	PD	2005 [22]	400-1600	-5	0.39 (975)	-	-
PbS **QD**	PC	2006 [23]	400-1500	100	1240 (1300)	1.8×10^{13}	<20 Hz
PbS **QD**:P3HT	PD	2006 [28]	400-2200	0	0.006 (1950)	-	-
PbS **QD** (Schottky) [d]	PD	2009 [24]	400-1700	0	16.5 (1450)	1×10^{12}	1.5 MHz
PbS **QD**/PCBM	PC	2009 [25]	400-1300	15	33 (1200)	-	>2 s
PbS **QD**:P3HT:$PC_{61}BM$	PD	2009 [26]	400-1800	-5	16.5 (1220)	2.3×10^{9}	2.5 kHz
PbSe **QD**/ZnO	PD	2011 [29]	600-1300	-0.5	2 (1220)	1×10^{11}	-
PbS **QD**/TiO_2	PD	2011 [27]	400-1400	0	28 (1250)	-	-
PbSe **QD**/ZnO	PD	2011 [30]	400-1600	0	38 (1550)	-	-

[a] Includes the active materials in the device structure. Electrodes, blocking layers and injection layers are not indicated. MEH-PPV = poly(2-methoxy-5-(2'-ethylhexyloxy)-*p*-phenylenevinylene). P3HT = poly(3-hexylthiophene). $PC_{61}BM$ = phenyl C_{61} butyric acid methyl ester.

[b] "PD" indicates a photodiode structure and "PC" indicates a photoconductor.

[c] τ_{fall} is the time constant describing the decay of photocurrent following a short pulse of illumination. f_{3dB} is the frequency of modulated light at which the photodetector response is attenuated by 3 dB.

[d] The reported value for D^* was measured at T = 250 K.

Chapter 2

Background

In this chapter, we introduce the various nanostructured materials and device structures that were utilized in this work. Overviews of organic semiconductors, J-aggregating cyanine dyes, and colloidal quantum dots are presented. We then review the basic operation of field effect transistors, photoconductors and heterojunction photodiodes, in preparation for more specific discussion in later chapters.

2.1 Organic Semiconductors

2.1.1 Basic Optical and Electronic Properties

Organic semiconductors of interest for optoelectronic device applications generally fall into one of two categories: (1) aromatic hydrocarbons and (2) conjugated polymers. The former are low molecular weight materials that contain benzene rings in their structure. The latter are macromolecules that consist of repeating monomeric sub-units along a conjugated backbone. Many of the materials used in this thesis

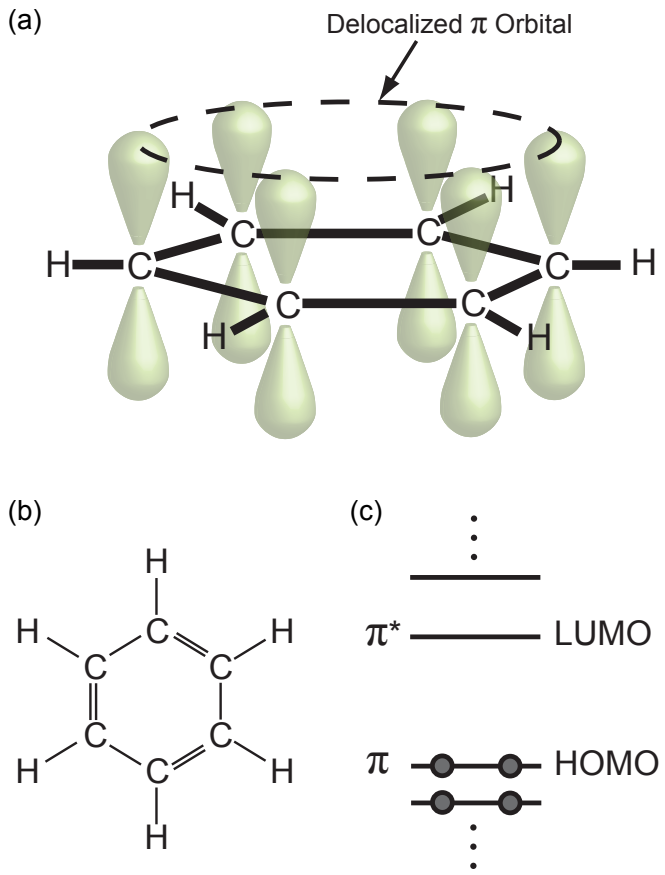

Figure 2.1: (a) Schematic depicting delocalized π orbitals above and below the plane of the carbon ring (adapted from Ref. [31]) (b) Chemical structure of a benzene ring. (c) Energy band diagram showing HOMO and LUMO energy levels.

fall in the former category. The molecule, spiro-TPD (discussed in Chapter 6), for example, is an aromatic hydrocarbon.

The key attribute that these material systems have in common is that they possess conjugated bonds in their structure that give rise to large delocalized electronic orbitals. This is illustrated in Figure 2.1 with the example of a benzene ring, the simplest aromatic hydrocarbon. In each of the six carbon atoms in the ring, three of the four valence electrons form sp_2-hybridized orbitals at 120° angles from one

another in the plane of the molecule. These orbitals directly overlap with the orbitals of adjacent hydrogen and carbon atoms, resulting in strong covalent bonds, called σ bonds. The fourth valence electron, in contrast, occupies a p_z orbital that extends out of the plane of the benzene ring. The side-to-side overlap of adjacent p_z orbitals from adjacent carbon atoms results in the formation of relatively weak π bonds between them. This is represented schematically by alternating single and double bonds in the benzene ring (see Figure 2.1(b)). In reality, the π bonds between adjacent carbon atoms are equally distributed and constitute a continuous "π-system" that is delocalized around the entirety of the ring. This π-system may be delocalized even further in larger molecules with a greater extent of conjugation.

In an energy band diagram describing the levels of the various electronic states in the molecule, the highest occupied state, referred to as the highest occupied molecular orbital (HOMO), and lowest unoccupied state, referred to as the lowest unoccupied molecular orbital (LUMO), are attributed to the ground and excited states of these relatively weakly-bound π electrons (Figure 2.1(c)). The difference between the HOMO and LUMO energy levels is generally well-defined for a given molecule and can be thought of as an optical band gap. The absorption of a photon with greater than the HOMO-LUMO energy, for example, can excite a π electron to a π^* excited state, forming an exciton, or bound electron-hole pair, on the molecule. In many organic materials, this transition can occur at visible or even infrared wavelengths.

2.1.2 Organic Thin Films

Films of organic materials are usually prepared in the solid state by either solution processing or thermal sublimation. These techniques are described in detail in Chapter 3. Organic semiconductors in the solid state are generally amorphous, with neighboring molecules held together only by weak van der Waals induced-dipole interactions. As a result, these solids are often soft, easily deformable and have low melting points. Moreover, they tend to be susceptible to degradation caused by oxygen and water in the atmosphere.

Since their electronic and vibrational states remain localized near individual molecules, the optical properties of the solid-state film are usually very similar to those of individual molecules. Electrical conduction is only possible because of the partial overlap of π wavefunctions of neighboring molecules. Carrier mobilities of organic semiconductors are generally lower than in inorganic semiconductors and depend on their particular molecular packing morphology. For example, an amorphous film of spiro-TPD, which is a hole transporting material used in organic solar cells [70] and light emitting diodes [71], exhibits a hole mobility of $\approx 10^{-4}$ $\mathrm{cm^2V^{-1}s^{-1}}$. Field-effect mobilities in the range of 1-20 $\mathrm{cm^2V^{-1}s^{-1}}$ have been achieved, however, in single crystals of organic materials such as pentacene [72] and rubrene [73].

Despite their inferior electrical characteristics and issues with stability, the many advantages of organic semiconductors have driven intense interest in employing them in a wide range of applications. These advantages include high optical absorption coefficients, a high degree of optical and electronic tunability (afforded by the wide variety of available materials), inexpensive low-temperature processing, and compat-

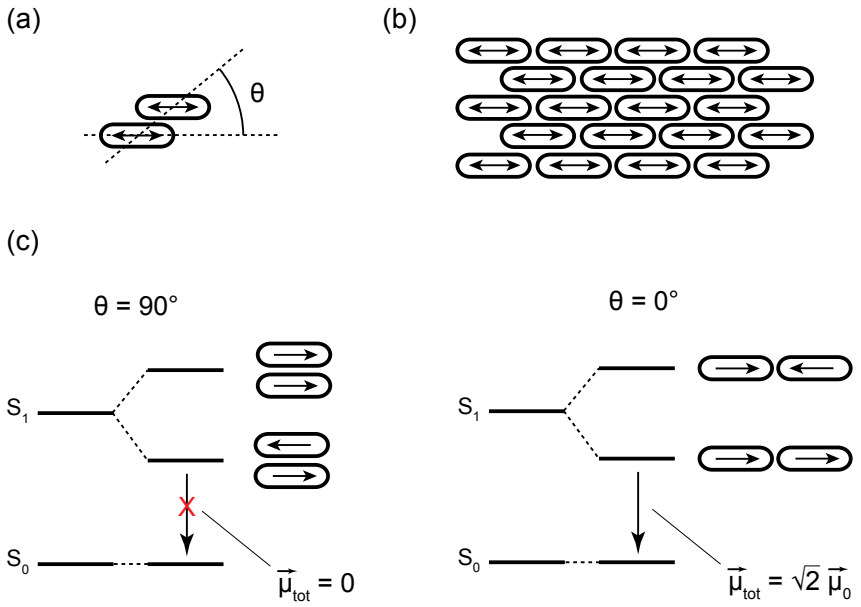

Figure 2.2: (a) Definition of slipping angle between two adjacent dye molecules. (b) Illustration of brickwork pattern of molecules. (c) Illustration of band-splitting for two coupled molecules for different slipping angles (adapted from Ref. [32]).

ibility with flexible and large-area substrates.

2.1.3 J-Aggregating Cyanine Dyes

Molecules from a unique class of organic materials tend to form supramolecular aggregates with optical transition dipole moments that are larger than those of the constituent molecules themselves. This phenomenon was independently discovered over 70 years ago by E. Jelley [74] and G. Scheibe [75] in aqueous solutions of the dye, pseudoisocyanine chloride (PIC chloride). Such aggregating dyes later found use in the photographic film industry throughout the 20$^{\text{th}}$ century [76, 77, 78, 79]. In honor of their inventors, these materials are today referred to as "J-aggregates" or "Scheibe aggregates".

J-aggregates are characterized by very high absorption coefficients and narrow absorption features that are red-shifted with respect to their monomeric absorption spectra. The new absorption band is referred to as the "J-band". A related type of aggregate is the "H-aggregate", in which the absorption feature is blue-shifted relative to the monomeric absorption spectrum. Here, "H" denotes a hypsochromic shift of the absorption feature.

To understand the origin of the unique spectral changes that arise with aggregation, we consider the interaction of two neighboring dye molecules, as in Ref. [32]. When the two molecules are brought into close proximity with one another, their dipole moments couple, resulting in a splitting of their excited states. The oscillator strength of these states is expected to depend on the geometry of the aggregate, as quantified by the "slipping angle", defined in Figure 2.2(a). For dipoles that are aligned tip-to-tail (slipping angle of $0\,^{\circ}$), the higher energy state will correspond to when the two dipoles are oscillating out of phase while the lower energy state will correspond to when the dipoles are oscillating in phase (see Figure 2.2(c)). In the case of the higher energy state, the two dipoles cancel each other resulting in a net dipole moment of zero. The dipole moment of the lower (red-shifted) energy state, however, is increased by a factor of $\sqrt{2}$.

This analysis can be extended to a larger system of N interacting dipoles. The J-band in this case corresponds to a situation in which all of the N molecules are oscillating in phase. The dipole strength can be estimated according to the equation [32]:

$$\mu^2_{J-Agg} \approx 0.81(N+1)\mu^2_m \tag{2.1}$$

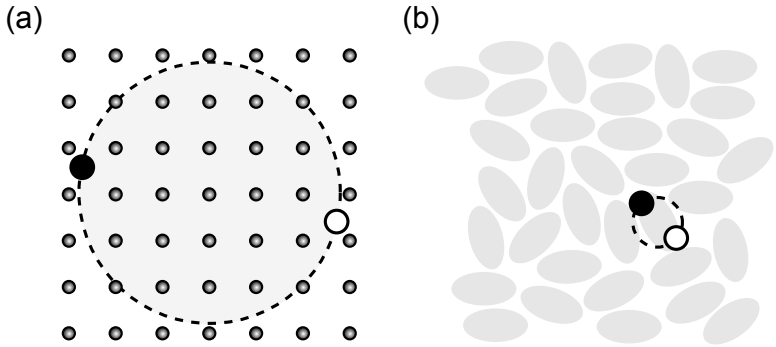

Figure 2.3: Schematic depicting (a) a Wannier-Mott exciton in a crystal lattice and (b) a Frenkel exciton tightly bound to a single molecule (adapted from Ref. [31]).

μ_m is the dipole strength of a monomer and μ_{J-Agg} is the dipole strength of the J-aggregate.

In an actual film, the slipping angle will likely not be at 0 °, but at some intermediate angle, resulting in a "brickwork" arrangement like that shown in Figure 2.2(b). A photodiode that is optically sensitized by a thin film of a J-aggregating cyanine dye is described in Chapter 7.

2.1.4 Wannier-Mott and Frenkel Excitons

Electrons and holes in a semiconductor may become bound by their mutual Coulomb interaction to form a quasi-particle known as an "exciton". An exciton may be thought of as an electron and hole orbiting around each other in the semiconducting material with some radius, a_x and binding energy, E_b. These characteristics are strongly influenced by the dielectric environment. In materials with high dielectric constants (ϵ_r >10), screening of the Coulomb interaction results in a large exciton radius and low binding energy. In this case the exciton may extend over many atomic sites in a crystal lattice as shown in Figure 2.3(a). These are referred to as "Wannier-

Mott" excitons and are mainly observed in inorganic semiconducting materials. They are typically characterized by binding energies on the order of 0.01 eV, making them unstable at room temperature due to phonon collisions.

In materials with lower dielectric constants, such as organic semiconductors ($\epsilon_r \approx$ 3-4), the extent of dielectric screening is much less, resulting in a more tightly-bound exciton called a "Frenkel" exciton. In this case, the exciton may be confined to a single molecule, as shown in Figure 2.3(b). The binding energies of Frenkel excitons are in the range of 0.1-1 eV, depending on the material. They are therefore stable at room temperature. The dynamics of Frenkel excitons are of paramount concern to the design of organic optoelectronic devices. This will be discussed further in Section 2.5.

2.2 Colloidal Quantum Dots

Quantum dots (QDs) are a type of low-dimensional nanostructure in which carriers are confined in three dimensions. There are numerous approaches to fabricating such structures, including chemical synthesis [33, 80] and a variety of epitaxial techniques [81, 82]. In this thesis, however, we are concerned specifically with chemically synthesized nanocrystal QDs that are processable from solution. The optical properties of quantum dots may be strongly influenced by the quantum confinement effect, giving rise to new properties that are not present in the corresponding bulk material. Of particular interest to this work is the prospect for tunable absorption across near- and shortwave infrared wavelengths. In this section, the synthesis and basic optical characteristics of nanocrystal QDs are reviewed.

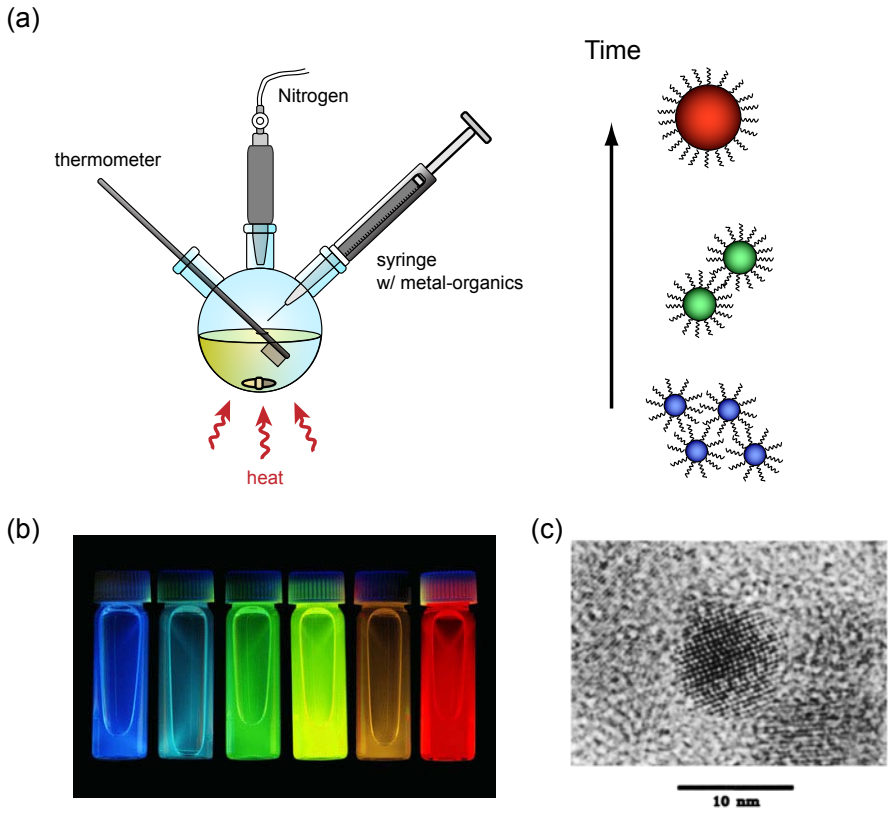

Figure 2.4: (a) Schematic of QD synthesis. (b) Photograph of CdSe QDs for a range of core diameters (photograph by Felice Frankel). (c) TEM image of a CdSe QD [33].

2.2.1 Quantum Dot Synthesis

Colloidal QDs are usually synthesized according to the procedure initially reported by Murray *et al* [33], which is shown schematically in Figure 2.4(a). This procedure involves first heating a coordinating solvent and organic ligands to a temperature of 300 °C. Organometallic precursors for the desired semiconductor (such as dimethyl cadmium and trioctylphosphine selenium for CdSe) are then rapidly injected into the reaction vessel, initiating the homogenous nucleation of nanocrystals. QD size can be monitored by measuring the absorption spectra of aliquots taken from the

growth solution. The ultimate QD size can be controlled by means of varying the temperature of the synthesis and by terminating the reaction when the desired QD size is reached. The latter is accomplished simply by cooling the growth solution to room temperature.

Following synthesis, QDs are precipitated from the growth solution and recast into a suitable solvent. Prior to their use in devices, they are usually precipitated and redissolved several times in order to eliminate excess ligands from the solution.

In this thesis, QDs of PbS (Chapters 4 and 5) and CdSe (Chapter 6) were utilized. The particular synthesis procedure for PbS QDs is reported in Ref. [83], while the synthesis of CdSe QDs is reported in Ref. [84].

2.2.2 Optical Properties

The energy of optical transitions in quantum dots are modified by the quantum confinement effect, enabling size-tunability of their absorption spectra. The confinement energy that arises may be calculated by regarding electrons and holes on the nanocrystal in terms of a standard three-dimensional particle-in-a-box problem. Assuming a spherical nanocrystal surrounded by an infinite energy barrier, the quantum confinement energy can be calculated as [41]:

$$E_{l,n}^{e,h} = \frac{\hbar^2 \phi_{l,n}^2}{2m_{e,h}a^2} \tag{2.2}$$

$m_{e,h}$ is the electron or hole effective mass, a is the nanocrystal radius and $\phi_{l,n}$ is the nth root of the spherical Bessel function of order l, $j_l(\phi_{l,n}) = 0$. For a given type of semiconductor, the confinement energy increases as the nanocrystal diameter is reduced. Also, the confinement energy will be greater for the carrier-type that

has a smaller effective mass. The extent of quantum confinement can be classified according to the size of the nanocrystal, a, relative the Bohr radius of a bulk exciton in the semiconductor, given by $a_B = \hbar^2\kappa/\mu e^2$. κ is the dielectric constant of the semiconductor and μ is the reduced effective mass ($1/\mu = 1/m_e^* + 1/m_h^*$). Many of the QD materials used in this work exist in a regime of strong confinement ($a \ll a_B$). In PbS, for example, the exciton Bohr radius is ≈ 18 nm [85], while the QD radii are in the range of 2-5 nm. In the strong confinement regime, optical transitions may be calculated as [41]:

$$\hbar\omega_v = E_g + E_v^h(a) + E_v^e(a) - 1.8\frac{e^2}{\kappa a} \tag{2.3}$$

E_g is the bulk band-gap of the semiconductor, E_v^h and E_v^e are the quantum confinement energies of electrons and holes, respectively, and the term on the right is a perturbation theory correction that takes the Coulomb interaction of quantum-confined electrons and holes into account.

The quantum confinement effect thus increases the optical transition energy over that of the bulk material. This, in turn, enables the absorption band-edge to be precisely tuned to shorter wavelengths by reducing QD size. In the case of PbS ($E_g \approx 0.4$ eV) and PbSe QDs ($E_g \approx 0.3$ eV), spectral absorption can be tuned across shortwave infrared wavelengths. The absorption spectra for PbSe QDs with a range of core diameters is shown in Figure 2.5. The ease of spectral tunability combined with access to near-infrared and shortwave-infrared wavelengths make QDs an attractive material for optoelectronic device applications. In particular, QDs make an excellent complement to organic optoelectronic devices, as few organic semiconductors absorb in the infrared.

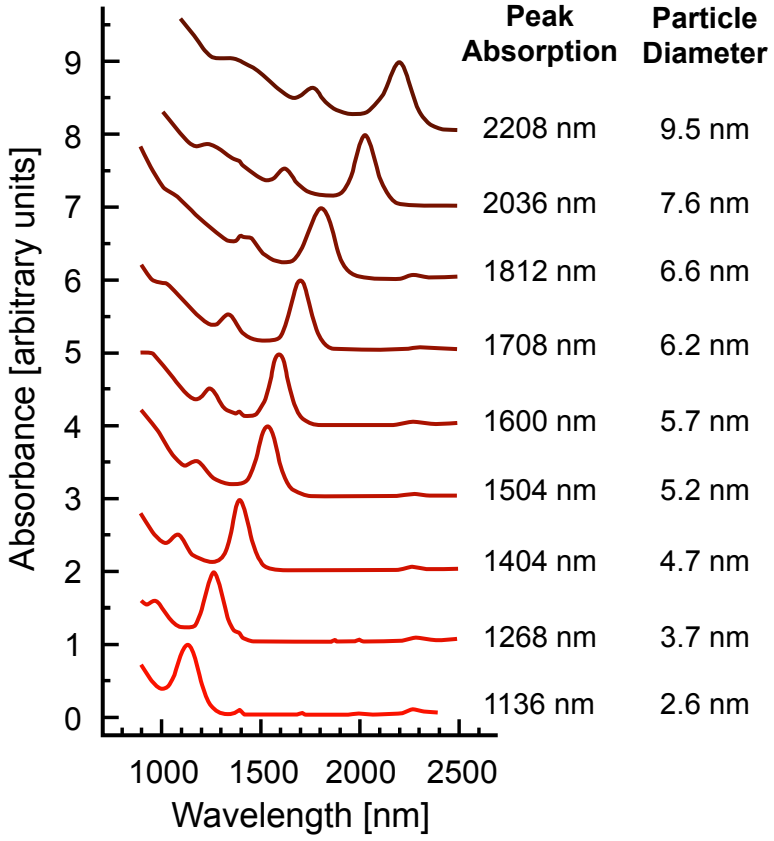

Figure 2.5: Absorption spectra of PbSe QDs as a function of nanocrystal diameter (adapted from Ref. [34]).

2.3 Field-Effect Transistors

The field-effect transistor (FET) is the fundamental building block of modern electronics and information technology. It is a three-terminal device that essentially functions as an electronic switch. A voltage applied to the "gate" electrode induces a conductive channel that allows current to flow across the other two electrodes (the "drain" and "source"). Most FETs in modern usage are implemented in crystalline inorganic semiconductors such as silicon or gallium arsenide [86]. In the past several decades, however, tremendous research has focused on the development of FETs that

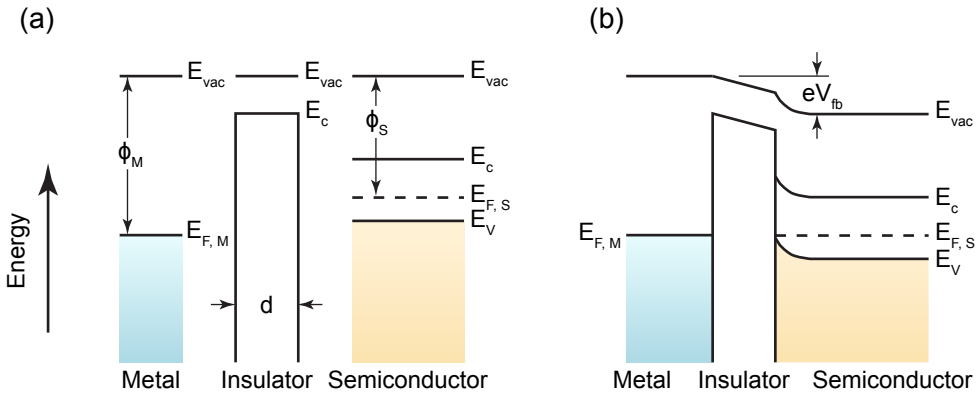

Figure 2.6: Energy band diagram of metal-insulator-semiconductor structure (a) prior to Fermi level equilibration and (b) after Fermi level equilibration (adapted from Ref. [35]).

are based on organic semiconductors [87] and other nanostructured materials [88, 89]. These efforts aim to realize devices for low-cost and flexible electronics. Scientifically, FETs also serve as a useful tool with which to characterize the electronic properties of materials. Current-voltage characteristics, for example, can provide a measure of carrier mobility as well as information about charge traps present in a material. In this section, we review the basic principles of FET operation and discuss experimental considerations associated with their fabrication and testing.

2.3.1 Principles of Operation

We begin our discussion of FET operation by first considering the metal-insulator-semiconductor (MIS) capacitor [86, 35]. The MIS capacitor consists of a semiconducting material and a metal that are separated by an insulating dielectric. When the capacitor is formed, the Fermi levels in the metal and semiconductor equilibrate, resulting in bending of the energy bands as shown in Figure 2.6. The flat band voltage,

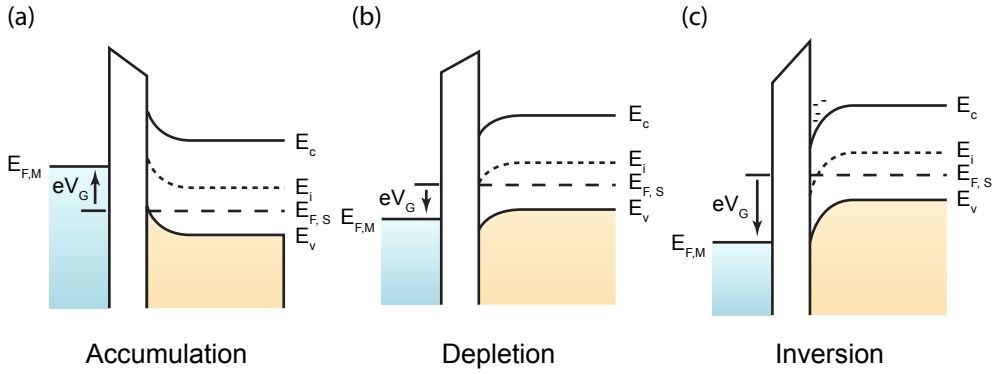

Figure 2.7: Different operating modes of a field-effect transistor: (a) Accumulation mode. (b) Depletion mode. (c) Inversion mode.

V_{fb}, is defined as the voltage required to return the energy bands to the flat band condition. V_{fb} may be calculated as the difference between the metal and semiconductor work functions:

$$eV_{fb} = e\phi_m - e\phi_s \tag{2.4}$$

Regarding the flat band condition to be the neutral state, there are 3 important regimes to the operation of a MIS capacitor. These regimes are shown schematically in Figure 2.7 for the case of a p-type semiconductor:

Accumulation: When a negative bias is applied to the gate electrode, the semiconductor energy bands bend upward, resulting in the accumulation of holes near the semiconductor/dielectric interface. The difference in the Fermi levels of the metal and semiconductor is equal to the applied bias, eV_G.

Depletion: If a positive bias is applied to the gate, the semiconductor bands bend downward, resulting in the depletion of holes from the semiconductor near the interface.

Inversion: If a sufficiently high positive bias is applied to the gate electrode, the

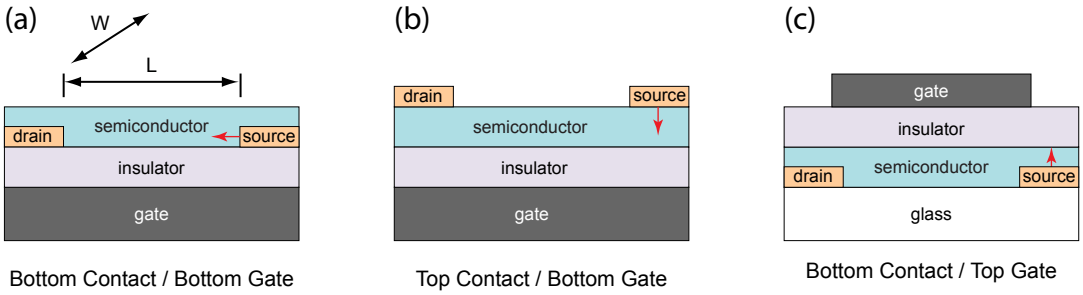

Figure 2.8: Different field effect transistor geometries: (a) Bottom Contact / Bottom Gate, (b) Top Contact / Bottom Gate, (c) Bottom Contact / Top Gate. Red arrows indicate the contact surface of charge injection (adapted from Ref. [36]).

band bending near the interface will be so severe that the Fermi level will begin to approach the conduction band of the semiconductor. At this point, electrons will begin to accumulate, effectively forming an n-type channel.

An FET essentially consists of an MIS capacitor, but with two additional electrodes (source and drain) in contact with the semiconductor. Several common FET geometries are shown in Figure 2.8. The dimensions of the FET can be characterized by its channel length (L), corresponding to the separation between the drain and source electrodes, and the channel width (W), corresponding to the distance over with the electrodes extend "into the page". The accumulation of charge near the gate dielectric when the FET is operated, for instance in inversion mode, results in a conductive channel. The application of a bias across the source and drain electrodes (V_D) will then result in a drain-to-source current (I_{DS}). The threshold voltage of the FET, V_T, can be understood as the gate bias required in order to establish this conducting channel.

2.3.2 Current-Voltage Characteristics

The FET current-voltage characteristics can be described analytically by invoking the "gradual channel approximation," in which we assume that the transverse electric field in the channel (perpendicular to the direction of current flow) is much larger than the longitudinal field. This assumption enables the FET to be analyzed as a simple one-dimensional problem [86, 35].

The amount of induced mobile charge in the channel of the FET (per-unit-area), as a function of position along the channel (x), may be calculated:

$$Q_s = C_i(V_G - V_T - V_c(x)) \tag{2.5}$$

C_i is the capacitance of the gate dielectric and $V_c(x)$ is the channel voltage as a function of x; $V_c(0) = 0$ at the source and $V_c(L) = V_D$ at the drain. The drain-source current (I_D) through a cross-section of the channel may then be written:

$$I_D = W\mu Q_s \frac{\mathrm{d}V_c(x)}{\mathrm{d}x} \tag{2.6}$$

Note that we assume the carrier mobility to be independent of the electric field. Rearranging this equation,

$$I_D \mathrm{d}x = W\mu Q_s \mathrm{d}V_c(x) \tag{2.7}$$

We now plug in the expression for Q_s (Equation (2.5)) and integrate from $x = 0$ to $x = L$:

$$I_D = \frac{\mu W C_i}{L}\left[V_G - V_T - \frac{V_D}{2}\right] V_D \tag{2.8}$$

This equation describes the current-voltage characteristics of the FET. For low applied drain biases ($V_D < V_G - V_T$), the quadratic term in the brackets may be neglected,

resulting in a linear relationship between I_D and V_G. This operating regime of the FET is referred to as the *linear* or ohmic regime:

$$I_D = \frac{\mu W C_i}{L}(V_G - V_T)V_D \tag{2.9}$$

As V_D is increased, I_D will begin to deviate from this linear relationship. This is due to the reduction of induced charge near the drain electrode by the channel voltage. The point at which the induced charge at $(x = L)$ becomes zero is referred to as "pinch-off," occurring when $V_D = V_G - V_T$. At this point, I_D becomes saturated with further increase of V_D and the FET is said to operate in the *saturation* regime. The saturation current is obtained by plugging the saturation condition $(V_D = V_G - V_T)$ into Equation (2.8):

$$I_D = \frac{\mu W C_i}{2L}(V_G - V_T)^2 \tag{2.10}$$

Characterization of an FET in the linear or saturation operating regime enables straightforward extraction of the carrier mobility by Equations (2.9) and (2.10), respectively.

2.3.3 Device Structures

The particular device structure used to implement an FET with a given semiconductor, including the geometry of the device and the choice of dielectric and electrode materials, is critical in determining its ultimate performance characteristics. A very common device structure for FETs that incorporate nanostructured materials is the bottom contact / bottom gate (BC/BG) geometry shown in Figure 2.8(a). This structure is advantageous because because it can readily be fabricated from a wafer

of degenerately doped silicon, where the silicon serves as the gate, a thermally-grown layer of SiO_2 serves as the gate dielectric ($\epsilon = 3.9$), and patterned metal electrodes serve as the source and drain. Substrates can be purchased with high-quality SiO_2 dielectrics already grown on them, obviating the need to further processing in order to deposit a gate dielectric. Often, the SiO_2 is modified with a surface treatment such as hexamethyldisiloxane (HMDS) or octadecylsilane (OTS) to improve the morphology of the semiconductor film or passivate electron-trapping hydroxyl groups on the SiO_2 surface [90, 91, 92] . High-quality surface passivation has been shown to be critical to enabling n-channel FET operation in organic FETs [87]. We note that the BC/BG geometry can also readily be implemented with non-silicon back-gates, as is necessary for the realization of integrated circuits [93, 94].

Alternative device structures include the top contact / bottom gate (TC/BG) and bottom contact / top gate (BC/TG) configurations shown in Figures 2.8(b-c). These geometries are sometimes referred to as "staggered," due to the fact that the channel is formed opposite from the source/drain electrodes. One of the main advantages of a staggered geometry is that the contact resistances at the drain and source electrodes are often far lower than in a comparable "co-planar" structure [95, 96, 97], such as the BC/BG configuration. This is due to the fact that in co-planar FETs, charge is injected into the channel only from the side walls of the source and drain electrodes. In contrast, current injection in a staggered geometry occurs from the much larger top surfaces of the source/drain electrodes (as indicated in Figure 2.8). Consequently, devices based on staggered architectures often can be operated under lower biasing conditions than their co-planar counterparts. In Chapter 5, we discuss several FET

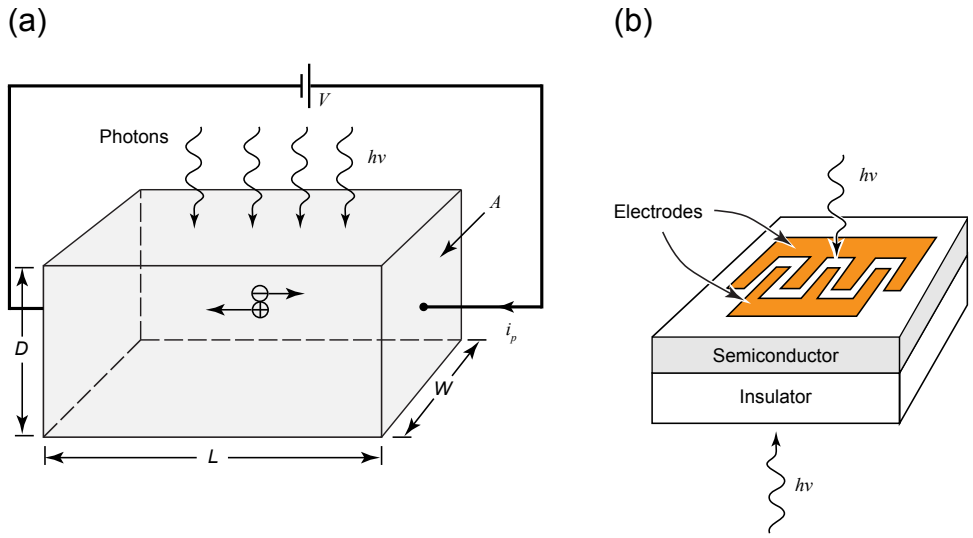

Figure 2.9: (a) Schematic of photoconductor operation. (b) Photoconductor structure with interdigitated electrodes (Adapted from Ref. [37]).

structures, including BC/BG and BC/TG devices, that incorporate thin films of PbS QDs.

2.4 Photoconductors

A photoconductor is essentially a light-sensitive resistor. It consists of a film of semiconducting material that is contacted with two electrodes. Under illumination, the absorption of light generates free carriers that increase the conductivity of the material, resulting in a photocurrent. The generation of carriers may be due to band-to-band (intrinsic) transitions or, alternatively, transitions involving impurity levels in the band gap (extrinsic photoconductivity). In this thesis, we are exclusively concerned with intrinsic quantum-dot-based photoconductors in which the transitions are determined by the band gap of the QDs. Specific devices are discussed in Chapters 4

and 6.

One of the main advantages of a photoconductor is the presence of an internal photoconductive gain mechanism. Gain allows for the possibility of extracting several carriers from the device for a single absorbed photon. To understand this mechanism, we consider a basic photoconductor structure shown in Figure 2.9(a). We make the following assumptions about its operation: (1) The device is sufficiently thick to absorb 100% of the light (device thickness, $D \gg 1/\alpha$) and (2) the contacts are ohmic for both carrier types. The photocurrent can be described by [60, 86]:

$$I_{photo} = q\eta \left(\frac{P_{opt}}{h\nu}\right) G \tag{2.11}$$

Here, P_{opt} is the illumination power incident to the device, η is the quantum efficiency (i.e. the number of carriers generated per photon) and G is the photoconductive gain. G may be greater than or less than unity depending on the configuration of the photoconductor as well as the bias condition. To determine an expression for G, we note that the photocurrent may also be written in terms of Ohm's Law:

$$I_{photo} = \sigma EWD = (\mu_n + \mu_p)\Delta nqEWD \tag{2.12}$$

E is the applied electric field across the two electrodes ($E = V_{bias}/L$) and Δn is the excess carrier concentration that results from illumination. The magnitude of Δn will depend on the generation and recombination rates that are operative in the photoconductor. The relevant rate equation may be written:

$$\frac{\mathrm{d}\Delta n}{\mathrm{d}t} = \left(\frac{P_{opt}}{h\nu}\right)\frac{\eta}{WLD} - \frac{\Delta n}{\tau} \tag{2.13}$$

τ is the excess carrier lifetime. Under steady-state illumination conditions we have:

$$\frac{\Delta n}{\tau} = \frac{\eta(P_{opt}/h\nu)}{WLD} \tag{2.14}$$

By combining Equations (2.12) and (2.14), we obtain:

$$I_{photo} = q\eta \left(\frac{P_{opt}}{h\nu} \right) \frac{(\mu_n + \mu_p)\tau E}{L} \tag{2.15}$$

Finally, referring to Equation (2.11), we determine the photoconductive gain to be:

$$G = \frac{(\mu_n + \mu_p)\tau E}{L} = \tau \left(\frac{1}{t_{rn}} + \frac{1}{t_{rp}} \right) \tag{2.16}$$

t_{rn} and t_{tp} are the transit times of electrons and holes, respectively ($t_r = L/\mu E$). If the transit time of the minority carrier is much larger than that of the majority carrier (for instance if it becomes trapped), then G will simply scale with the ratio of the recombination lifetime and the transit time of the majority carrier. In terms of device operation, G will directly scale with applied bias ($G \propto V_{bias}$) and with the inverse square of the channel length ($G \propto L^{-2}$). To maximize gain, therefore, the applied voltage should be as high as possible and the channel length should be as short as possible.

2.5 Heterojunction Photodiodes

Solar cells and photodetectors that incorporate nanostructured materials must be engineered to allow for the dissociation of photo-generated Frenkel excitons into free carriers that can be collected at the electrodes as photocurrent. This is usually accomplished by utilizing a donor/acceptor hetero-interface to facilitate exciton dissociation [98, 99]. An energy band diagram for a heterojunction photodiode is shown in Figure 2.10. The total external quantum efficiency (η_{EQE}) of the device can be expressed as the product the four processes shown in Figure 2.10: (1) Absorption

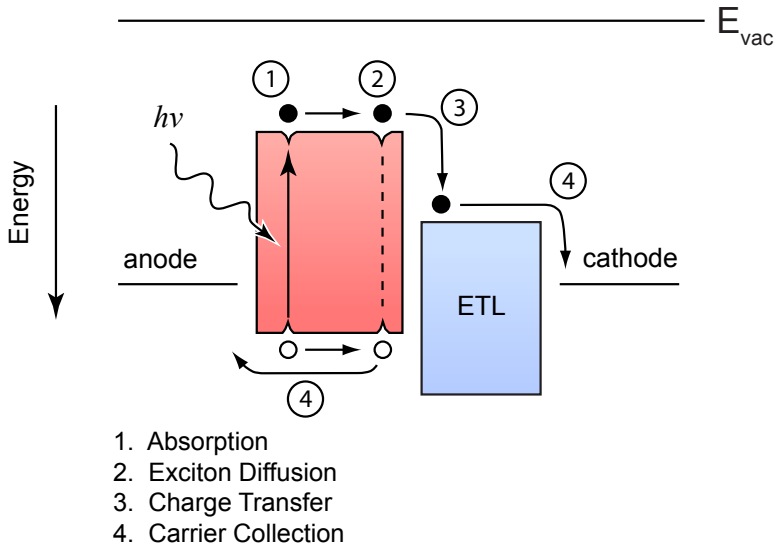

Figure 2.10: Critical processes for the generation of photocurrent in a donor-acceptor heterojunction diode.

(η_α), (2) exciton diffusion (η_{ED}), (3) exciton dissociation, or charge transfer (η_{CT}), and (4) carrier collection (η_{CC}).

$$\eta_{EQE} = \eta_\alpha \eta_{ED} \eta_{CT} \eta_{CC} \tag{2.17}$$

Device performance is often limited by poor exciton diffusion efficiency (η_{ED}), which results from the fact that excitons in nanostructured materials often migrate only short distances by random diffusion before recombining. The exciton diffusion length, L_D, is usually in the range of 3-10 nm in organic semiconductors [100, 98]. This is far less than the thickness of an active layer material required in order to capture an appreciable amount of light ($1/\alpha \approx 100$ nm [101]). Consequently, the exciton diffusion process imposes a considerable limit to how much light can be harvested in this type of structure. The thickness and morphology of the active layers must therefore be carefully designed in order to maximum the exciton diffusion efficiency

and device performance. These considerations will be discussed in the context of a J-aggregate photodiode structure in Chapter 7)

Chapter 3

Experimental Methods

This chapter reviews the experimental methods employed to fabricate and characterize the devices that are described in this thesis. We present an overview of the ONElab growth system, a review of the various specific deposition techniques that were utilized, and a description of electrical and optical characterization techniques that were employed.

3.1 ONElab Growth System

The fabrication of nanostructured optoelectronic devices generally involves the sequential processing of several layers of different materials. For example, organic active layers may be deposited by thermal sublimation, while indium-tin-oxide (ITO), a material commonly used as a transparent electrode, is typically deposited by means of RF magnetron sputtering. A critical concern throughout the processing of active device layers is that the electrical characteristics of many nanostructured and thin-film

materials are sensitive to oxygen and water, and must therefore be maintained in dry and inert environments in order to minimize degradation. Even a brief exposure of an incomplete device to air, which may occur while transferring it from one tool to the next, may result in drastic and adverse changes to the already-deposited materials' properties. In ONElab, the inert processing of device layers is facilitated through the use of the ONElab growth system, shown schematically in Figure 3.1. Samples may be prepared in a glovebox environment prior to being loaded into the "transfer line" vacuum system via a load lock. A cart and pulley system facilitates the transfer of samples among several different deposition tools including thermal evaporators, a chemical vapor-phase deposition reactor and a sputter-deposition tool. Manually-operated rack-and-pinion feedthroughs on each of these systems are used to seize samples from the transfer line and return them following the completion of the process. In this manner, multi-layer device structures may be built up without the substrate ever leaving an inert environment. Following the completion of processing, electrical and optical testing may be conducted in a second nitrogen glovebox system, located at the opposite end of the transfer line.

3.2 Thin Film Deposition Techniques

This work spans the use of a diverse array of materials including polymeric and small-molecule organic semiconductors, colloidal quantum dots, metal-oxide semiconductors and metals. Consequently, a variety of material deposition techniques were employed. These techniques can be divided into two categories: (1) solution-processing and (2) physical vapor deposition.

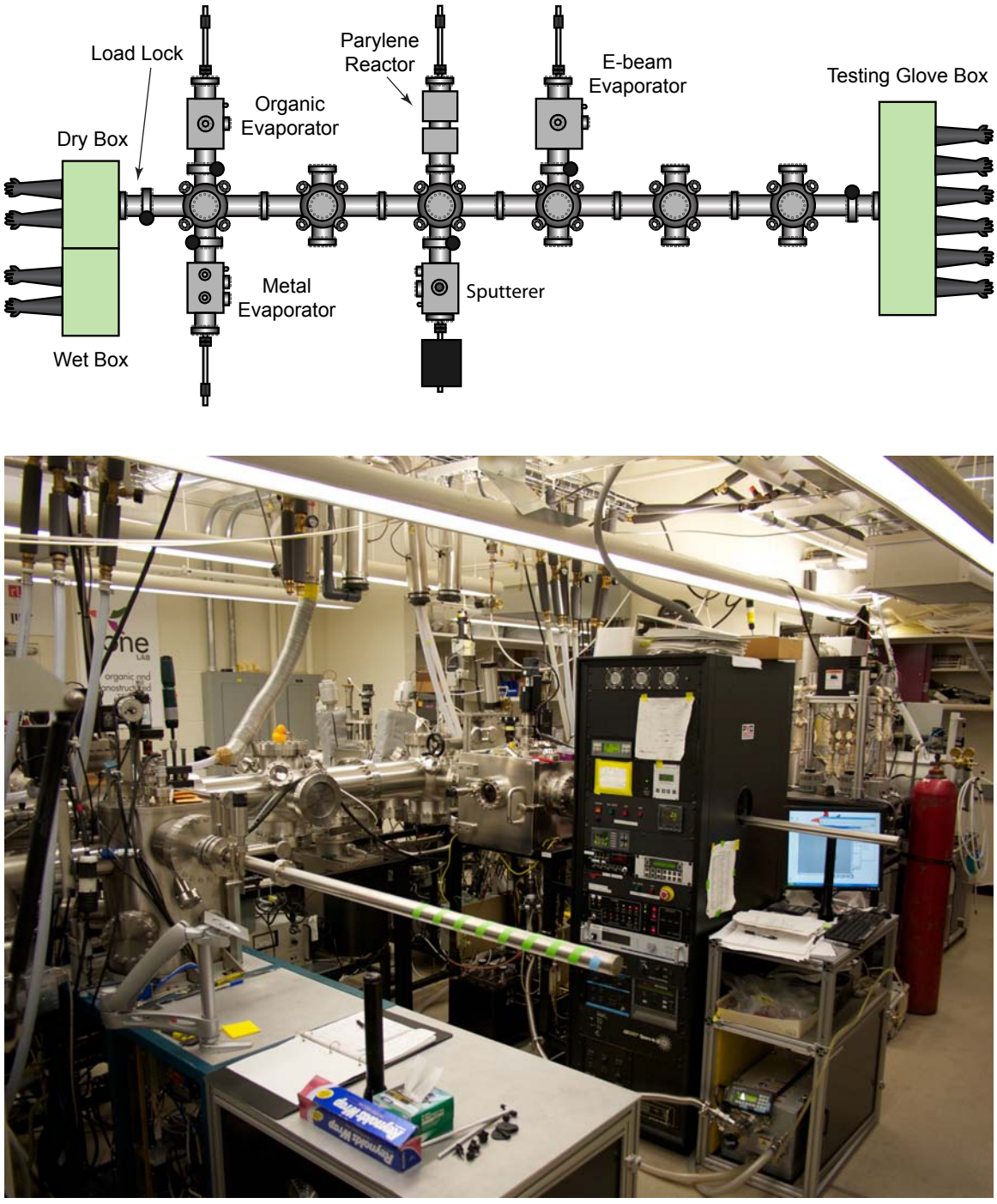

Figure 3.1: Schematic and photograph of the ONElab growth system in December, 2011.

Table 3.1: Spin-coating conditions for several of the materials used in this thesis.

Solution [material / solvent]	**Spin Conditions** [concentration / spin speed]	**Thickness**[a] [nm]
U3[b] / water	10 mg mL^{-1} / 4000 RPM	15[c]
PbS QDs (oleic acid) / octane	15 mg mL^{-1} / 1500 RPM	15
PCBM[d] / chloroform	10 mg mL^{-1} / 1500 RPM	55
Microchem A4 PMMA / anisole	unknown / 1000 RPM	465
Polystyrene[e] / butyl acetate	50 mg mL^{-1} / 2000 RPM	330

[a] Measured with stylus profilometry unless otherwise specified.
[b] Purchased from Ryan Scientific.
[c] Measured with optical ellipsometry.
[d] Purchased from Polymer Source Inc. with M_w = 221,500 and M_w/M_n = 1.04.
[e] Purchased from American Dye Source.

3.2.1 Solution Processing

In this thesis, spin-casting was used extensively for the deposition of polymers, colloidal quantum dots and some low-molecular-weight organic materials. This technique involves dispensing a solution of the desired material onto a substrate that is rotating at a high speed. The rotation distributes the solution across the substrate resulting in a high-quality film of nearly-uniform thickness. The solvent typically evaporates from the film in seconds to minutes [102, 103], depending on its particular boiling point. A solvent with a low boiling point such as chloroform ($T_{boiling}$ = 61.2 °C), for example, evaporates much faster than a solvent with a higher boiling point, such as octane ($T_{boiling}$ = 125.5 °C). The film thickness may be controlled by the choice of solvent, the particular concentration of the solution and the rotation speed (typically in the range of 1000-6000 rotations-per-minute.) The spin conditions for several of the materials used in this thesis are presented in Table 3.2.1.

3.2.2 Physical Vapor Deposition

A number of materials are not readily processible from solution, including the metals (Al, Ag, Au) and metal-oxide materials (MoO_3, ZnO, ITO, Al_2O_3) that were used in this work. For these materials, a suitable physical vapor deposition (PVD) process was used for film deposition. PVD involves physically reducing the desired material into a vapor (for example by thermal evaporation or ion bombardment) and allowing it to condense onto a substrate. For some organic materials, such as spiro-TPD, PVD may be preferable to solution processing as it affords superior thickness control and film quality.

Thermal Evaporation

A schematic and photograph of the thermal evaporator system used extensively in this thesis are shown in Figure 3.2. Source materials are contained in tungsten crucibles (obtained from R.D. Mathis Company) that reside in a high vacuum system. The base pressure is maintained at $<10^{-5}$ Torr. AC current delivered from an external power supply heats up the source crucible, resulting in the sublimation of the material it contains. The substrates to be coated are mounted above the crucible on a rotating stage. The vaporized source material condenses on the substrates at a rate that is controlled by the amount of electrical current delivered to the crucible. The rate of deposition is monitored with a quartz crystal thickness monitor that resides inside the vacuum chamber. Most of the materials used in this work were deposited at a rate of ≈ 1Å/s.

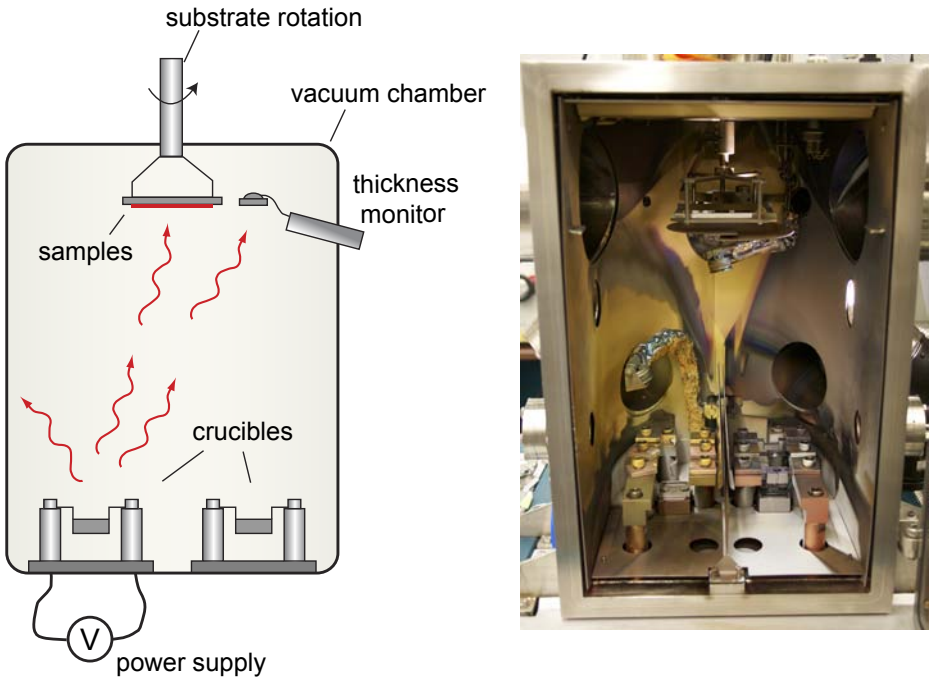

Figure 3.2: Schematic and photograph of the ONElab thermal evaporator system.

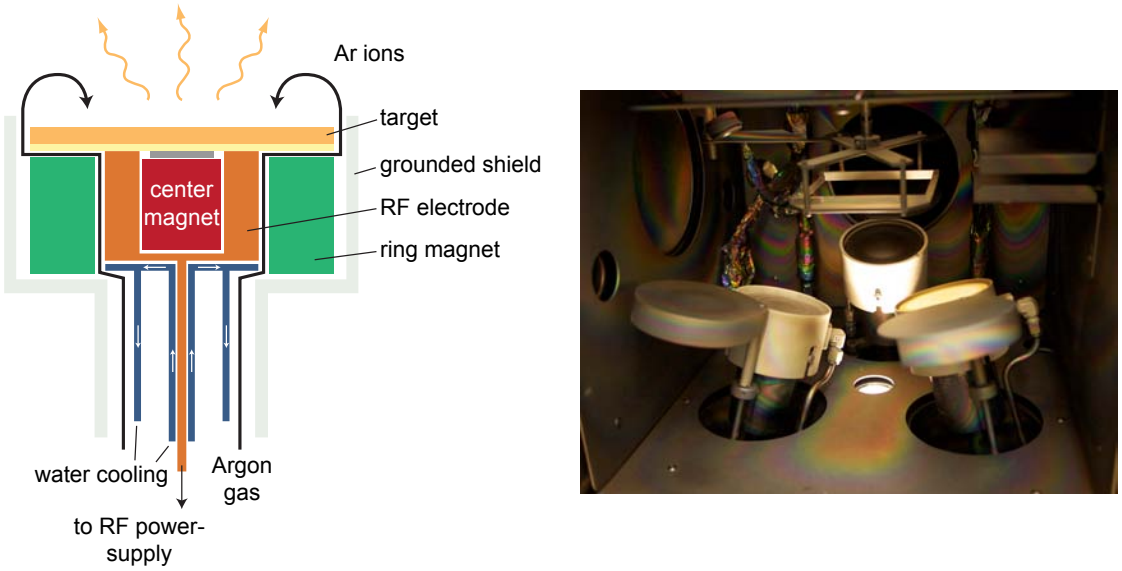

Figure 3.3: Schematic of RF magnetron sputterering (adapted from [38]) and photograph of the ONElab sputtering system.

RF Magnetron Sputtering

For materials with high melting points, including the metal-oxides ITO and ZnO used in this work (T_M >2000 K), thermal evaporation cannot be straightforwardly used for film deposition. In these cases, RF magnetron sputtering may be used. Rather than simply relying on heat to vaporize the source material, this technique involves bombarding a "target" of the desired source material with energetic ions to physically eject material from the surface. This ejected material will then be able to condense onto the substrate to form a film.

The ONElab sputtering system consists of three MAK-300-V magnetron sputtering gun (US Inc.). A schematic of a sputtering gun as well as a photograph of the ONElab sputtering system are shown in Figure 3.3. The sputtering chamber is pumped down to $<10^{-5}$ Torr and back-filled with Argon to a set pressure that is

maintained by a feedback-controlled variable gate valve. The application of a suitably high voltage (200-1000 V) to the cathode by an RF power supply ionizes the incoming Argon gas. Magnets within the gun create a magnetic trap that confines this Argon plasma to just above the sputtering target, physically isolating it from the substrates that are mounted on a rotating stage above. The Ar^+ ions in this plasma are accelerated into the target by the applied potential with sufficient energy to eject material from the surface. Since the ejected particles of the target are electrically neutral, they are able to freely traverse across the chamber and condense onto the substrate.

For insulating materials, the surface of the target is prone to become positively charged during the sputtering process. This build-up of charge will gradually screen the cathode potential. To avoid this undesirable situation, the voltages applied to the cathode and anode are reversed at a sufficiently high frequency ($f = 13.65$ MHz in our system) to periodically neutralize the built-up charge before it can accumulate to an appreciable extent.

Control of the working gas pressure and the RF power applied to the cathode enables precise control of the the rate of deposition. The sputter-deposition of several materials will be discussed in the context of a hybrid metal-oxide/organic photodetector structure in Chapter 7.

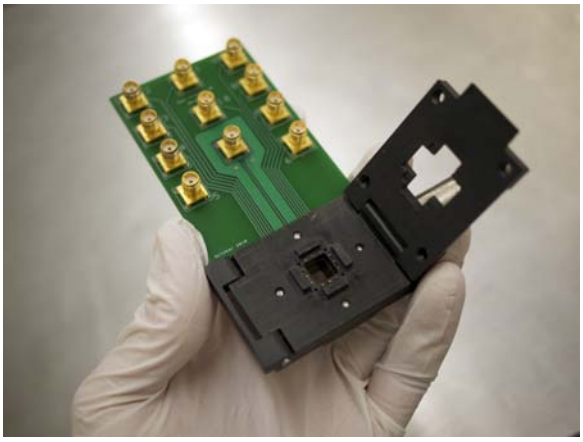

Figure 3.4: Photograph of custom-built test fixture used in this work.

3.3 Device Characterization Techniques

3.3.1 Basic Electrical Characterization

All of the electrical measurements presented in this thesis were conducted in a nitrogen-filled glovebox environment. Connection to device electrodes is established with a custom-built test fixture (see Figure 3.4), initially described in Ref. [101]. A latch secures a $0.5'' \times 0.5''$ sample and 10 spring-loaded gold pins make contact to the device around the samples' edges. A custom printed circuit board was fabricated to facilitate easy electrical connection via SMA connectors.

A variety of test equipment was used to study the electrical characteristics of devices. A Keithley 6487 Sourcemeter was used to measure current-voltage (I-V) characteristics of photodiodes and photoconductors. These measurements were conducted in the dark as well as under illumination from various light sources including LEDs and diode lasers.

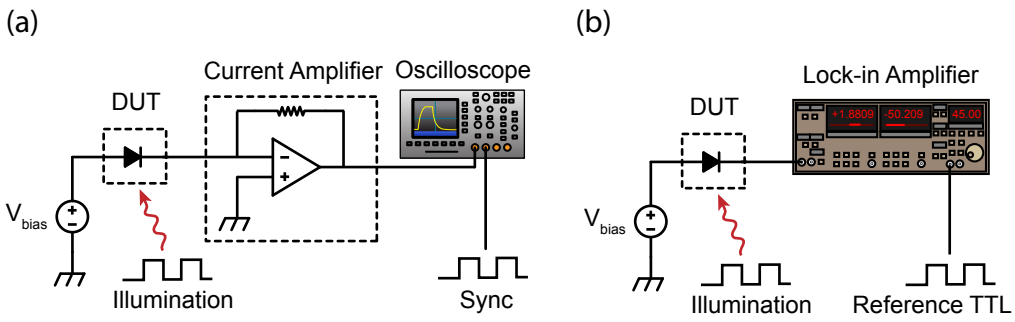

Figure 3.5: (a) Measurement of transient photoresponse with a current amplifier and oscilloscope. (b) Measurement of transient photoresponse with a lock-in amplifier.

For characterization of field-effect transistors (FETs), an Agilent 4156C Semiconductor Parameter Analyzer was used. Transfer characteristics (drain-source current plotted as a function of gate bias for fixed drain biases) and output characteristics (drain-source current plotted as a function of drain bias for fixed gate biases) were measured. Capacitance-voltage (C-V) characteristics were measured with an Agilent 4156C or a Solartron 1260 Impedance Analyzer. All measurements on FETs and capacitive structures were conducted with a text-fixture that was mounted inside a custom-built dark box to ensure that ambient illumination was minimized.

3.3.2 Measurement of Response Speed

The speed with which a photodetector can respond to changes in incident illumination is an important figure-of-merit that qualifies its potential uses. This metric can be quantified in a number of ways. In this thesis, we measure the response speed in terms of the fall time (τ_{fall}) and the 3-dB bandwidth (f_{3dB}). τ_{fall} is the time constant of the the decay in photoresponse following a pulse of illumination. The 3-dB bandwidth is the frequency at which the photodetector's response to modulated

illumination is attenuated by 3 decibels, corresponding to a decrease in magnitude by a factor of $1/\sqrt{2}$, or attenuation to $\approx 71\%$ of its initial magnitude. We note that an additional commonly used metric is the "10%-90% rise/fall time", which is the time required for the photoresponse to vary between 10% of its initial value and 90% of its initial value in response to a sharp pulse of illumination.

The experimental setup used to measure τ_{fall} is shown in Figure 3.4(a). The device-under-test (DUT), represented in this case by a photodiode, is illuminated with a pulse of light from a diode laser. The resulting photocurrent is amplified with a Femto DHPCA-100 current amplifier and its decay monitored on a Tektronix 3054C oscilloscope. For conducting this measurement, several factors must be considered in order to ensure that the measured decay time is in fact limited by the DUT: (1) the rise/fall time of the light source must be faster than the DUT, (2) the speed of the measurement electronics must be faster than the DUT and (3) the capacitance at the input of the current amplifier should be considered and minimized.

For the measurements presented in this thesis, a TTL-modulated Newport LQD laser diode with at rise/fall time of 2 ns was used as the excitation source. The speed of the Tektronix 3054C oscilloscope is 500 MHz, also corresponding to a rise/fall time of ≈ 2 ns. The speed of the Femto DHPCA-100 is determined by the particular gain setting (Volts-per-Amp) used; the lowest gain of 10^2 corresponds to a rise/fall time of 1.8 ns, although this specification becomes slower at higher gain settings. The response speed measurement limit is thus expected to fall in the range of 2-25 ns, provided that the gain on the amplifier is 10^4 or lower.

To experimentally confirm that the rates of photoresponse decay were not limited

by the measurement electronics, the response speed of a Thorlabs FDS100 silicon photodiode was measured in the setup shown in Figure 3.4(a). τ_{fall} was measured to be 610 ns at zero-bias and 22 ns at a reverse bias of -20V. This is close to the diode specification of 10 ns and confirms that our setup is able to measure a current decay that is at least as fast as $\approx$ 20 ns. The amplifier gain setting was varied, including gains of 10^2 ($\tau_{rise/fall}$ = 1.8 ns) and 10^3 ($\tau_{rise/fall}$ = 4.4 ns), and no effect on the time constant was observed. Additionally, the parasitic capacitance at the input of the current amplifier was varied by connecting the DUT and amplifier with varying lengths of coaxial cable ranging from 2 ft ($\approx$ 90 pF) to >20 ft ($\approx$ 670 pF). The decay time constant was unaffected by these changes, although considerable ringing in the response was observed as the parasitic capacitance was increased. These tests confirm that the measured response speed is indeed limited by the DUT.

The 3-dB frequency may be estimated from the measurement of τ_{fall}. A more direct way of determining f_{3dB}, however, is to measure the photoresponse of the device to a modulated light source (such as a laser diode or an optically chopped light source) as a function of the modulation frequency. The point at which the peak-to-peak amplitude of the photoresponse is attenuated by 3-dB can readily be measured on an oscilloscope, as shown in Figure 3.4(a). Alternatively, this measurement may be made with a lock-in amplifier, as shown in Figure 3.4(b). In this thesis, a Stanford Research Systems Model 830 lock-in amplifier was used, limiting the measurable bandwidth to 70 kHz (utilizing the lock-in amplifier's current input with a gain of 10^6).

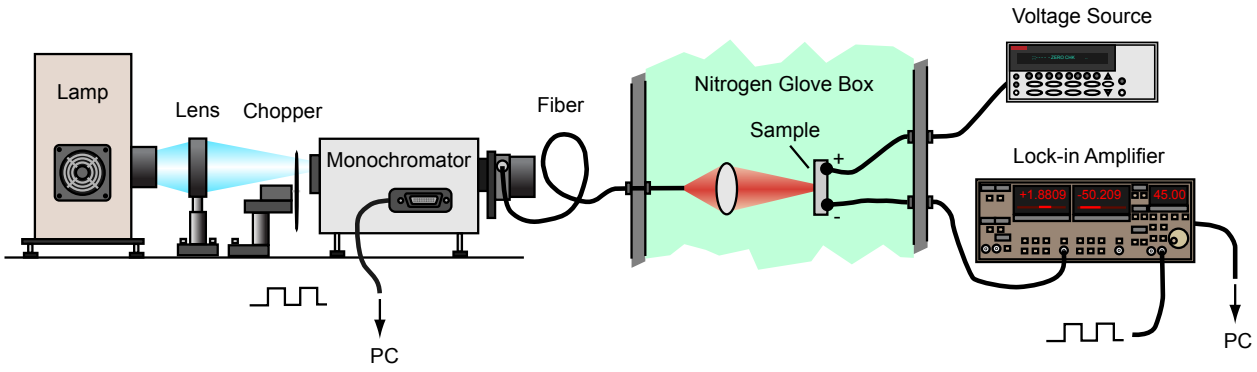

Figure 3.6: Schematic of set-up used to measure photocurrent action spectra inside a glovebox environment.

3.3.3 Measurement of Photocurrent Spectra

An important technique for characterizing the performance of photosensitive devices is to measure their photoresponse as a function of wavelength. Of particular interest is the determination of the photon-to-electron conversion efficiency, also referred to as the external quantum efficiency (EQE). The experimental setup used to conduct this measurement is shown schematically in Figure 3.6. Monochromatic light is first generated by focusing broadband light from a 1000W xenon arc lamp (Newport Model 66921) or 1000 W quartz tungsten halogen (QTH) lamp (Newport Model 66885) through an optical chopper into an Acton Spectrapro 300i monochromator. The output from the monochromator is coupled into the glovebox with an optical fiber and used to illuminate the device under test. A lock-in amplifier (Stanford Research Systems Model 830), provided with the reference signal from the optical chopper, is used to extract the AC photocurrent. Following calibration of the spectrally-resolved incident optical power ($P_o(\lambda)$) with a calibrated photodiode (Newport 818-UV or Newport 818-IR), the spectral response of the device is measured. The EQE is then

calculated for a particular wavelength using the equation:

$$EQE = \frac{I_{ph}}{q}\left(\frac{h\nu}{P_o}\right) \times 100\% \tag{3.1}$$

I_{ph} is the measured photocurrent, h is Planck's constant and ν is the frequency of illumination. The related metric of responsivity, in Amps-per-Watt, may readily be calculated from the external quantum efficiency using the equation:

$$R = \frac{I_{ph}}{P_o} = \frac{\eta q}{h\nu} \tag{3.2}$$

Here, η is the unitless quantum efficiency ($EQE/100\%$).

3.3.4 Noise Equivalent Power and Specific Detectivity

A critical consideration to photodetection is the presence of random fluctuations, or "noise", in the current passing through the device. The presence of noise obscures the detection of the desired signal and should carefully be considered and minimized, if possible. Several figures-of-merit have been established to quantify the effective sensitivity of a photodetector, taking noise into account. Among these are the noise equivalent power and specific detectivity.

The noise equivalent power (NEP) is defined as the incident power (in Watts) required to realize a unity signal-to-noise ratio over a bandwidth of 1 Hz. NEP may also be interpreted as the minimum detectable signal power for the detector. NEP may be calculated by I_n/R, where I_n is the root-mean-squared (RMS) noise current (over a particular bandwidth, Δf) and R is the responsivity.

The detectivity (D) is defined as the inverse of the NEP. A normalization of this metric to the detector area and bandwidth gives the widely used metric of specific

detectivity, or D^* [60]:

$$D^* = \frac{\sqrt{A_D \Delta f}}{NEP} = (A_D \Delta f)^{1/2} \frac{R}{I_n} \tag{3.3}$$

Here, A_D is the active area of the device and Δf is the bandwidth over which the noise current is measured.

To measure D^*, the responsivity at a particular wavelength and for a particular biasing condition may be measured using the technique described in Section 3.3.3. The RMS noise current, I_n, is often calculated from the dark I-V characteristics of the device with the assumption of a dominant noise mechanism. For photodiodes operating at zero-bias, Johnson-Nyquist noise, which results from random thermally-induced current fluctuations, is assumed to be the dominant noise mechanism, giving a RMS noise current:

$$I_{J-N} = \sqrt{4k_B T \Delta f / R_D} \tag{3.4}$$

R_D is the differential resistance of the diode, measured about zero-bias. With a bias applied across the device, the shot noise from the dark current often dominates the noise. The RMS shot noise current can be calculated with the equation:

$$I_{shot} = \sqrt{2q I_{dark} \Delta f} \tag{3.5}$$

I_{dark} is the dark current of the diode under a particular biasing condition. The total RMS noise current in a photodiode may be then be calculated as [86]:

$$I_n = \sqrt{I_{J-N}^2 + I_{shot}^2} \tag{3.6}$$

In photoconductors, the dominant noise mechanism is usually "generation-recombination" noise, which is due to variations in the conductivity of the device originating from

the random generation and recombination of carriers. The generation-recombination noise may be described by the equation:

$$I_{G-R} = \sqrt{\frac{4qIG\Delta f}{1+\omega^2\tau^2}} \tag{3.7}$$

G is the photoconductive gain, I is the current flowing through the photoconductor, ω is the modulation frequency and τ is the carrier life-time.

It is important to note that these calculations for I_n represent ideal limits of the noise level, and may underestimate the total noise present in the system. In particular, these estimates neglect "1/f" or "flicker" noise, which contributes to noise at low frequencies [60]. It is thus ideal to measure the noise current in the device directly, particularly if the low-frequency range is of interest. In this thesis, the noise currents in PbS QD photoconductive structures were experimentally measured under dark conditions and at room temperature. Devices were loaded into a Janis ST-100 cryostat and the noise current was measured as a function of frequency with a Stanford Research Systems Model SR785 Dynamic Signal Analyzer. These measurements are presented and discussed in Chapter 4. A detailed discussion of noise in QD photoconductors is also available in Ref. [104].

3.3.5 Cryogenic Measurements

For characterization of field-effect transistors at reduced temperature, a Janis ST-100 cryostat was used (see Figure 3.7). The sample was mounted directly onto a copper cold finger with a teflon block and contact was made with spring-loaded gold pins. Liquid helium was used to reduce the temperature of the cold finger. A Lakeshore 330 Autotuning temperature controller, in conjunction with a 25 Ω

Figure 3.7: Photograph of Janis ST-100 cryostat used in this work.

cartridge heater and silicon temperature sensor (Lakeshore DT-470-CU-12), was used to maintain desired temperature points.

Chapter 4

Photoconductors Consisting of PbS QD Films

In this chapter, several QD-based photoconductors are presented with sensitivity extending to SWIR wavelengths. The fabrication and characterization of these devices are described, and several approaches for improving their performance are investigated.

4.1 Introduction

4.1.1 QD Photoconductors

Thin films of colloidal nanocrystal quantum dots (QDs) have attracted considerable interest for a variety of optoelectronic device applications. Much of this interest pertains to the freedom available to directly engineer their optoelectronic properties by varying the nanocrystal size [80] as well as by chemically modifying QD surfaces

with oxidation [105, 83] or ligand exchange [106, 84, 107, 108, 109, 110]. Of particular interest is the prospect for QD optical response that extends into the short-wavelength infrared (SWIR) part of the spectrum (wavelengths of $\lambda = 1.0\mu$m to 2.0μm) with QDs of low-bandgap semiconductors such as PbS and PbSe. This wavelength range is largely inaccessible to organic materials yet is critical to efficient photovoltaics [58], night vision [111, 2], biological imaging applications [112, 113], and optical communication [114, 115].

Photoconductive detectors in a planar geometry (i.e. consisting entirely of semiconducting films deposited over laterally arranged electrodes) are particularly attractive for commercial application due to the potential ease with which they can be directly integrated with conventional detector read-out integrated circuits [94, 116]. Several photodetectors of this geometry have been reported with sensitivity at infrared wavelengths (λ >700 nm) [23, 9, 117, 17, 21, 25]. In the structure described by Konstantatos *et al*, consisting of a single spin-coated film of PbS QDs deposited over interdigitated gold electrodes [23], a specific detectivity (D^*) of $\approx 10^{13}$ Jones was reported. This is comparable to that of state-of-the-art epitaxially-grown InGaAs photodetectors [60]. A critical shortcoming with this device structure, however, is that it exhibits a very slow temporal response (f_{3dB} <20 Hz) attributed to long-lived QD surface traps. This problem precludes its use in applications such as optical communication in which high speed is required [114, 115].

4.1.2 Interfacial Recombination for Improved Response Speed

Since there exists a fundamental trade-off between gain and bandwidth in PbS QD-based planar photoconductive structures, one strategy for enabling faster device response is to deliberately sacrifice photoconductive gain to an extent that is tolerable by accelerating carrier recombination. It has been demonstrated, for instance, that the appropriate selection of QD ligands can limit the presence of trap states to only those with desired lifetimes [69]. Though effective in reducing the photocurrent decay time constant to 27 ms, this approach places an upper limit on device bandwidth associated with the fastest trap state that can be isolated with chemical treatment.

We introduce an alternative approach to controlling the transient response of planar QD photodetectors through the utilization of an organic/QD heterojunction to affect the recombination rate of charge carriers in the device. Specifically, we incorporate a film of the fullerene derivative, [6,6]-phenyl C_{61}-butyric acid methyl ester (PCBM), which creates a type-II hetero-interface with PbS QDs, into a planar PbS QD photoconductor structure. Charge separation at a QD/fullerene interface was first reported by [118] and later exploited to realize a planar photodetector structure consisting of a blend of as-synthesized PbS QDs (insulated with long oleic acid ligands) with PCBM [25]. In the present study, this fast charge separation process is employed to transfer photo-generated electrons from PbS QDs into the PCBM layer, where they may recombine across the PbS QD/PCBM interface rather than be subject to slow trap-mediated bulk recombination processes in the QD film.

4.1.3 Chemical Modification of the QD Film

Through the utilization of a bi-layer heterojunction structure [119, 120] rather than an organic/QD blend, we also enable the application of aggressive chemical treatments to the QD film in order to further control device response without affecting the organic semiconducting layer. Here, we utilize both a chemical treatment in 1,2-ethanedithiol (EDT), which has been shown to passivate electron traps in PbS QD films [110, 69] as well as a thermal oxidation treatment, which has been shown to form insulating oxide shells around the nanocrystals to affect charge transport [105, 83]. Importantly, the EDT treatment also renders the QD film insoluble to chloroform, which permits the subsequent spin-casting of PCBM (15 mg mL^{-1} in chloroform) without damaging the underlying QD film. By applying these treatments, we are able to directly modify the charge transport properties of the QD film as well as the charge dynamics at the organic/QD interface to enable optimization of device performance.

4.2 Device Fabrication and Testing

A gold interdigitated electrode array (L = 10μm, W = 59 mm) was fabricated on a substrate of D263 borosilicate glass by e-beam evaporation and liftoff. PbS QDs with a first optical excitation wavelength of $\lambda = 1270$ nm were synthesized according to a procedure described in Ref. [83]. The as-synthesized QDs were precipitated from solution with methanol and butanol and then recast into n-butylamine (BA) for 3 days in order to exchange the native oleic acid (OA) ligands with shorter BA

ligands. The QD solution was subsequently precipitated and redissolved into octane at a concentration of 75 mg mL^{-1}. The spin-cast films of BA-treated QDs were then treated in a solution of 0.02% EDT in acetonitrile for 30 seconds followed by a short rinse in pure acetonitrile. Two layers of QDs deposited in this manner resulted in a total film thickness of 110 nm. For bi-layer devices, a 15 mg mL^{-1} solution of PCBM in chloroform was spin-cast at 2000 RPM for 60 seconds.

Current-voltage characteristics were measured with a Keithley 6487 Picoammeter both in the dark and under illumination from a 90 mW Newport LQD-1060 laser diode (emission centered at $\lambda = 1060$ nm).

To measure time response, the LQD-1060 laser diode, modulated at 5 Hz, was used to illuminate the devices and a Femto DHPCA-100 High Speed Current Amplifier and Tektronix 3054b oscilloscope were used to measure the photocurrent decays.

For quantum efficiency measurements, monochromatic light was generated by using a 1000 W quartz tungsten halogen (QTH) lamp that was optically chopped and focused into an Acton Spectrapro 300i monochromator. A calibrated Germanium photodetector was used to measure the optical power of the spectrally-resolved output. At $\lambda = 1060$ nm, the optical power density was measured to be 21.5μW cm^{-2}. A lock-in amplifier provided with the reference signal from the optical chopper ($f = 30$ Hz) was used to measure the AC photocurrent. The absorption data used for the calculation of IQE was taken with a Cary 5e spectrophotometer. All absorption curves were base-line corrected at $\lambda = 1600$ nm.

An Ithaco 1211 Current Amplifier and a Stanford Research Systems Model SR785 Dynamic Signal Analyzer were used to directly measure device noise current (I_n) in

the dark at $f = 10$ Hz.

4.3 Basic Operation of a PbS QD Photoconductor

We first characterize the performance of a typical device consisting only of a PbS QD film (see Figure 4.1(a)). External quantum efficiency (EQE) >1000% is readily accessible at V_{bias}>10 V (see Figure 4.1(b)) as was first reported in Ref. [23]. This high sensitivity is attributed to the presence of long-lived electron traps [69] that manifest a high photoconductive gain in the structure. Since the response speed is inversely related to the recombination rate within the photoconductor, the presence of these long-lived traps also result in a very slow response speed (f_{3dB} <20 Hz).

We next consider the stability of these devices with exposure to air. The measured EQE as a function of the time over which the device was exposed to an ambient environment is shown in Figure 4.2(a). The EQE is observed to be <100% prior to any air exposure. A brief exposure of 5 seconds to the ambient environment, however, is observed to result in a substantial improvement in quantum efficiency (EQE >1000%). This change is attributed to the formation of oxidation products on the QD surfaces ($PbSO_3$, $PbSO_4$, etc.) that act as electron traps [69]. The sensitization of PbS QD films by exposing them to air is thus critical to attaining the high quantum efficiency commonly associated with these structures. The magnitude of the photoresponse remains fairly stable with further air exposure. The peak in EQE, however, blue shifts with time as the surfaces of the QDs become further oxidized and the effective QD core diameter shrinks. The evolution of the device characteristics with time is shown in Figure 4.2(b)

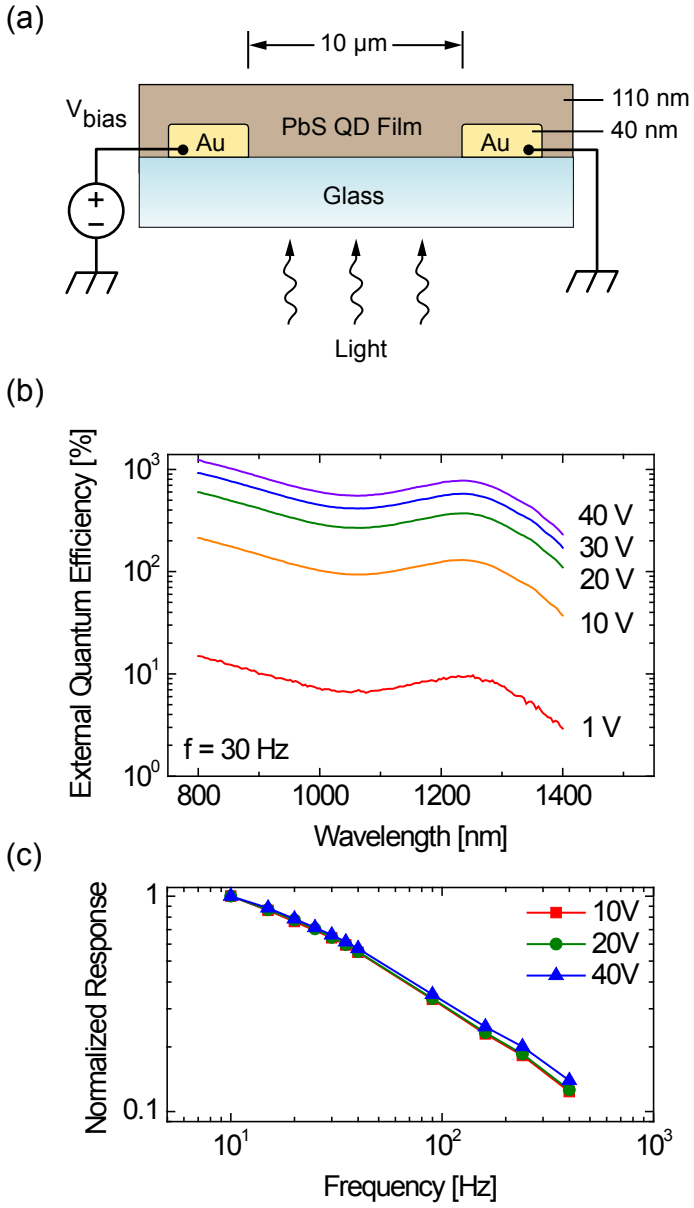

Figure 4.1: (a) Section view schematic of a PbS QD photoconductor. (b) EQE as a function of wavelength for a range of biasing conditions. (c) Normalized response vs. modulation frequency for a range of biasing conditions.

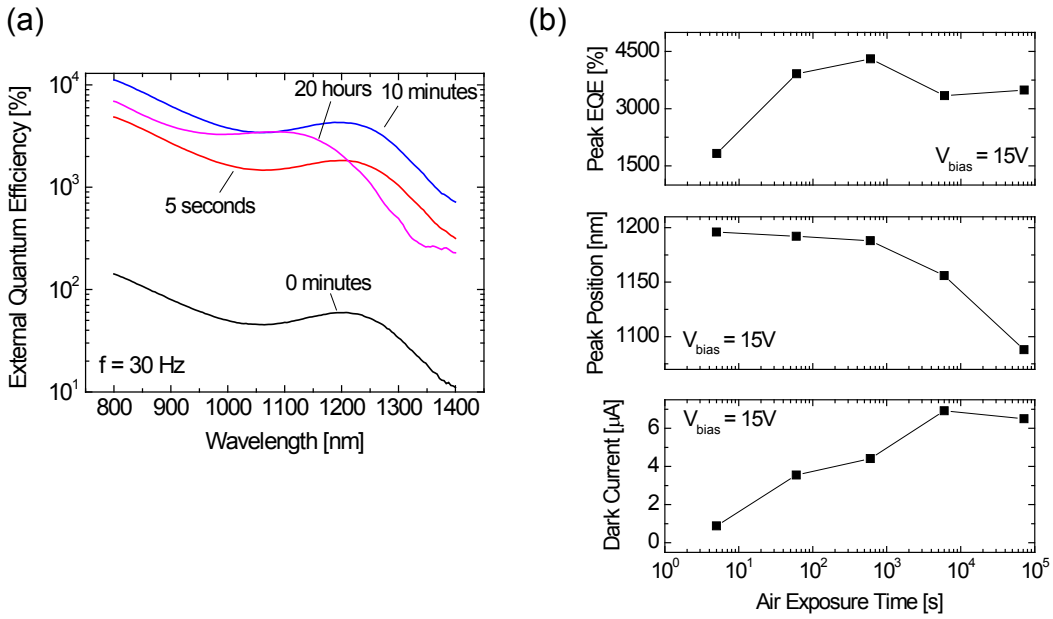

Figure 4.2: (a) EQE as a function of wavelength for an EDT PbS QD photoconductor before and after exposure to ambient air. (b) Peak EQE, wavelength and dark current as a function of air exposure time.

4.4 Bilayered PbS QD/PCBM Photoconductor

The hybrid PbS QD/PCBM bi-layer device structure and its energy band diagram are shown in Figure 4.3. The gold electrodes serve as ohmic contacts to the p-type PbS QD film. Photoconductive gain in the device can be described by τ/T_r, where τ is the electron-hole recombination lifetime and T_r is the transit time of the majority carrier across the 10μm channel between the gold electrodes. The presence of the PbS QD/PCBM interface creates an interfacial recombination mechanism that competes with the bulk recombination processes present in the QD film, thus affecting both gain and bandwidth (see Figure 4.3(b)).

The long oleic acid ligands on the as-synthesized PbS QDs were first replaced with butylamine ligands in solution, and then by ethanedithiol ligands (EDT) following

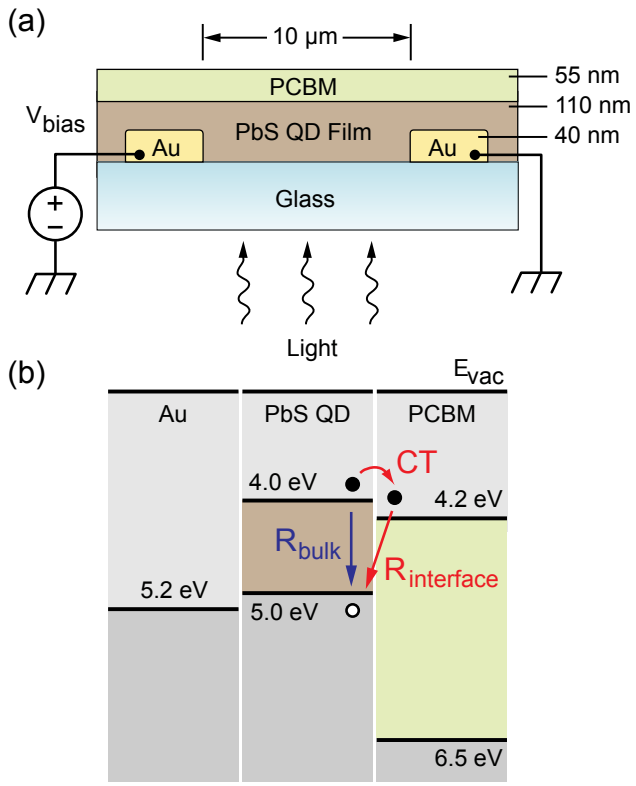

Figure 4.3: (a) Section view schematic of bilayered device structure. Gold electrodes were evaporated onto a 2 nm Titanium adhesion layer (not shown). The W/L ratio of the interdigitated electrode is 5900. (b) Electronic band diagram of the device. HOMO and LUMO levels for PbS QDs and PCBM were taken from [39] and [10], respectively. R_{bulk} represents the bulk recombination processes in the QD film (dashed arrow). The interfacial recombination process (solid arrows) consists of a charge transfer event (CT) followed by recombination across the interface ($R_{interface}$).

deposition of the QD film (additional details on device fabrication are available in the experimental section). The EDT-treated QD films were then subjected to exposure in different environments prior to PCBM deposition. 'Pristine' films were maintained in an inert nitrogen atmosphere at room temperature throughout all fabrication and testing steps. '70 °C' and '110 °C' films refer to films that were annealed for 30 minutes in an air environment at 70 °C or 110 °C, respectively, in order to partially oxidize the nanocrystals. The annealed films were treated in an EDT solution a final time just prior to PCBM deposition in order to ensure complete passivation of the oxidized QDs.

Table 4.1: Summary of photosensitivity figures of merit for devices consisting of pristine and annealed QD films. All measurements were taken at a bias of 15 V. EQE, IQE, R and D^* are reported at the wavelength of the first excitonic peak (pristine: $\lambda = 1268$ nm, 70 °C: $\lambda = 1156$ nm, 110 °C: $\lambda = 1080$ nm) and under an illumination intensity of $P_o = 21.5\mu$W cm^{-2}.

Device	I_{dark} [A]	I_{light}/I_{dark}	EQE [%]	IQE [%]	R [A W^{-1}]	I_n[a] [A Hz$^{-1/2}$]	D^* [Jones]
pristine	1.68×10^{-6}	254	678	8.50×10^{3}	6.93	4.62×10^{-11}	1.15×10^{10}
pristine/PCBM	3.92×10^{-6}	23	57	7.19×10^{2}	0.59	1.80×10^{-11}	2.50×10^{9}
70 °C	1.27×10^{-7}	3085	112	1.40×10^{3}	1.04	2.43×10^{-12}	3.29×10^{10}
70 °C/PCBM	1.16×10^{-7}	1963	79	9.96×10^{2}	0.74	-	-
110 °C	1.09×10^{-9}	30364	11	1.46×10^{2}	0.09	2.13×10^{-14}	3.33×10^{11}
110 °C/PCBM	1.02×10^{-9}	27062	5	6.90×10^{1}	0.04	-	-

[a] Noise current was measured at $f = 10$ Hz.

Several key figures of merit were measured in order to assess the performance of single layer devices, consisting only of the QD film, as well as bi-layer QD/PCBM devices. The time response, quantified by the 3-dB bandwidth (f_{3dB}), is calculated by taking the inverse of the time required for a pulse of photocurrent to decay to $1/e$ of its initial value. Several figures of merit to describe photosensitivity were also measured (see Table 4.4). The spectral photon-to-electron conversion efficiency, referred to as the external quantum efficiency (EQE), is measured to characterize device performance across a range of wavelengths. The related metric of internal quantum efficiency (IQE), representing the extent of internal photoconductive gain in the device, is calculated according to $IQE = EQE/(1 - T)$, where T is the percentage of light that is optically transmitted through the film. Responsivity (R), in units of Amps per Watt, is calculated using the equation: $R = EQE \times q/(hv)$, where $q = 1.602 \times 10^(-19)$ C. Finally, the important photosensitivity metric of specific detectivity (D^*), in units of cm $Hz^{1/2}$ W^{-1} or "Jones", is measured. D^* is a measure of the signal-to-noise ratio of a photodetector over a 1 Hz bandwidth normalized to the detector area and can be calculated using the equation, $D^* = (\sqrt{A_D \Delta f})/I_n)R$ where A_D is the active area of the device, Δf is the bandwidth over which the noise current is measured, I_n is the noise current and R is the responsivity of the device.

4.4.1 Current-Voltage Characteristics

The current-voltage characteristics of each device are plotted in Figure 4.4. The current is measured to a maximum bias of 15 V (corresponding to an electric field strength of 1.5×10^4 V cm^{-1}) both in the dark and under illumination at $\lambda = 1060$

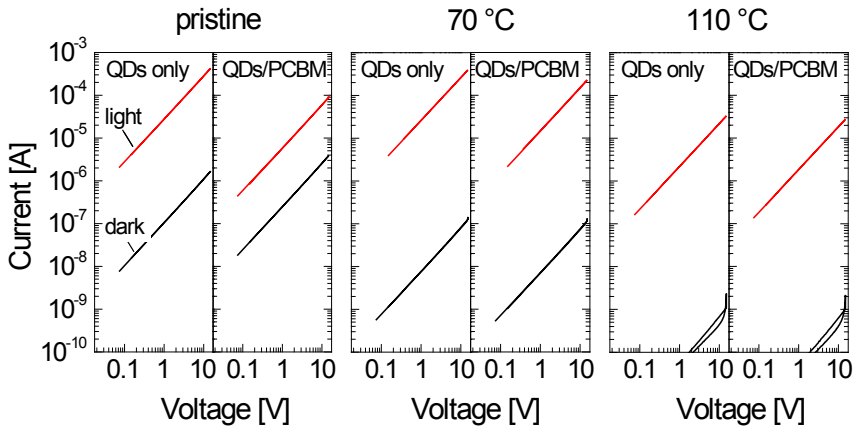

Figure 4.4: Current-voltage characteristics for devices consisting of pristine QD films and films annealed in air for 30 minutes at 70 °C and 110 °C. Dark currents are shown as dashed lines and light currents, measured under illumination from a 90 mW diode laser at wavelength $\lambda = 1060$ nm, are shown as solid lines.

nm. At this wavelength approximately 8% of the light is absorbed, and all of this absorption is due to the QD film. All devices exhibit a linear response over the voltage range tested. For the single-layer pristine device (without a PCBM film), a dark current of 1.7μA is measured, corresponding to a linear current density of 290 nA per centimeter of channel width (nA cm^{-1}). Annealing at 70 °C and 110 °C reduces the current response to 21 nA cm^{-1} and 0.19 nA cm^{-1}, respectively. The reduction in dark current with annealing is attributed to reduced mobility in the QD film as insulating oxide shells grow around the constituent QDs [83]. I_{light}/I_{dark} is found to increase with annealing temperature from a ratio of 250, for the pristine device, to 3100 and 30,000 for the devices annealed at 70 °C and 110 °C, respectively. These observations suggest that the overall photosensitivity of individual QD films can be improved by means of air-annealing treatments.

The addition of the PCBM layer to the pristine device results in an order-of-

magnitude reduction in I_{light}/I_{dark}. We attribute this to the introduction of the interfacial recombination process shown in Figure 4.3(b). Accelerated electron-hole recombination at the PbS QD/PCBM interface reduces the lifetime of trapped electrons and hence the photoconductive gain. The addition of the PCBM layer to the devices annealed at 70 °C and 110 °C produces only a small difference in I_{light}/I_{dark}, suggesting that the presence of an oxidized shell around the QDs inhibits the interfacial charge transfer and recombination processes.

4.4.2 Transient Response

To further investigate the effects of interfacial recombination and QD oxidation on device performance, the transient responses of these devices were measured. The devices were illuminated with a modulated laser source with emission at $\lambda = 1060$ nm, and the resulting photocurrent decays were recorded on an oscilloscope (Figure 4.5(a)). A slow modulation frequency of $f = 5$ Hz ensures that the device response reaches steady-state under each illumination pulse and that the full photocurrent decay trace can be captured. The photocurrent decays are bias-independent and are well-fit by double exponential functions (Figure 4.5(b)). The fact that the decay responses do not shorten with increased bias suggests that photocurrent decay is determined by the recombination processes in the devices and not by carrier sweep-out. For the single-layer pristine QD device, the dominant time constant is varies from 100 μs to 500 μs with decreasing illumination intensity. A tail with a time constant of (7 ± 3) ms is also observed and becomes increasingly significant to the overall response speed at relatively low light intensities (P_o <¡ mW cm^{-2}). Similar time

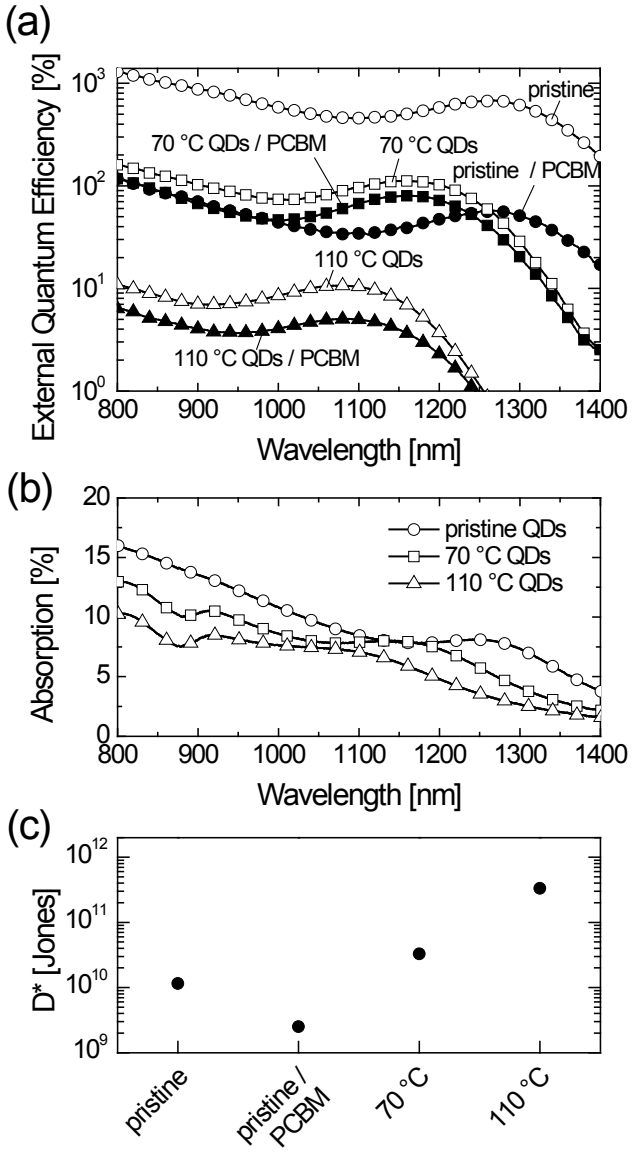

Figure 4.5: (a-b) Normalized photocurrent decay measurements under a bias of V_{bias} = 15 V and modulated (5 Hz) illumination from a 90 mW laser (λ = 1060 nm). (c) Extracted time constants for decays from pristine and pristine/PCBM devices as a function of device bias. τ_1 and τ_2 represent the fast and slow time constants extracted from a double-exponential fit from the pristine QD device. The pristine/PCBM device was fitted to a single exponential decay with a time constant of τ. (d) Device bandwidth versus illumination intensity.

constants were measured for devices made with annealed QD films, with and without the presence of PCBM. These time constants are attributed to bulk recombination processes in the QD film. The pristine QD/PCBM bi-layer device uniquely exhibits a dominant fast decay with a time constant $(0.5 \pm 0.1)\mu$s which we attribute to the fast interfacial recombination shown in Figure 4.3(b). We note that this fast decay component is substantially diminished in devices that were subjected to an air annealing treatment, again indicating that the presence of oxide shells around the QDs inhibits the interfacial recombination process.

To characterize the transient performance of these devices, 3-dB bandwidths (f_{3dB}) are extracted from these decay measurements and are plotted in Figure 4.5(c) as a function of incident light intensity. In the case of single layer devices, bandwidth follows a square root dependence with increasing intensity. At approximately $P_o = 5$ mW cm^{-2}, the bandwidth of the bi-layer device begins to exhibit an advantage over the single layer pristine device. At P_o >50 mW cm^{-2}, the 3-dB bandwidth of the bi-layer device increases well beyond 100 kHz, while the single layer pristine device remains below 10 kHz. This improvement in response speed is due to the fast bimolecular recombination rate provided by the PbS QD/PCBM interface. The onset of this improvement with increasing light intensity is attributed to the presence of electron traps on the PbS QDs. Under higher light intensities the mobility of electrons increases as these trap states become filled, enabling a greater percentage of photo-generated electrons to diffuse to the PbS QD/PCBM interface. For the 110 °C-annealed devices, an advantage in bandwidth with the PCBM layer is observed for illumination intensities greater than 100 mW cm^{-2}. This higher onset of strong

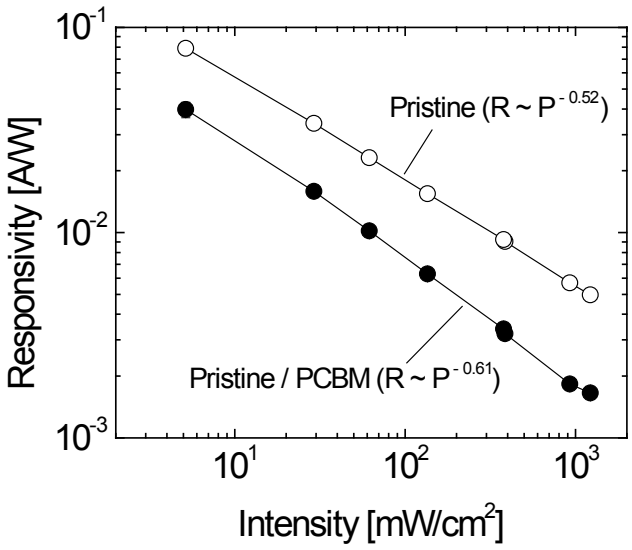

Figure 4.6: Responsivity versus illumination intensity.

interfacial recombination is attributed to reduced carrier mobility in 110 °C-annealed devices.

4.4.3 Intensity-Dependence of Responsivity

The photocurrent response of each device characterized in this study follows a square-root dependence with intensity, indicating a bimolecular recombination mechanism[121]. Consequently, responsivity and therefore specific detectivity follow inverse square-root dependence with increasing intensity (see Figure 4.6). Thus, we observe a fundamental trade-off between bandwidth and photosensitivity: under high illumination intensities, bandwidth will be high but photosensitivity will be low, and vice-versa under low intensity. In the case of the pristine bi-layer device, for example, the 3-dB bandwidth at $P_o = 21.5\mu$W cm^{-2} is very low (<100 Hz) while photosensitivity, as quantified by specific detectivity, is measured to be 2.5×10^9 Jones. This is compara-

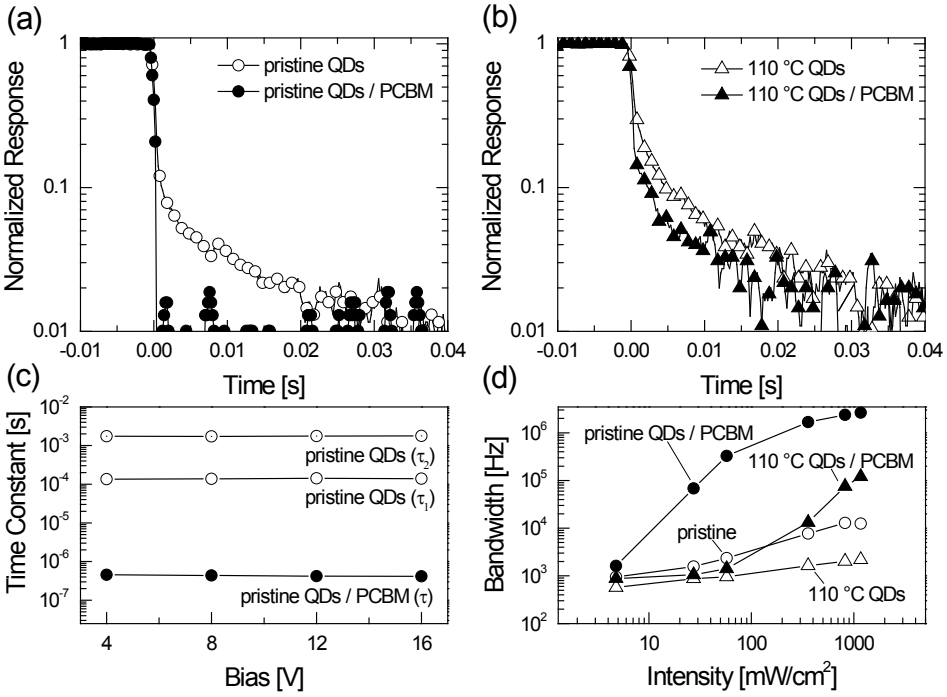

Figure 4.7: (a-b) Normalized photocurrent decay measurements under a bias of $V_{bias} =$ 15 V and modulated (5 Hz) illumination from a 90 mW laser ($\lambda = 1060$ nm). (c) Extracted time constants for decays from pristine and pristine/PCBM devices as a function of device bias. τ_1 and τ_2 represent the fast and slow time constants extracted from a double-exponential fit from the pristine QD device. The pristine/PCBM device was fitted to a single exponential decay with a time constant of τ. (d) Device bandwidth versus illumination intensity.

ble in performance to epitaxially grown lead-salt photoconductors operating at room temperature [60]. Under a much higher illumination intensity of $P_o = 57$ mW cm^{-2}, however, the bandwidth becomes very high ($f_{3dB} \approx 330$ kHz), but the photosensitivity is diminished to 4.4×10^7 Jones. Proper consideration of device application must therefore take into account the range of intensities under which light is to be detected.

4.4.4 Spectrally-Resolved Quantum Efficiency

To characterize the photosensitivity of these devices across SWIR wavelengths, the spectrally resolved quantum efficiency was measured and is presented in Figure 4.7. The position of the first excitonic peak is observed to blue-shift with increasing annealing temperature from $\lambda = 1270$ nm, for the pristine film, to $\lambda = 1156$ nm and $\lambda = 1080$ nm for the 70 °C and 110 °C-annealed films, respectively (see Figure 4.7(b)). This blue-shift is due to a decrease in the effective core diameter of the QDs as their surfaces become increasingly converted to oxide compounds [83]. The single-layer device consisting only of a pristine film of QDs yields the highest EQE of 680%, corresponding to a responsivity of 6.9 A W^{-1} or an IQE of 8500%. The annealed films exhibit a considerably lower EQE (112% for 70 °C and 10.6% for 110 °C at their first excitonic peaks) due to poorer charge transport which increases the transit time of holes and therefore reduces gain. The presence of a PCBM layer on top of the QD film results in small changes to the annealed devices, but a large reduction in the EQE of the pristine device to 57% ($IQE = 718\%$). This is again consistent with the occurrence of enhanced recombination provided by the PbS QD/PCBM interface.

4.4.5 Specific Detectivity

In order to determine specific detectivity, the noise current in the device must first be determined. Measurements of the noise current as a function of frequency were obtained at room temperature under dark conditions with a noise spectrum analyzer (see Figure 4.8(a)). Expected internal sources of noise include Johnson-Nyquist noise ($i_{J-N} = \sqrt{4k_BT\Delta f/R}$), which results from random thermally-induced

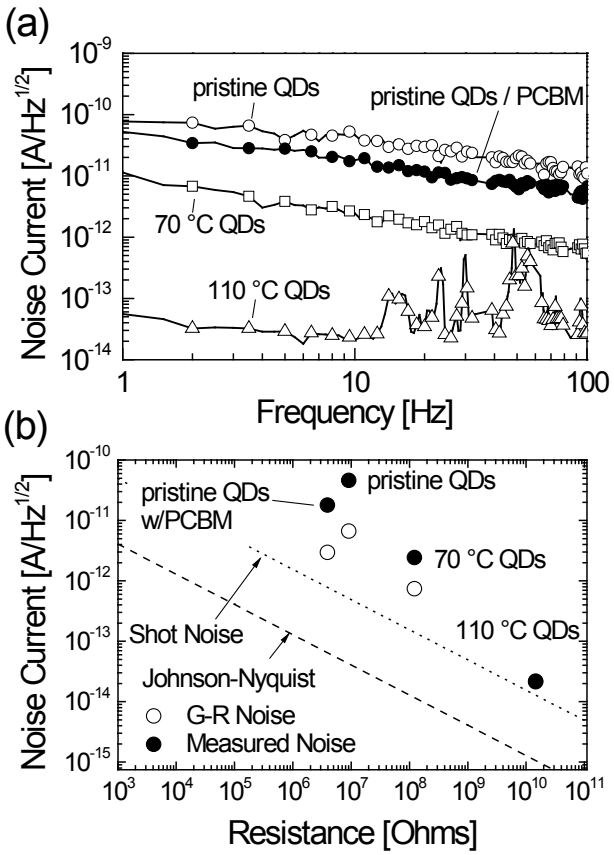

Figure 4.8: (a) Noise current as a function of frequency. (b) Noise current versus device resistance as compared with calculated Johnson-Nyquist and dark current shot noise.

current fluctuations, and generation-recombination noise ($i_{G-R} = \sqrt{4qIG\Delta f}$), which is due to variations in the conductivity of the device originating from the random generation and recombination of carriers. At low frequencies the noise current in each device follows a $f^{-1/2}$ dependence, indicating the presence of so-called "1/f" or "pink" noise, attributed to the presence of surface trap states and commonly observed in infrared detectors [60]. We note that measured noise currents exceed those predicted to arise from Johnson-Nyquist or generation-recombination noise, suggesting that 1/f noise is the dominant noise mechanism at low frequencies (see Figure 4.8(b)).

We next consider the effect of QD oxidation on the noise current for the single layer devices consisting only of the QD film. Measured at $f = 10$ Hz, air annealing reduces noise current from 4.62×10^{-11} A Hz$^{-1/2}$, for the pristine device, to 2.43×10^{-12} A Hz$^{-1/2}$ and 2.13×10^{-14} A Hz$^{-1/2}$ for the 70 °C and 110 °C-annealed devices, respectively. The decrease in noise with increasing device resistance can largely be attributed to the reduction of Johnson-Nyquist noise and shot noise. Specific detectivity is calculated to increase with the air annealing treatment from 1.2×10^{10} Jones for the pristine device to 3.3×10^{11} Jones for the device annealed at 110 °C. The reduction in responsivity that results from the air annealing treatment is thus overcompensated for by the reduction in noise, allowing an improvement in D^* of over an order of magnitude.

In the case of the pristine PbS QD bi-layer device, the QD film is slightly more conductive than the single-layer device. This would be expected to result in an increase of both Johnson-Nyquist noise and shot noise. However, the measured noise current is observed to decrease by a factor of 2.6 (see Figure 4.8(b)). This observation

suggests that the reduction in the population of trapped electrons in the QD film due to the PbS QD/PCBM interface directly affects the $1/f$ noise mechanism. For these bi-layer devices, D^* decreases by almost an order of magnitude to 2.5×10^9 Jones, despite the reduction in noise.

Measurements of the specific detectivity (D^*) are shown in Figure 4.7(c). D^* increases with the air annealing treatment from 1.2×10^{10} Jones for the pristine device to 3.3×10^{11} Jones for the device annealed at 110 °C. The reduction in responsivity that results from the air annealing treatment is thus overcompensated for by the reduction in noise, allowing an improvement in D^* of over an order of magnitude.

4.5 Conclusion

We demonstrated a hybrid organic/QD planar photodetector consisting of discrete layers of PbS QDs and PCBM. Fast operation (f_{3db} >300 kHz) is achieved under sufficiently high illumination power ($P_o = 57$ mW cm^{-2}) with the introduction of a fast interfacial recombination mechanism to reduce carrier lifetime. We compared the advantages and disadvantages of the hybrid bi-layer structure with those of single layer devices, consisting only of the chemically treated QD film. We find that, although the bi-layer structure allows for improved time response, the single layer structure is preferred for maximizing photosensitivity. Chemical modification of the QD film through oxidation enables control over the charge transport properties of the device leading to a specific detectivity (D^*) as high as 3.3×10^{11} Jones. Oxidation of the QD film, however, is found to substantially inhibit the PbS QD/PCBM interfacial recombination process, reducing the advantage in bandwidth provided by PCBM. The

bi-layer photodetector structure facilitates tailoring of the photodetector performance and exemplifies a convenient device structure for studies of carrier dynamics at hetero-interfaces in other material systems.

Chapter 5

Bias-Stress Effect in PbS QD Field-Effect Transistors

In the previous chapter, photoconductors based on chemically-treated films of PbS QDs were described. The efficient operation of these devices critically depends on the charge transport properties of the film as well as the presence of charge traps on QD surfaces. In the present chapter, we thoroughly investigate these properties of the QD film in a field-effect transistor configuration.

5.1 Introduction

Although much progress has been made in advancing the performance of opto-electronic devices that incorporate colloidal quantum dot (QD) thin films, aspects of charge transport in these devices remain poorly understood. In several recent studies of lead chalcogenide QDs in field-effect transistor (FET) structures, a rapid

bias-stress effect, or shift in threshold voltage (V_T) with the application of a gate bias, was observed [122, 123, 124, 125, 110, 126]. This effect manifests as a stretched exponential decay in the drain-source current (I_{DS}) after a bias is applied to the gate electrode. The instability associated with bias stress precludes practical applications of QD FETs and even complicates the characterization of their performance at the research level. For example, in the case of alkanedithiol-treated PbSe QD FETs, the speed and extent of this decay necessitated Liu and coworkers to perform FET measurements as rapidly as possible (<500 ms) in order to minimize the distortion of transfer and output characteristics [124].

The origins of the bias-stress effect have been extensively studied in the past two decades for FETs containing organic small-molecule [93, 127], conjugated polymer [128, 129, 130, 131, 132, 133], metal oxide [134], and amorphous silicon (a-Si:H) [135, 136] charge transport layers. In contrast, only a few reports directly address this phenomenon in QD FETs. In the case of PbSe QD FETs in which the QDs were passivated by either oleic acid [122], alkanedithiols [123, 124, 110, 126], or amine ligands [125], screening of the gate field by charge trapping at or near the semiconductor/dielectric interface was identified as the most likely mechanism for the bias-stress effect. In these studies, however, the dynamics of the stressing process were not quantitatively characterized and uncertainty remains regarding the nature of the trapped charge. In particular, it remains unclear whether the charge that screens the gate field accumulates in surface states at the QD/dielectric interface or within the QD film itself. In organic FETs, hydroxyl groups at the surface of SiO_2 have been implicated as electron-trapping sites [137] and surface-bound water molecules have been

identified to act as hole traps [138, 133]. On the other hand, the presence of QD surface defects [139, 140, 141, 142, 121] or the organic ligands intended to passivate QD surfaces [143, 144, 145], may also act as trapping sites.

In this chapter, we investigate the origin of the bias-stress effect in EDT-treated PbS QD FETs by studying the dynamics of the stressing process as a function of drain bias, gate bias, temperature, and QD size. In addition to a standard bottom-gate bottom-contact FET configuration, we utilize a top-gate bottom-contact configuration with a series of dielectric materials. Importantly, this approach provides a way to isolate the influence of the QD/dielectric interface on transistor performance and thereby enables the study of bulk properties of the QD film. We choose to study films of EDT-treated PbS QDs because they have been comparatively less well-studied in FET geometries than PbSe QDs, yet have been central to several recent optoelectronic device demonstrations [49, 26, 24]. From the current-voltage response of the FETs we find that top-gated structures exhibit ambipolar operation with typical mobilities on the order of $\mu_e = 8 \times 10^{-3}$ cm^{2}V^{-1}s^{-1} in n-channel operation and $\mu_h = 1 \times 10^{-3}$ cm^{2}V^{-1}s^{-1} in p-channel operation. The bias-stress characteristics are observed to be qualitatively similar to those reported in EDT-treated PbSe QD FETs [110, 124]. A key observation is that the stress and recovery characteristics are similar in devices made with a series of different dielectrics, including parylene-C, poly(methyl methacrylate) (PMMA) and polystyrene, which suggests that charge trapping occurs within the QD film itself, and is not due to interface states at particular QD/dielectric interface. The measurements of bias-stress-induced time-dependent decays in the drain-source current (I_{DS}) are fit well to stretched exponential functions

and the time constants of these decays in n-channel and p-channel operation are found to follow thermally activated Arrhenius behaviour. Our results are consistent with a mechanism in which field-induced morphological changes within the QD film result in screening of the applied gate field. Possible specific physical origins for electron and hole traps in the EDT-PbS QD system are considered and discussed.

5.2 Fabrication and Testing of PbS QD FETs

Preparation of QD Films: PbS QDs were synthesized according to a procedure described elsewhere [83]. The diameters of the QDs are estimated according to the position of their lowest energy absorption peaks. For the fabrication of all FET structures described in this study, PbS QDs with a band-edge absorption peak at wavelength $\lambda = 1155$ nm (corresponding to a QD energy gap of $E_g = 1.1$ eV and a QD diameter of $d = 4.40$ nm [146]) are used, unless otherwise specified. The as-synthesized QDs were precipitated twice from solution with acetone and butanol and recast into hexane. Following a third crash-out, the QD precipitate was recast into octane at a concentration of 25 mg mL^{-1}. A single film was spun at 1500 RPM for 60 seconds to produce a ≈ 15 nm-thick film. The gold contacts at the edge of each sample were swabbed clear with octane to ensure good electrical access. The films were then treated in a solution of 0.1% EDT in acetonitrile for 30 seconds followed by a short rinse in pure acetonitrile.

Fabrication of FETs: Gold interdigitated electrode arrays (with length and width of $L = 10$ m and $W = 12$ mm, respectively) were fabricated on substrates of D263 borosilicate glass as well as on degenerately doped silicon with a 500 nm ther-

mally grown SiO_2 layer. The electrode films were deposited by e-beam evaporation of 2.5 nm thick film of Ti followed by 45 nm thick film of Au and then patterned with liftoff. Following solvent cleaning, the substrates were subjected to oxygen plasma for 30 seconds. Glass substrates were submerged overnight in a 0.2 M solution of (3-mercaptopropyl)trimethoxysilane (MPTMS) in toluene to grow a self-assembled monolayer to promote adhesion of the QD films. After 1 minute of sonication in isopropanol, the substrates were dried with nitrogen and transferred into a nitrogen environment for the deposition of the QD film. The gate dielectric was deposited as described below and an aluminium gate was deposited by thermal evaporation through an aligned shadow mask. For the devices on silicon substrates, no surface treatment was employed prior to the deposition of the QD film. A contact to the underlying silicon was made by scoring through the top SiO_2 surface and applying a small amount of silver paste.

Preparation of Dielectrics: Films of parylene-C were formed using diX-C dimer from Daisan Kasei in a homemade CVD reactor. The deposition pressure of the vacuum system was approximately 10^{-3} Torr. Electronic grade polystyrene (Polymer Source Inc.) with M_w = 221,500 and M_w/M_n = 1.04 was dissolved in butyl acetate (50 mg mL^{-1}) and spin-cast at 2000 RPM. For poly(methyl methacrylate) dielectrics, 950PMMA A4 Resist, purchased from Micro-chem, was spin-cast at 1000 RPM. Following deposition of PMMA and polystyrene films, the samples were stored in an ultra-high vacuum environment ($\tilde{1}0^{-8}$ Torr) overnight to remove solvent. Parylene-C, PMMA and polystyrene film thicknesses were measured to be 478 nm, 465 nm and 330 nm, respectively.

Field Effect Transistor Characterization: To characterize the capacitance for each gate dielectric, test capacitors were made consisting of the identically prepared dielectric films sandwiched in between an ITO bottom-contact and an aluminium top-contact. A Solartron 1260 Impedance Analyzer was then used to directly measure the gate capacitance at a frequency of $f = 37$ Hz. The capacitances of the parylene-C, PMMA and polystyrene films were measured to be 6.2, 5.7 and 5.9 nF cm^{-2}, respectively. An Agilent 4156C Semiconductor Parameter Analyzer was used to acquire transfer and output characteristics. For extraction of the field-effect mobility, the total stress time of transfer characteristic sweeps was limited to 400 ms.

For stress and recovery measurements, the Agilent 4156C was operated under computer control in order to ensure consistency of the measurement sequence. Several short (10 ms) pulsed measurements of drain-source current under the desired bias conditions were taken within a 2 hour period before the application of the stress condition in order to ensure that the device was in an unstressed state and also to provide the initial drain-source current level for normalization. The current was measured continuously while the gate bias was applied in order to capture the decay in current as the device became stressed. Immediately after, a series of pulsed measurement identical to the initial normalization current measurements tracked the recovery of the drain-source current level to its initial condition.

5.3 FET Characterization

Bottom-gate / bottom-contact FETs on Si/SiO_2 substrates were fabricated and tested in order to establish consistency between the QD materials used in this study

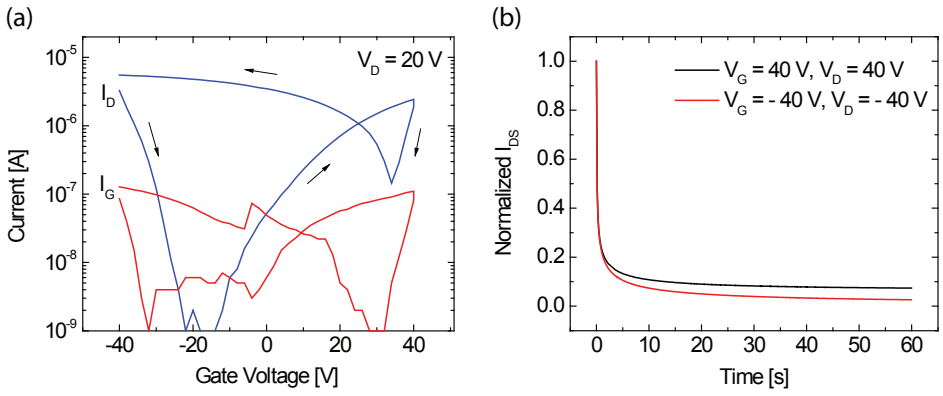

Figure 5.1: (a) Transfer characteristic for EDT PbS QD FET. (b) Normalized I_{DS} under an applied gate bias as a function of time.

and the literature. These devices exhibit ambipolar operation (see Figure 5.1), consistent with recent reports on PbS [123] and PbSe QD-based FETS [124]. We also note that after the application of the gate bias, I_{DS} in both n-channel and p-channel modes exhibits a stretched-exponential decay on a time scale similar to that previously observed in PbSe QD FETs [110, 124].

To assess the role of the QD/dielectric interface in determining device performance, including the occurrence of bias stress, we now investigate a series of top-gate / bottom-contact FETs with three different dielectrics: parylene-C [147, 93], PMMA [87] and polystyrene [148]. Each of these dielectrics has been used in organic FET transistor studies specifically to avoid the formation of interface states associated with surfaces of SiO_2 dielectric layers. The device structure as well as the molecular structures for each of the dielectric materials used are shown in Figure 5.2.

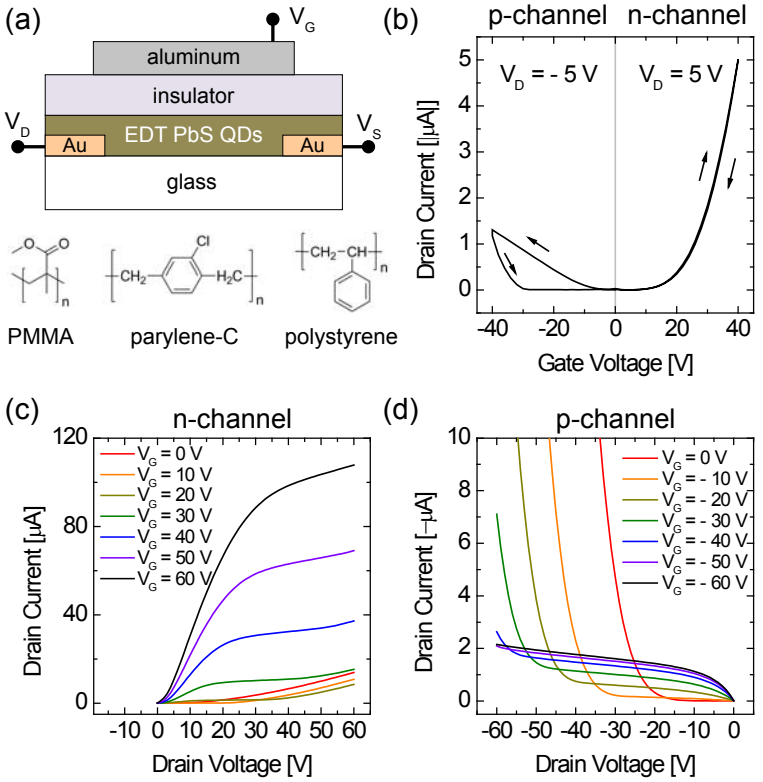

Figure 5.2: (a) Schematic of device structure and molecular structures of parylene-C, PMMA and polystyrene, respectively, which are used as gate dielectric materials. (b) Ambipolar transfer characteristics of a representative EDT PbS QD FET made with a PMMA dielectric. The p-channel and n-channel sweeps were measured separately and with a break of several minutes in between in order to minimize distortion. (c-d) Output characteristics for negative and positive gate biases, respectively.

5.3.1 Current-Voltage Characteristics

The output characteristics (I_{DS} versus V_D) for a representative device that incorporates a PMMA dielectric layer are shown in Figure 5.2 for p-channel and n-channel operation, respectively. Saturation in the magnitude of drain-source current is observed for sufficiently high drain biases, corresponding to the pinch-off of the hole and electron channels. The transfer characteristics (I_{DS} versus V_G) in the linear operating regime for the same device are shown in Fig. 1b. To minimize the influence of bias stress on FET characteristics, such as threshold voltage (V_T) and mobility (μ), the single current-voltage sweeps are limited to <400 ms. Additionally, sweeps to positive and negative gate biases are conducted separately and with a break of several minutes in between. To characterize threshold voltage and mobility, the initial sweep toward higher $|V_G|$ is used. We note that considerable hysteresis is observed in p-channel mode, while the forward and backward sweeps in n-channel mode are consistent. The value that we extract for the mobility in p-channel operation is thus likely to be an underestimation of the actual hole mobility in the device.

Threshold voltages for both n-channel and p-channel operation are extracted by extrapolating the $I_{DS} - V_G$ sweeps shown in Fig. 1b to a current level of zero. Field-effect mobilities are then calculated assuming a linear drain-source current given by the equation [86]:

$$I_{DS} = \frac{W}{L}\mu C_i(V_G - V_T)V_D \tag{5.1}$$

The parameters L and W are the length and width of the FET channel, respectively, and C_i is the dielectric capacitance (F cm^{-2}). We obtain mobilities of $\mu_e = 8 \times 10^{-3}$ cm^{2}V^{-1}s^{-1} in n-channel operation and $\mu_h = 1 \times 10^{-3}$ cm^{2}V^{-1}s^{-1} in p-channel

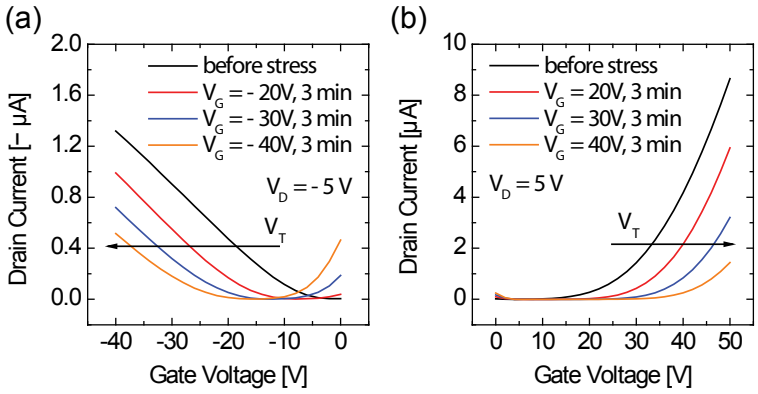

Figure 5.3: (a-b) Transfer characteristics for a top-gated device that incorporates a PMMA dielectric in n-channel and p-channel operation, respectively, exhibiting a shift in threshold voltage, ΔV_T, following sustained gate bias.

operation (averaged over 8 devices). Similar ambipolar characteristics are observed in devices consisting of parylene-C and polystyrene dielectrics.

5.3.2 Bias Stress

We next characterize the bias-stress effect in top-gated FET structures with different dielectric materials. We again first consider a representative FET with a PMMA dielectric. The threshold shift, ΔV_T, is illustrated in Figure 5.3 for different stressing conditions. We note that for sufficiently high $|V_G|$, the slope of the transfer characteristic remains approximately unchanged with stress, indicating that carrier mobility remains largely unchanged by the stressing process. We also note that these shifts do not represent the ultimate ΔV_T reached during the stressing cycle due to a delay before acquiring the transfer curves, during which time the device is able to recover to an extent.

To more accurately characterize the bias stress effect, we measure the decay in I_{DS} continuously under an applied gate bias. The decay in I_{DS}, normalized to its

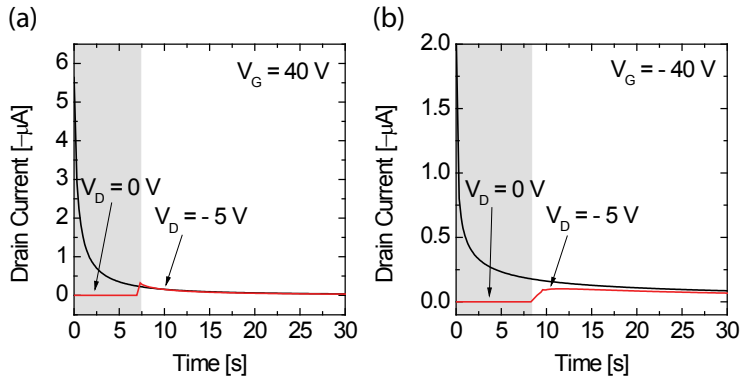

Figure 5.4: Drain current of EDT-treated PbS QD FET with PMMA dielectric in n-channel (a) and p-channel (b) operation. The black curves represent measurements in which $V_G = \pm 40$ V and $V_D = -5$ V are applied simultaneously. The red curves represent measurements in which the application of V_D is delayed by a mechanical switch. The delay is represented by the gray box.

initial value, under an applied gate bias of $V_G = \pm 40$ V and drain bias of $V_D = \pm 5$ V, is shown in Figure 5.6. In <30 seconds, the currents in both n-channel and p-channel modes of operation decay by over an order of magnitude. We find that these decays occur regardless of whether or not a drain bias is applied to the device, as shown in Figure 5.4. Moreover, the rates of current decay are largely unchanged by the magnitudes of V_G and V_D, as shown in Figure 5.5.

The decay in I_{DS} is well fit by a stretched exponential function (fit to the data in Figure 5.6(a) is shown in black) of the form:

$$I_{stress} = I_0 \cdot exp\left((-t/\tau)^{\beta}\right) \tag{5.2}$$

I_0 is the pre-stress drain-source current and τ and β are the fitting parameters. Stretched exponential functions have been used extensively to characterize bias-stress in various FET systems [93, 133, 134, 135, 136], in which τ is a characteristic time constant and β is a dispersion parameter related to the distribution of time constants

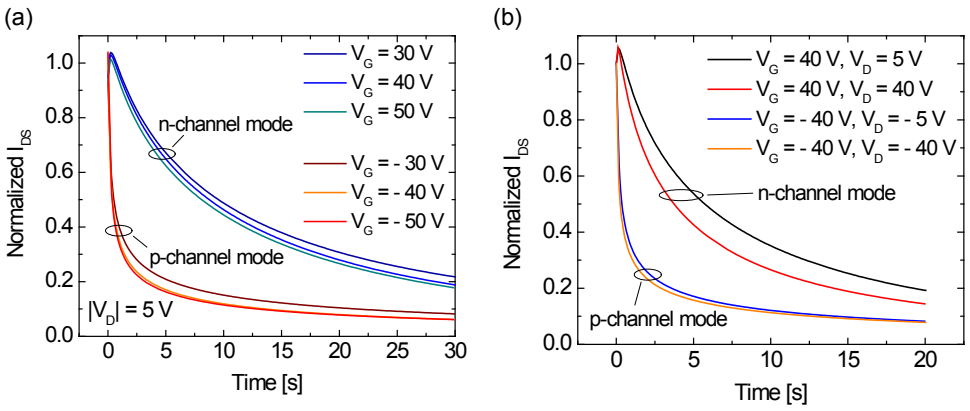

Figure 5.5: (a) Normalized I_{DS} under an applied gate bias as a function of time for different drain biasing conditions.

that characterize the trapping process. The decay in p-channel operation ($\tau = 0.7$ s, $\beta = 0.38$) is observed to occur faster than in n-channel operation ($\tau = 2.6$ s, $\beta = 0.56$). We note that, although the fitting parameter β is similar to that observed in other systems, the time constant τ is faster by several orders of magnitude (τ typically varies from 10^3 - 10^8 s in organic FETs [133]). For example, in pentacene-based FETs, the reported fitting values are $\beta \approx 0.4$ and $\tau \approx 10^4$ s [93]. One explanation for this difference is that trapping in the present QD system is relatively energetically favorable, whereas the long time constants for organic and a-Si:H FETs have been attributed to energy barriers that mediate the rate of trapping [136, 93].

5.3.3 Estimate of the QD Trap Density

The fast evolution of the bias-stress effect may suggest that there are a relatively large number of traps in the present system. To further assess this possibility, we estimate the amount of charge trapped during bias stress according to the equation: $Q_{trapped} = CV_T$ [93, 133]. The value for ΔV_T is calculated from measurements of I_{DS}

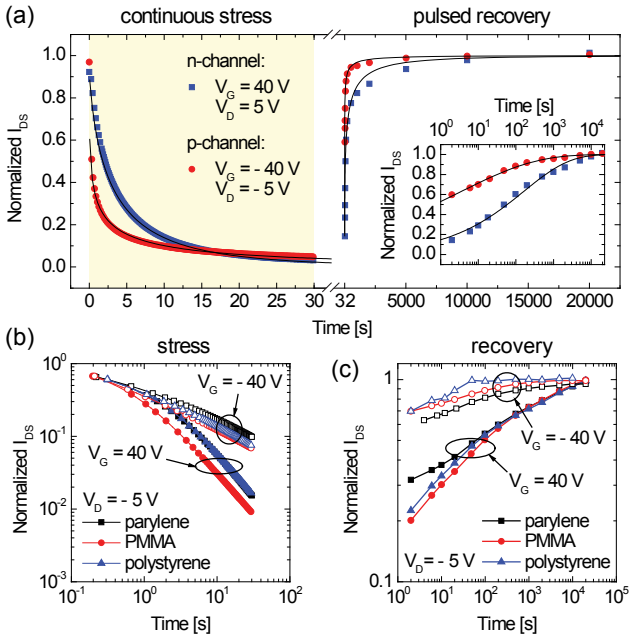

Figure 5.6: (a) Normalized drain-source current under a continuous applied gate bias and recovery with time upon the release of that bias. Black lines are stretched exponential fits to the data. (inset) Semi-logarithmic plot of the recovery of normalized drain-source current following stress. (b-c) Normalized stress and recovery on log-log plots for devices made with different gate dielectrics at a drain bias of -5 V. Lines serve as a guide to the eye.

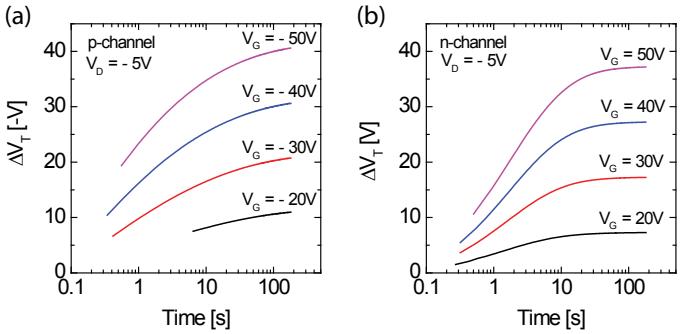

Figure 5.7: (a-b) Transfer characteristics in n-channel and p-channel operation exhibiting a shift in threshold voltage, ΔV_T, following sustained gate bias. (c-d) Calculated shift in threshold voltage with time.

under fixed bias conditions using the following equation [129]:

$$|\Delta V_T| = (1 - \frac{I(t)}{I_0}) \, |V_G - V_{T0}| \tag{5.3}$$

I_0 is the initial drain-source current and V_{T0} is the initial threshold voltage. The resulting plots of ΔV_T versus time, for a device consisting of a PMMA dielectric, are shown in Figure 5.7(a) and Figure 5.7(b) for stress at positive and negative gate biases, respectively. For the range of V_G tested, ΔV_T begins to saturate after several minutes to a value approaching $V_G - V_{T0}$. This corresponds to complete screening of the gate field and a turn-off of the device.

Since we do not observe an upper-bound to ΔV_T, we conclude that the density of trapped charges in both polarities is greater than the density of injected carriers, the magnitude of which is given by $C(V_G - V_{T0})/q$. We can nevertheless estimate a lower-bound for the trap densities in the QD film by considering the amount of charge being trapped for the highest biasing condition tested before the onset of permanent degradation of device performance (V_G = 50 V). ΔV_T was measured to be 24.2 V for n-channel operation and 38.0 V for p-channel operation, corresponding to trap

densities of approximately 8.6×10^{11} carriers-per-cm^2 and 1.4×10^{12} carriers-per-cm^2, respectively. Assuming that all of this charge is trapped in the first QD monolayer adjacent to the dielectric layer and that the QDs are packed in a FCC (111) structure (2-dimensional density can be calculated by $D_{2d} = 1/(2\sqrt{3} \cdot r^2)$ [149], where r is the sum of the QD radius (2.2 nm) and half of the interparticle spacing (0.8 nm) [109]), we estimate a QD density of 3.2×10^{12} QDs-per-cm^2. Thus, the calculated lower bound for trap density is less than 0.5 traps-per-QD.

5.3.4 Recovery from Bias Stress

The recovery of EDT-treated PbS QD FETs following the bias-stress condition is also shown in Figure 5.6. These data are measured by periodically pulsing the gate bias from zero to V_G, and maintaining V_G for only 10 ms to record I_{DS}. Recovery data are found to be well fit by a stretched exponential function of the form:

$$I_{recovery} = I_0 \cdot \left(1 - exp\left((-t/\tau)^{\beta}\right)\right) \tag{5.4}$$

The recovery occurs faster after operation in p-channel mode (τ = 4 s, β = 0.22) as compared to n-channel mode (τ = 163 s, β = 0.36). At the first data point, collected at 2 seconds after the end of the stressing cycle, the hole current recovers to approximately 60% of its initial level. It subsequently approaches its initial value in a rapid, stretched exponential manner. Recovery from stress in n-channel operation, in contrast, is slower, taking several hours to fully return to its initial condition. This indicates that the detrapping of electrons in this system is slower than the detrapping of holes and may imply the presence of deep electron traps and relatively shallow hole traps. As shown in Figure 5.6(b-c), stress and recovery characteristics are similar for

devices made with all three dielectrics. We therefore conclude that the bias-stress effect in this system is a bulk phenomenon and not due to a particular QD/dielectric interface (i.e. the charge accumulation that is responsible for the change in I_{DS} occurs within the QD film itself).

5.3.5 QD FET Operation at Low Temperatures

To investigate the specific bulk mechanisms responsible for the bias-stress effect, transistor characteristics and measurements of the bias-stress effect were taken as a function of temperature (T = 90 K - 295 K). Samples were loaded into a Janis ST-100 optical cryostat and cooled with liquid helium. A cartridge heater controlled by a Lakeshore 330 temperature controller was used to maintain a desired temperature set point. Thirty minutes were allowed in between stress measurements in order to allow the device to recover and for the temperature to stabilize at the next temperature point. Linear transfer characteristics ($V_D = \pm 5$ V) taken as a function of temperature are given in Figure 5.8(a) and 5.8(b) for n-channel and p-channel operation, respectively. In n-channel operation, the extracted conductance follows an Arrhenius temperature dependence and is well fit to the equation:

$$G(T) = G_0 \cdot exp\left(-E_a/k_B T\right) \tag{5.5}$$

G_0 and E_a are fitting parameters. This indicates that the transport mechanism is thermally activated hopping (see inset of Figure 5.8(a)), as has recently been observed in EDT-treated PbSe QD FETs [126]. We extract an activation energy of $E_a = 0.13$ eV. The shapes of the transfer characteristics in p-channel operation are distorted by the faster bias stress effect (see Figure 5.8(b)), preventing the extraction of a

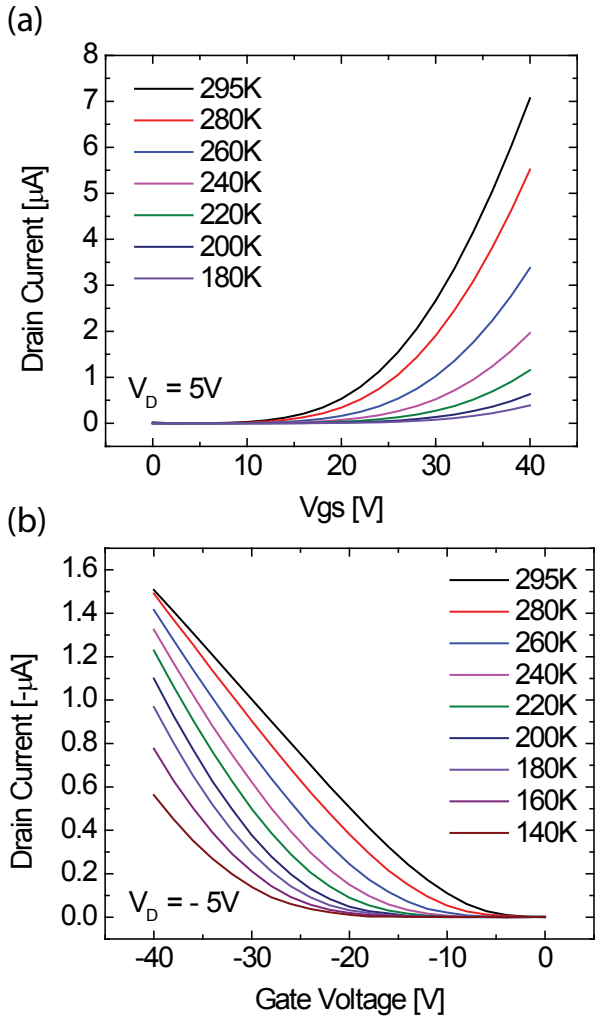

Figure 5.8: (a) Transfer characteristics in n-channel mode as a function of temperature. (inset) Extracted conductance as a function of inverse temperature. (b) Transfer characteristics in p-channel mode as a function of temperature.

meaningful trend in the conductance.

The bias-stress effect is substantially diminished at reduced temperature, particularly in n-channel mode (see Figure 5.9(a-b)). We quantify these observations by extracting the stretched-exponential fitting parameters from the normalized I_{DS} decays at different temperatures, which are shown in Figure 5.9(c-d). The time-constant

of the current decay, τ, is found to follow thermally-activated Arrhenius behaviour of the form:

$$\tau = v^{-1} \cdot exp\,(E_a/k_B T) \tag{5.6}$$

E_a and v^{-1} are fitting parameters. Also, the dispersion parameter, β, is observed to slowly and linearly increase with temperature. Such a temperature dependence has previously been noted in FETs based on several other material systems, including the polymer PTAA [133], ZnO [134] and amorphous silicon (a-Si:H) [135, 136]. Bias stress in these systems was ascribed to the creation of defects or traps within the semiconductor layer or at the semiconductor/dielectric interface; the activation energy can be interpreted as the energy required to create the trapping defects. In the present system, we determine the activation energy in n-channel mode, to be 0.63 eV and the frequency prefactor, v, to be 1.4×10^{10} Hz. These parameters are similar to those reported in organic and a-Si:H systems, where E_a is typically $\approx$ 0.6 eV and v varies from 10^3 Hz to 10^9 Hz [15]. In contrast, the relatively weak temperature sensitivity of the bias stress effect in p-channel mode is described by the fitting parameters E_a = 0.09 eV and v = 57 Hz.

5.3.6 QD FET Operation as a Function of QD Size

To further investigate the bulk mechanisms for bias stress, we prepared and characterized PbS QD FETS as a function of QD size. QD diameters were determined by measuring the position of the first QD excitation peak and relating it to the QD diameter based on the experimental data presented in Ref. [146]. Field-effect mobilities were extracted and are plotted as a function of QD size in Figure 5.10. Note

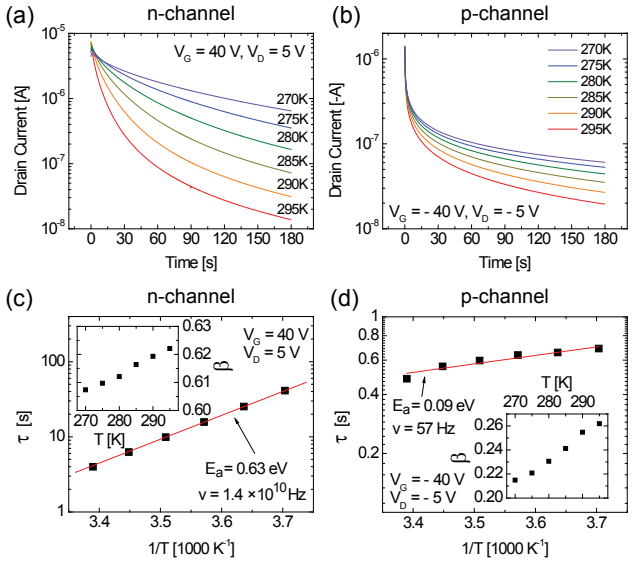

Figure 5.9: (a-b) Drain current in n-channel and p-channel operation, respectively, as a function of time for different temperatures. (c-d) Stretched exponential fitting parameters as a function of inverse temperature. See text for definition of fitting parameters.

that for the two smallest QD sizes, measurements were conducted in the saturation regime ($V_G = V_D = \pm 60$ V) in order to ensure sufficient current to extract mobility. All other measurements were conducted in the linear regime as described above. Electron and hole mobilities are observed to be highly sensitive to QD size for smaller core diameters. In n-channel mode, the field-effect mobility peaks at approximately d =4.5 nm and declines for larger QD sizes. In p-channel mode, the mobility plateaus at approximately the same core diameter and remains constant for larger sizes. This is qualitatively what was observed in the case of PbSe QD FETs in Ref. [124]. As we will show below, however, these measurements are subject to varying degrees of hysteresis as a function of QD size. Mobility measurements for smaller QD sizes are thus likely to underestimate the mobility that would be observed prior to any bias

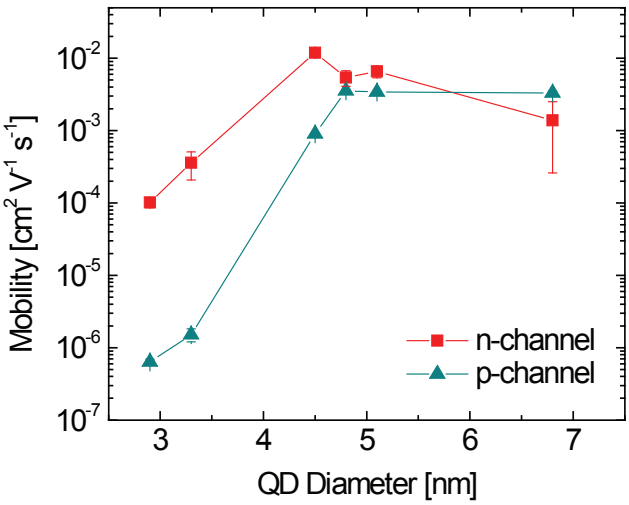

Figure 5.10: Field-effect mobilities measured in n-channel and p-channel modes of operation for a range of QD sizes. Lines serve as a guide to the eye.

stress, particularly in p-channel mode, relative to measurements for the larger QD sizes.

We next study the effect of QD size on the bias stress characteristics. The stress and recovery characteristics for devices made with QDs of 3.7 nm, 4.4 nm and 5.4 nm diameters are shown in Figure 5.11. In n-channel operation, the time constant of I_{DS} decay under bias stress is observed to decrease with QD size from 14.4 s for 5.4 nm QDs to 0.4 s for 3.7 nm QDs ($\beta \approx 0.5$). In p-channel operation, on the other hand, the speed of the decay is observed to be invariant to QD size. These observations may be understood in terms of the relative positions of the trap levels with respect to the conduction and valence bands as a function of QD size. Specifically, several recent reports suggest that the HOMO levels in PbS QDs are relatively isoenergetic with QD size with respect to the LUMO levels. As a result, the activation energy for trapping in p-channel mode may be essentially independent of QD size, thus explaining the

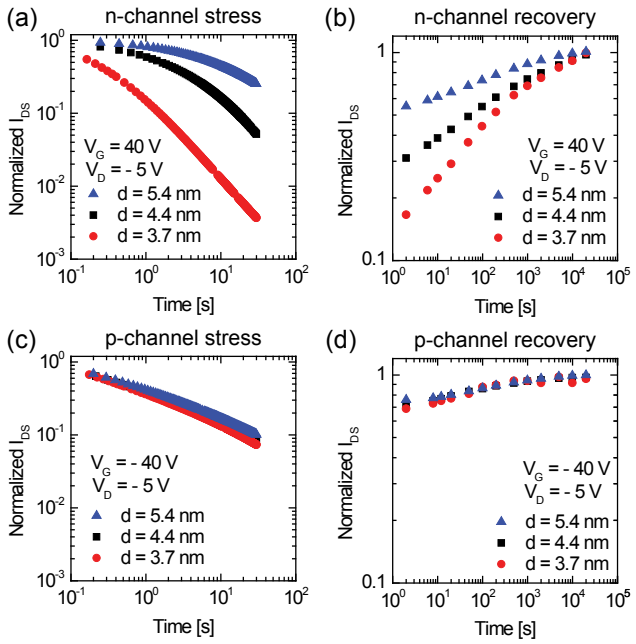

Figure 5.11: Normalized drain-source current stress and recovery in n-channel (a-b) and p-channel (c-d) operation for devices made with PbS QDs of different core diameters.

observed invariance of the bias-stress effect with QD size. An alternative possibility is that the bias stress mechanism in p-channel mode may not directly be associated with the presence of QD surface defects, but instead may be due to trapping on the EDT ligands present within the QD film.

5.4 Possible Trapping Mechanisms

Though our investigation thus far suggests the presence of deep electron traps as well as shallow hole traps that reside within the QD film, the precise physical cause of these traps remains elusive. Electrons traps in PbS QDs have been attributed to unpassivated Pb^{2+} sites [139] as well as to oxide species ($PbSO_3$ and $PbSO_4$)

resulting from the oxidation of surface sulfur anions on the QDs [69]. Rigorous air-free conditions were maintained throughout the synthesis of the QDs as well as the fabrication and testing of the FETs. Nevertheless, we cannot rule out the presence of oxide compounds on the QD surfaces. Exposure of devices to air indeed results in a loss of n-channel operation, which we attribute to the formation of electron-trapping oxidation products on the QD surfaces [150, 83]. As for the source of hole traps, temperature-dependent photoluminescence studies have identified sulfur anions on the PbS QD surface to act as hole traps [140, 139]. Another possibility is that the thiol ligands themselves are responsible for the hole traps, as has been observed in CdSe QD systems [143, 144, 145]. This scenario would also be consistent with the lack of an observable change in the p-channel stressing characteristics as a function of QD size, as the density of available EDT-based hole traps may be expected to remain relatively invariant to QD size.

5.5 Conclusion

We characterized the performance of FETs consisting of 1,2-ethanedithiol (EDT)-treated PbS QD films and studied the strong bias-stress effect observed in these devices. Top-gated devices exhibit ambipolar operation with typical mobilities on the order of $\mu_e = 8 \times 10^{-3}$ cm^{2}V^{-1}s^{-1} and $\mu_h = 1 \times 10^{-3}$ cm^{2}V^{-1}s^{-1}. The particular choice of dielectric was found to have little effect on the evolution of the bias-stress effect, leading us to conclude that the mechanism for bias stress originates in the bulk of the QD film and is not due to a particular semiconductor/dielectric interface. The extent of the bias-stress effect, as well as the very high speed of the stress and

recovery processes that we observe, suggests that a large quantity of trapping states are available within EDT-treated PbS QD films. Measurements as a function of QD size reveal that the stressing process in n-channel operation is faster for QDs of a smaller diameter. These results are consistent with a mechanism in which field-induced morphological changes within the QD film result in screening of the applied gate field. This work elucidates aspects of charge transport in chemically treated lead-chalcogenide QD films and is of relevance to on-going investigations toward employing these films in optoelectronic devices.

Chapter 6

A QD-Sensitized Heterojunction Photoconductor

In the PbS QD photoconductors described in Chapter 4, the exchange of the insulating native ligands on QD surfaces with much shorter passivating ligands was integral to enabling charge transport and efficient photodetector operation. The use of such aggressive chemical treatments, however, comes with the disadvantages of reducing the quality of QD surface passivation and the environmental stability of the QD film. In this chapter, we describe an alternative approach to enable the efficient extraction of photo-generated charge from QDs with the use of a lateral heterojunction photoconductor architecture. In this structure, the functions of charge transport and optical absorption are dissociated into different physical layers, obviating the need for chemical treatment of the QD film.

6.1 Introduction

Organic semiconductors and colloidal nanocrystal quantum dots (QDs) are promising candidate materials for realizing photovoltaics (PVs) and photodetectors (PDs) that can be fabricated near room temperature and that are scalable to large-area substrates. Organic semiconductors, including small molecules and polymers, possess a number of desirable attributes for optical sensing including high absorption coefficients over visible wavelengths and compatibility with large-area deposition processes such as ink-jet and screen printing. Various artificially nanostructured materials have also become available that possess large transition dipole moments and consequently strong optical absorption. Of particular interest among these artificial nanostructures are chemically synthesized QD nanocrystals, which, like organic semiconductors, can be processed from solution and which have a broad optical response that can be tuned from the visible to the infrared by selection of the type and physical size of the nanocrystals. [34, 58].

The unique attributes of QD materials (i.e. size-tunability of absorption and the requirement of surface-passivating ligands for solubillity) suggest the need for new device architectures to fully take advantage their properties. In this chapter, we demonstrate a hybrid organic/QD PD in which the optical absorption and electrical charge transport are physically separated into different layers, enabling their independent tuning and optimization. This desirable capability is rare among organic photodetecting device structures, with the main exception being the dye-sensitized solar cell [151]. Owing to its unique geometry, the present device also provides direct insight into the exciton dissociation mechanism that is crucial to the operation of QD

PDs.

Previously, several organic PV and PD structures incorporating QDs were reported [152, 153, 70, 154, 155, 119, 156, 84]. One class of these structures employs thin films containing QDs that are sandwiched between top and bottom contact electrodes. In the sandwich geometry, current flows vertically between the electrodes after photogenerated excitons dissociate into free carriers at a type-II heterojunction interface between the organic and QD semiconductors. Hybrid organic/QD PVs of this type have been demonstrated both in bulk heterojunction [152, 153] and bilayered heterojunction [70] configurations. A second class of photosensitive structures employs thin films of organic semiconductors [154, 155, 119] or QDs [156, 84] that are contacted by lateral in-plane electrodes. To generate current flow in the lateral geometry, voltage is applied across the electrodes facilitating extraction of the photogenerated charge.

In this chapter, we describe a bilayered lateral heterojunction photoconductor that is comprised of a molecular thin film of N,N'-Bis(3-methylphenyl)-N,N'-bis(phenyl)-9,9-spirobifluorene (spiro-TPD) and a thin film of trioctylphosphine (TOPO)-capped CdSe colloidal QDs. The device structure is shown in Figure 6.1. The selection of spiro-TPD was based on its morphological stability [40] and its favorable energy band alignment with CdSe QDs [70]. The hole mobility of 10^{-4} cm^2 V^{-1} s^{-1} in spiro-TPD is several orders of magnitude higher than the electron mobility in the film of TOPO-capped CdSe QDs [155, 157]. Therefore, in the lateral heterojunction geometry the organic layer predominantly serves as the charge transport layer. Also, because spiro-TPD does not absorb across much of the visible spectrum, it is the absorption of the

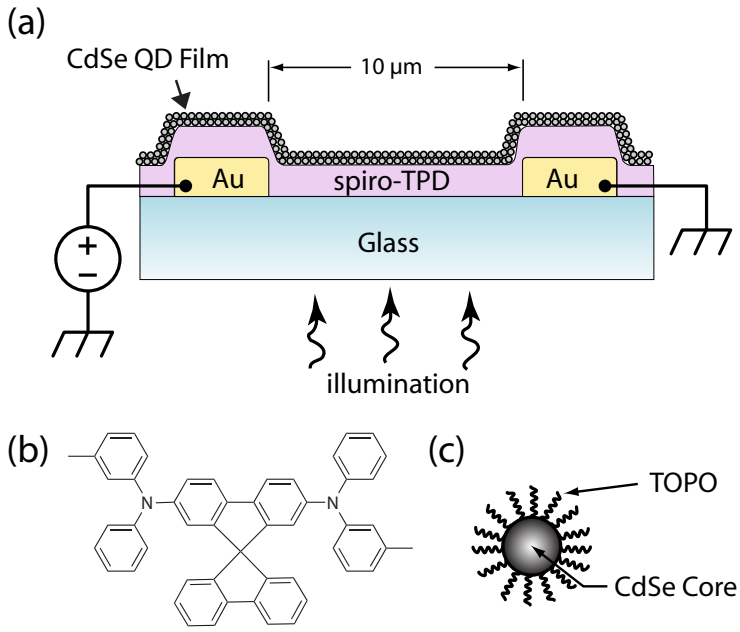

Figure 6.1: (a) Section view of the device structure. The thickness of the spiro-TPD layer is 200 nm. The Au layer is 50 nm thick on top of a 20 nm thick chrome adhesion layer (not shown). For each device there are 30 pairs of Au electrodes arranged in an interdigitated array forming a serpentine channel (not shown). The channel length is 10 μm and the electrode width is 1000 μm. (b) Chemical structure of the hole-transporting material, spiro-TPD. (c) Schematic of CdSe nanocrystal passivated with TOPO ligands.

QD layer that determines the long wavelength edge to the spectral sensitivity of the device.

Under illumination, excitons are generated in the organic and QD layers, which together form a type-II heterojunction (see inset of Figure 6.3). Excitons within a diffusion length of this interface may be dissociated, resulting in the transfer of free electrons to the QDs and holes to the organic charge transport layer. The increase in carrier concentration results in an increase in current when a bias is applied across the electrodes.

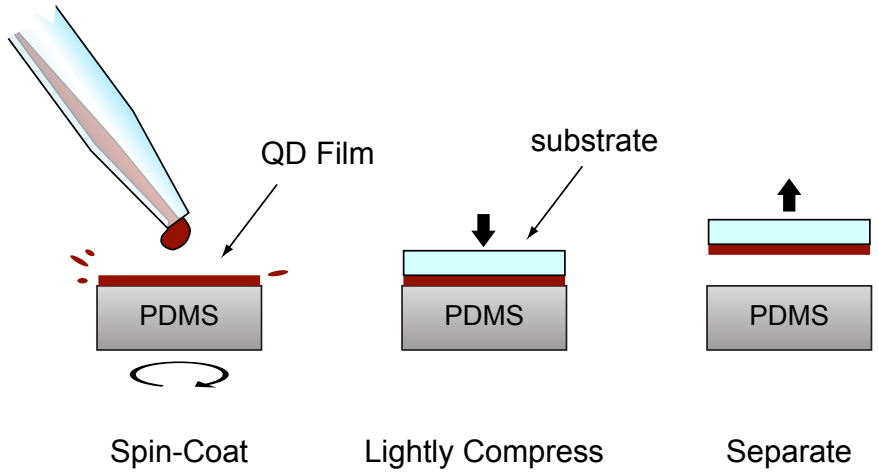

Figure 6.2: Cartoon describing the microcontact printing process used to deposit a thin film of CdSe QDs onto a thermally evaporated film of spiro-TPD.

6.2 Device Fabrication

To form the lateral photodetector structures, interdigitated chrome/gold electrodes (of 20 nm / 50 nm film thickness, respectively) forming a serpentine channel with a length of 10 μm are first deposited by thermal evaporation onto a substrate of D263 borosilicate glass (refractive index of 1.52). A 200 nm thick spiro-TPD film (thickness measured by stylus profilometry) is then thermally evaporated over the electrodes. Subsequently, the samples are transferred directly into a nitrogen-filled glove box without exposure to air.

CdSe QD cores with a lowest energy absorption peak at wavelength $\lambda = 590$ nm are synthesized and passivated by TOPO ligands to provide solubility in chloroform [84]. Microcontact printing from a polydimethylsiloxane (PDMS) stamp is used to deposit the QDs onto the device [70, 158, 159]. Stamps are cleaned with chloroform prior

to spin-coating with QDs at 4000 rotations per minute for 60 s. The stamps coated with QDs are then placed in a vacuum environment ($\approx 10^{-3}$ Torr) for approximately 1 hr to evaporate the solvent, after which a small amount of force is applied between the PDMS stamp and the device substrate to transfer the QD film (see Figure 6.2). The thicknesses of transferred QD films were measured with a Digital Instruments Dimension 3000 Scanning Probe Microscope to be approximately 50 nm. Completed devices were tested immediately after fabrication at room temperature in a nitrogen environment.

6.3 Device Characterization

6.3.1 Current-Voltage Characteristics

Current-voltage characteristics were measured with a Keithley 6487 Picoammeter both in the dark and under illumination by a Lamina green light emitting diode (LED) light engine (emission centered at $\lambda = 521$ nm) at 78 mW cm^{-2}. I-V measurements are shown in Figure 6.3 for a control device, consisting only of the spiro-TPD film, and for a QD Device with both heterojunction layers. We note that since spiro-TPD absorption is minimal at wavelengths greater than $\lambda = 400$ nm, visible light is primarily absorbed by the QDs (see Figure 6.4). If we approximate the electric field distribution across the device as being constant, a bias of 100 V translates to the electric field strength of 10^5 V cm^{-1}. At this bias, the ratio of the light current to the dark current increases from 1.1, measured for the control device, to 3.5 for the QD device.

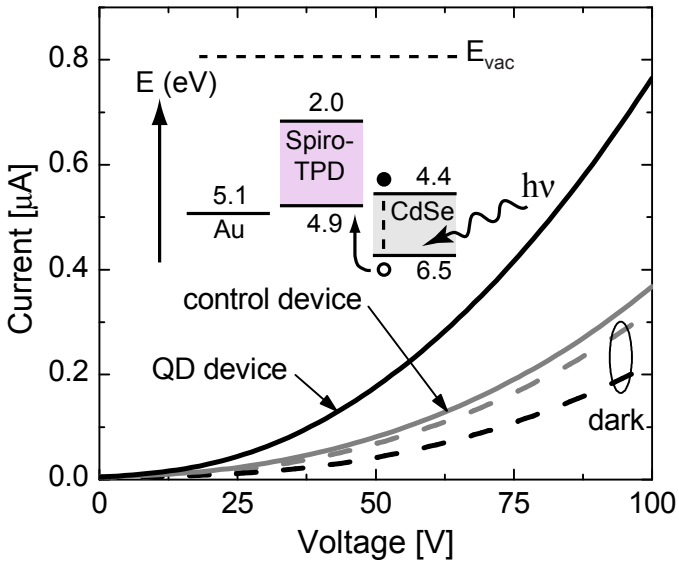

Figure 6.3: Current-voltage characteristics measured for a control device and a QD device. Dashed lines show dark currents. Solid lines show the device response under illumination from a green LED with an intensity of 78 mW cm^{-2} and with emission centered at $\lambda = 521$ nm. The inset shows the energy band diagram for the QD device. The energy levels for the spiro-TPD were taken from Ref. [40]. Energy levels for the CdSe QDs were calculated following the approach reviewed in Ref. [41] and using bulk CdSe parameters obtained from Ref. [42].

We note that unencapsulated devices suffered little degradation after being stored in a nitrogen environment for over 2 months. After approximately 1 week of exposure to ambient conditions, however, we observed an increase in the dark current (bias of 100 V) of greater than an order of magnitude as well as a reduction in the ratio of the light current to the dark current from 4.3 to 1.8 under identical illumination conditions.

6.3.2 Spectrally-Resolved Quantum Efficiency

Device performance can be better understood by considering the monochromatic photon-to-electron conversion efficiency or external quantum efficiency (EQE) as a

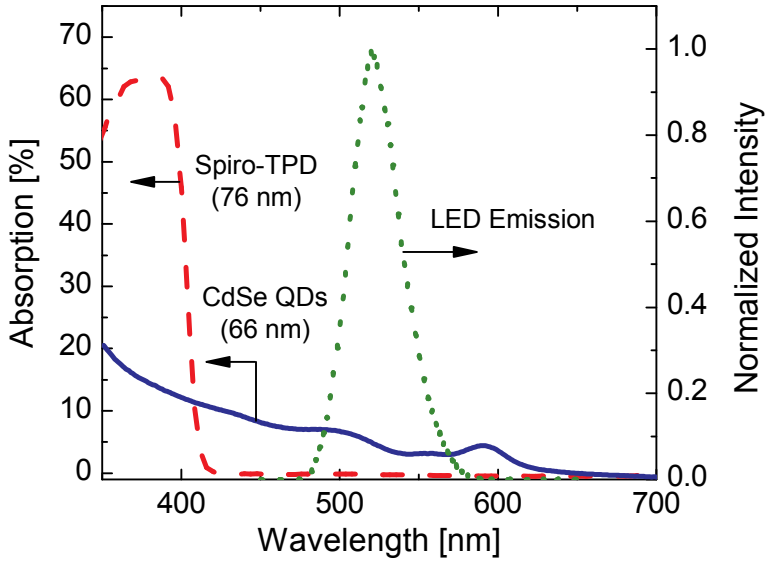

Figure 6.4: Absorption spectra of spiro-TPD (dashed line) and CdSe QDs (solid line) measured with an Aquila NKD-8000 spectrophotometer. Emission from the LED (dotted line) is absorbed exclusively by the QD film.

function of wavelength. For this measurement, the broadband light from a 1000 W Xe lamp was optically chopped and focused into an Acton Spectrapro 300i monochromator. A calibrated silicon PD was used to measure the optical power of the output, which was subsequently focused onto the device under study. A lock-in amplifier provided with the reference signal from the optical chopper (45 Hz) was used to extract a measurement of the AC photocurrent.

Figure 6.5 shows the EQE of the QD device for a variety of biases. A large response peak that occurs between $\lambda = 300$ nm and $\lambda = 400$ nm is attributable to light that is absorbed in the spiro-TPD layer. There is also a strong photoresponse for $\lambda >$400 nm that closely follows the absorption spectrum of the QDs. A maximum in the EQE occurs at $\lambda = 590$ nm, the lowest energy absorption peak of the QDs, which reaches 13% at 300 V. The EQE is related to the internal quantum efficiency (IQE) by the

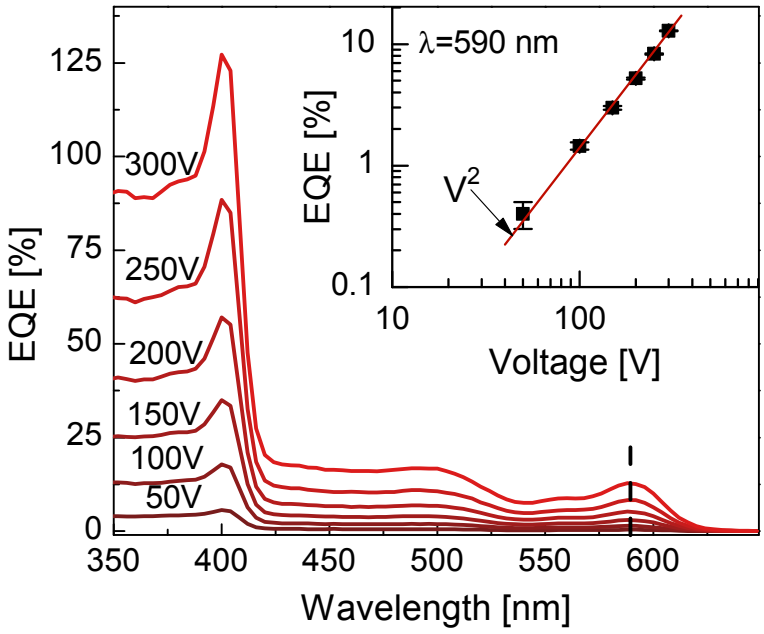

Figure 6.5: EQE spectra for a variety of biases. Inset shows EQE at $\lambda = 590$ nm as a function of bias. Responsivity at 400 and 590 nm are 0.41 and 0.061 A/W, respectively. Photocurrent follows a nearly V^2 power law indicative of space charge limited conduction in spiro-TPD.

absorption efficiency of the device 1-T-R, where T and R are the percentages of light that are transmitted and reflected under illumination, respectively. This relationship can be written as

$$EQE = (1 - T - R) \times IQE \tag{6.1}$$

At $\lambda = 590$ nm, 1-T-R was measured using an Aquila NKD-8000 spectrophotometer to be 16% resulting in an IQE of approximately 80%.

For a sufficiently high bias applied across the electrodes an EQE of greater than 100% may be realized, which suggests that the device is operating in a regime of photoconductive gain. The inset reveals that the EQE measured at $\lambda = 590$ nm follows a V^2 power law dependence with bias. This is consistent with space charge limited conduction in the ideal case of a trap-free low-mobility semiconductor, first described by Rose [160] and Lampert [161], and often utilized in the analysis of charge transport in organic thin films.

6.3.3 Antibatic Photoresponse

We note that there is a strong peak in the photoresponse at $\lambda = 400$ nm, which is also where the spiro-TPD absorption begins to fall off (see Figure 6.4). A photoresponse that is strongest at wavelengths for which absorption is weakest is described as "antibatic". In sandwich devices, this behavior is a consequence of greater charge generation efficiency near the rear interface (the interface farthest from the source of illumination) than within the bulk. The effect is strongest if the active layer is sufficiently thick to absorb most of the incoming light [162, 163]. Since the spiro-TPD

film is optically thick[1], the presence of an antibatic peak at $\lambda = 400$ nm indicates that the spiro-TPD/QD interface is likely the primary site of exciton dissociation.

6.4 Conclusion

This study demonstrates an efficient lateral photodetector that utilizes an evaporated film of an organic material as a charge transport layer and that is sensitized by the optical response of CdSe QDs. A Type-II heterojunction at the organic/QD layer interface facilitates the dissociation of excitons and results in a large photoresponse. An antibatic peak is observed in the EQE spectrum, which suggests that exciton dissociation in the device is dominated by charge transfer at the heterointerface. Since charge generation is largely isolated to the organic/QD interface, this device structure enables the direct study of charge separation at that interface. This is in contrast to devices of the sandwich geometry, in which interfaces between active layer materials and the electrodes may complicate the interpretation of device performance.

[1]The spiro-TPD film thickness is 3.2 times greater than $1/\alpha$, where α is the absorption coefficient measured to be 1.6×10^5 cm^{-1} at $\lambda = 375$ nm.

Chapter 7

NIR Photodiode Sensitized with a J-Aggregating Cyanine Dye

Previous chapters have concerned different photodetecting structures that incorporate colloidal QDs. As noted in Chapter 1, however, there are a variety of organic semiconductors that are also very attractive for infrared photodetection. In this chapter, we describe the characterization of a NIR photodiode that is sensitized by an ultra-thin film of J-aggregating cyanine dye. In contrast to the photoconductors described in previous chapters, the present device may be operated at zero bias and with a relatively fast response speed.

7.1 Introduction

Photodetectors consisting of organic semiconductors, including solution-processed [164, 18] and thermally-sublimed molecular materials[55] have attracted tremendous

research interest due to their potential for low-cost processing as well as their compatibility with inexpensive and arbitrary substrates [45, 94, 165]. To date, efforts to improve the efficiency of such devices have primarily focused on the exploration of new molecular materials with desirable electronic and optical properties [21, 19], as well as on more sophisticated device structures. An additional approach toward improving the performance of organic photodiodes is to engineer the organic semiconductors at the supramolecular level [166], which entails controlling the molecular arrangement of organic materials to realize desirable optical and electronic properties distinct from the molecular constituents. The formation of J-aggregates from cyanine dyes enables quantum mechanical manipulation of energy level splitting, resulting in a range of interesting properties for optoelectronic devices [79]. For example, a red shift and narrowing of the absorption feature accompanies the aggregation of cyanine dye monomers into a J-aggregate crystal structure. Additionally, the peak absorption coefficients of J-aggregate thin films may be considerably higher than non-J-aggregating organic semiconductors, with values for α exceeding 10^6 cm^{-1} [167, 32].

Several photovoltaic devices that incorporate J-aggregating cyanine dyes have been demonstrated, including dye-sensitized solar cells (DSSC) [168, 169, 170, 171] and solid-state solar cells with active layers consisting entirely of thin films of organic materials [172, 173, 174, 175, 16]. The narrow and intense absorption features of J-aggregates, however, are especially desirable in photodetector applications where wavelength specificity may be important. Moreover, the variety of available J-aggregate materials can enable photodetectors to be engineered to operate specifically at desired wavelengths [176]. Of particular interest in this regard is to realize

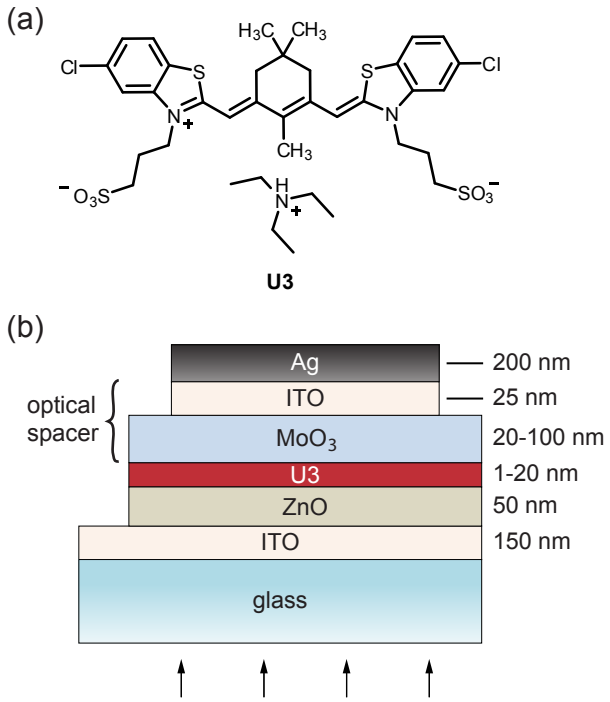

Figure 7.1: (a) Molecular structure of **U3**. (b) Device structure with direction of illumination indicated with arrows.

detectors that operate at near-infrared wavelengths, which would enable a variety of applications including night-vision imaging and biochemical sensing applications [57].

Special consideration is warranted in the design of photodetectors that incorporate J-aggregate films rather than more conventional organic materials. Due to their high optical absorption coefficients, very thin active layer films (<10 nm) may be used to absorb nearly all incident light. Also, in order to take advantage of the narrowness of J-aggregate absorption, device structures with transport layers that are transparent at wavelengths outside of the J-aggregate peak are desirable. Finally, directionality in the ordering and packing of J-aggregate films may result in highly anisotropic exciton diffusion [177, 100], which can have significant implications on the efficiency of donor-acceptor heterojunction devices.

In this chapter, we demonstrate a photodetector that employs metal-oxide charge transport layers and that is sensitized at near-infrared wavelengths by a thin film of the J-aggregating cyanine dye, **U3**. The J-aggregate of **U3** exhibits an absorption peak at $\lambda = 790$ nm and possesses excellent photostability relative to other J-aggregating cyanine dyes [178]. The molecular structure of **U3** is shown in Figure 7.1(a). The structure of our **U3** photodetector is shown in Figure 7.1(b). ITO acts as both a top and bottom contact, while ZnO and MoO_3 act as electron and hole transport layers, respectively. The MoO_3 layer also serves to pin the Fermi level of the top contact to facilitate the extraction of holes from the **U3** layer [43]. Together, the MoO_3 and top-ITO layers also constitute a transparent optical spacer between the **U3** layer and the silver mirror, the thickness of which can be used to optimize the optical field distribution within the device. An external quantum efficiency (EQE) of $16.1 \pm 0.1\%$ (and IQE $= 25.8 \pm 0.1\%$) at $\lambda = 756$ nm is achieved at zero-bias in a device consisting of an 8.1 ± 0.3 nm-thick dye film. The specific detectivity (D^*) and response speed (f_{3dB}) of the fully optimized device are measured to be $(4.3 \pm 0.1) \times 10^{11}$ cm $Hz^{1/2}$ W^{-1} and 91.5 kHz, respectively. Modeling of our structure reveals that photocurrent is limited by the diffusion of photo-generated excitons to the ZnO/**U3** hetero-interface and we determine the exciton diffusion length in the **U3** film to be $L_d = 2.0 \pm 0.4$ nm.

7.2 Determination of U3 Energy Levels

Electrochemical measurements on solutions of **U3** dissolved in either ultrapure water (monomeric **U3**) or in 0.01M aqueous NaCl (J-aggregated **U3**) were made

with an Autolab PGSTAT 20 potentiostat (EcoChemie) using a quasi-internal Ag wire reference electrode (BioAnalytical Systems) submersed in 0.1M aqueous NaCl. Cyclic voltammograms were recorded using a platinum button electrode as the working electrode and a platinum coil counter electrode. The ferrocene/ferrocenium (Fc/Fc+) redox couple in dichloromethane was used as an external reference. A quasi-reversible oxidation peak and an irreversible reduction peak are observed (see Figure 7.2(a)). The half potential of the first oxidation peak is measured to be 1.04 V vs. Ag/AgCl, or equivalenly 0.64 V vs. Fc/Fc+ (the ferrocene redox couple occurs at 400 mV vs. Ag/AgCl). To convert this oxidation potential to the vacuum highest occupied molecular orbital (HOMO) level, we employ the linear relationship between oxidation levels established by cyclic voltammetry and HOMO levels obtained from ultraviolet photoemission spectroscopy that was established in [179]. We arrive at a HOMO level of 5.5 ± 0.1 eV. In order to determine the lowest occupied molecular orbital (LUMO), we first use the empirical relation described in [180] to relate optical bandgap ($\lambda = 790$ nm) to the transport bandgap (E_t) of **U3**. We then add E_t to the HOMO level. E_t is calculated to be 1.7 ± 0.6 eV and the LUMO level is calculated to be 3.8 ± 0.7 eV.

The frontier energy levels for the **U3** film were determined by cyclic-voltammetry and suggest the formation of a type-II heterointerface between the ZnO and **U3** layers, suitable for the transfer of photo-generated charge. A cyclic-voltammogram and the band diagram of the **U3** photodetector structure are shown in Figure 7.2.

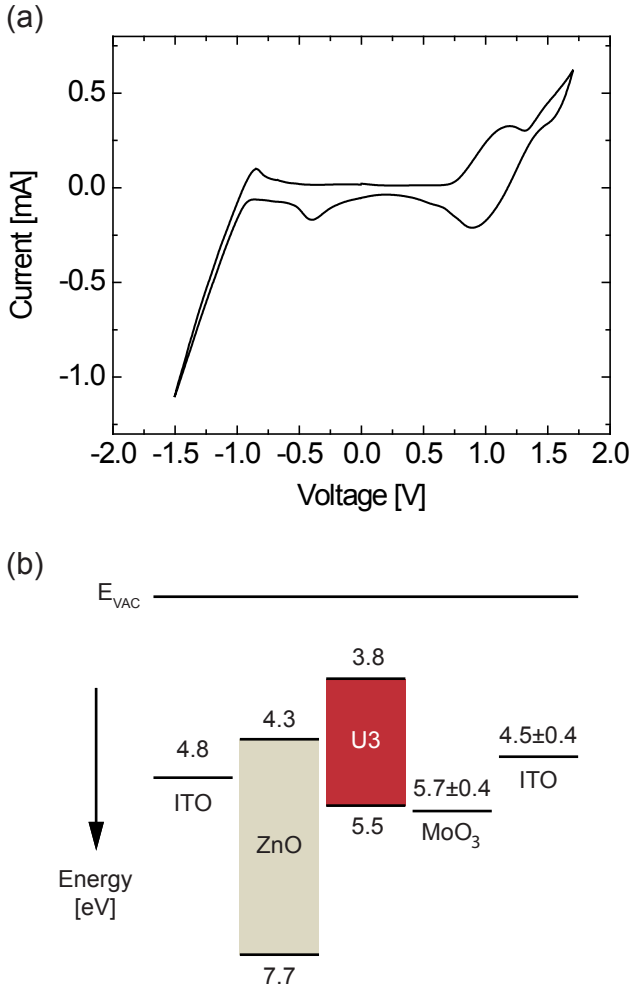

Figure 7.2: (a) Cyclic Voltammogram of J-aggregated **U3** in 0.01 M aq. NaCl, measured with a platinum button electrode and a Ag/AgCl reference electrode at a scan rate of 100 mV/s under ambient conditions. (b) Energy band diagram of the device structure. HOMO and LUMO levels for U3 were determined by cyclic-voltammetry. The remaining energy levels were taken from ref. [43].

7.3 Device Fabrication and Testing

To fabricate the **U3** photodiode structures, pre-patterned ITO substrates (obtained from Thin Film Devices, Inc.) were first cleaned and treated in oxygen plasma. ZnO was deposited at a rate of 0.05 nm/s by RF-sputtering at a power of 150 W and in an Argon atmosphere of 20 mTorr. Films of **U3** (purchased from Ryan Scientific and used without any further purification; CAS Number 202135-09-9) were prepared by dissolving **U3** powder in ultrapure water and spin-casting at 4000 RPM for 60 seconds onto the ZnO layer, which was pre-treated in oxygen plasma. The thickness of the **U3** film is varied from 1 nm to 15 nm by varying the concentration of the **U3** solution from 2 mg mL^{-1} to 10 mg mL^{-1}. Excess material was swabbed away from the edges of the substrate in order to ensure good electrical contact to the ITO electrodes. Film thickness was determined by ellipsometry measurements on separate films prepared on silicon substrates. All of the subsequent processing and testing steps were conducted under rigorously air-free conditions. The MoO_3 hole transporting layer was thermally sublimed at a rate of ≈ 0.1 nm s^{-1} and at a base pressure of 1×10^{-6} Torr. The 25 nm ITO top-contact was deposited via RF-sputtering at a rate of 0.005 nm s^{-1} and in an Argon atmosphere of 5 mTorr. A low sputtering power of 7 W was used in order to minimize damage to the MoO_3 and organic layers, as described elsewhere [181, 43]. Finally, a silver mirror (200 nm thickness) was sputtered on top of the ITO at a rate of 0.05 nm s^{-1} to complete the device. The combined thickness of the MoO_3 and ITO layers can be chosen such that the **U3** layer would be situated at the anti-node of the optical electric field, thus maximizing absorption of the incident light [182]. The device area, as defined by the anode-cathode overlap, is 1.21

Table 7.1: Parameters extracted from fits to the ideal diode equation for devices consisting of **U3** films of different thicknesses.

U3 Thickness [nm]	R_p [Ω cm^2]	R_s [Ω cm^2]	J_s [A cm^{-2}]	n
15.0	3793900	28	1.4×10^{-7}	2.9
10.5	607650	11	1.1×10^{-7}	2.4
8.1	35083	5	1.5×10^{-6}	2.8
4.0	41940	17	7.7×10^{-7}	3.0
1.0	338	3	2.7×10^{-7}	1.2

mm^2. Current density-voltage (J-V) measurements were recorded by a Keithley 6487 picoammeter both in the dark and under illumination, for which a Newport LPM-785 laser diode directed through a beam expander was used. The illumination intensity at $\lambda = 785$ nm was 1.7 mW cm^{-2}. For external quantum efficiency measurements, the sample was illuminated with optically-chopped light from a monochromator that underfilled the device area, and the AC photocurrent was measured with a SRS-830 lock-in amplifier.

7.3.1 U3 Photodetector Current-Voltage Measurements

A representative J-V curve for a device consisting of a 10.5 nm-thick **U3** film and a 60 nm-thick MoO3 film is shown in Figure 7.3(a). In forward bias, the J-V curve in the dark is well-fit to the generalized Shockley equation [183], given below:

$$J = \frac{R_p}{R_s + R_p}\left(J_s\left[exp\left(\frac{e(V - JR_s)}{nk_BT}\right) - 1\right] + \frac{V}{R_p}\right) \tag{7.1}$$

J_s is the reverse-bias saturation current, n is the diode ideality factor, and R_s and R_p are the series and shunt resistances of the diode. The extracted ideality factor is 2.4 ± 0.1, indicating that carrier recombination within the device is a significant

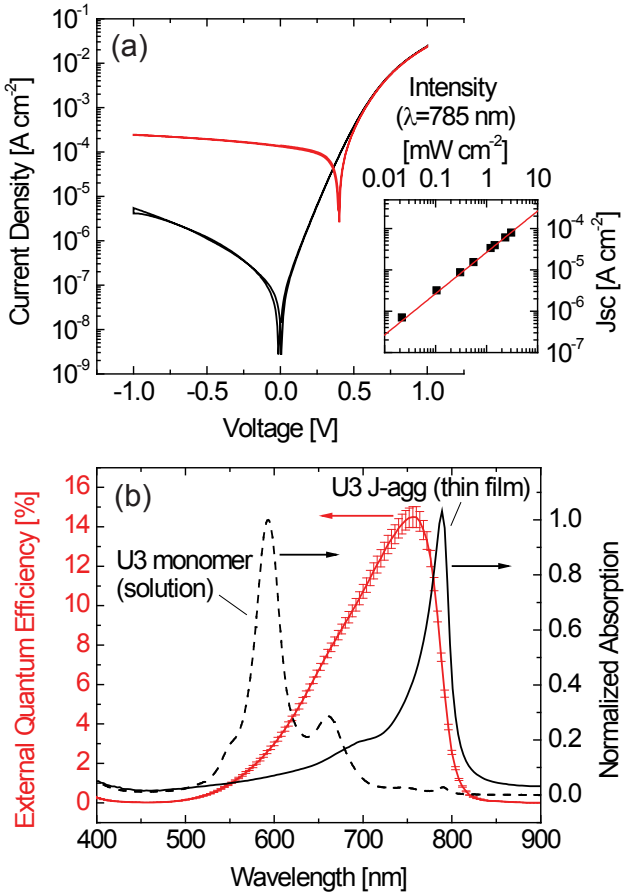

Figure 7.3: (a) Current-voltage characteristic of a typical device in the dark and under illumination of 1.7 mW cm^{-2} at $\lambda = 785$ nm. **U3** thickness is 10.5 nm and the MoO_3 thickness is 60 nm. (inset) J_{SC} as a function of illumination intensity. A linear fit to the data is shown in red. (b) External quantum efficiency of the same device as in (a), shown in red. Also shown are the absorption spectra of monomeric **U3** (dotted line), measured in a 3.3 μg mL^{-1} solution of ultrapure water, and J-aggregated **U3** (black line), measured in a thin film spun-cast at a concentration of 8 mg mL^{-1}.

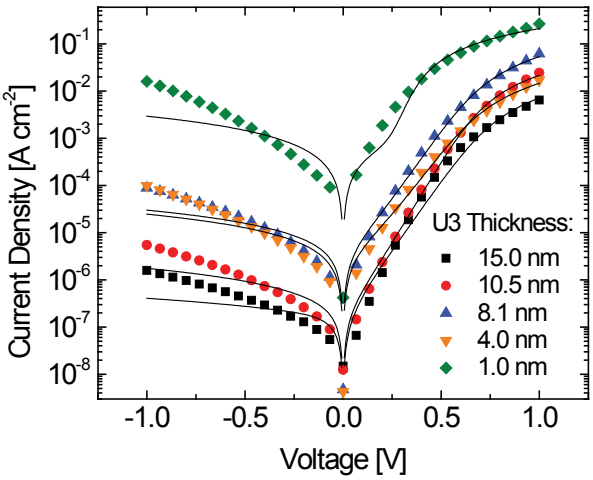

Figure 7.4: J-V characteristics for devices consisting of **U3** films of different thicknesses. The MoO_3 thickness is 60 nm. Fits to the ideal diode equation are shown in black.

contribution to the dark current. J-V characteristics under dark conditions for devices with different thicknesses of **U3** are shown in Figure 7.4. Fits for these data are provided in Table 7.3.1.

The differential resistance (R_D), which is defined as the slope of the J-V curve about zero-bias, is measured to be 170 kΩ cm^2. A high differential resistance is desirable, as it results in lower electrical noise and, consequently, a higher signal-to-noise ratio for a given value of responsivity, as will be discussed later. Under illumination at 785 nm, we measure an open-circuit voltage (V_{OC}) of 0.4 V, a short-circuit current density (J_{SC}) of 1.12×10^{-4} A cm^{-2} and a fill factor of 0.43, making the device suitable for operation as a photodetector without an applied bias. The magnitude of J_{SC} is found to follow a linear relationship with illumination intensity (see inset), which is also desirable in photodetector applications.

These performance characteristics are found to be highly sensitive to the thickness

of the **U3** film. For example, R_D varies with the thickness of the **U3** film from 5.8 ± 1 kΩ cm^2 for devices consisting of a 1 nm **U3** film to 790 ± 160 kΩ cm^2 for devices consisting of a 15 nm-thick **U3** film. Moreover, devices with a **U3** film thickness of <8.1 nm suffer a large reduction in V_{OC} (see inset of Figure 7.5(a)). These observations indicate that the presence of a high-quality **U3** film is integral in this structure to realize high rectification as well as a photovoltaic response, both of which are critical to photodetector performance.

7.3.2 External Quantum Efficiency

To characterize the photosensitivity of the device, we conducted spectrally-resolved measurements of external quantum efficiency (shown in Figure 7.3(b)). Broadening of the **U3** EQE peak relative to the J-aggregated **U3** absorption spectrum is attributed to enhanced off-peak absorption due to the optical half-cavity present in the structure. This broadening results in a blue-shift in the peak EQE from $\lambda = 790$ nm to $\lambda = 756$ nm. The magnitude of the peak EQE is found to be highly sensitive to the thicknesses of both the MoO_3 optical spacer layer and the **U3** film (see Figure 7.3(a-b)). A maximum EQE of $16.1 \pm 0.1\%$ is obtained in a device consisting of a 60 nm MoO_3 film and a **U3** thickness of 8.1 ± 0.3 nm. The peak in EQE magnitude is observed to trail off for increasing thickness of **U3** and MoO_3 due to optical interference effects. The downward trend in EQE for thinner **U3** film thicknesses (Figure 7.5(a)) can be attributed to the reduction in film quality and the associated reduction photovoltaic performance, as shown in the inset of Figure 7.5(a).

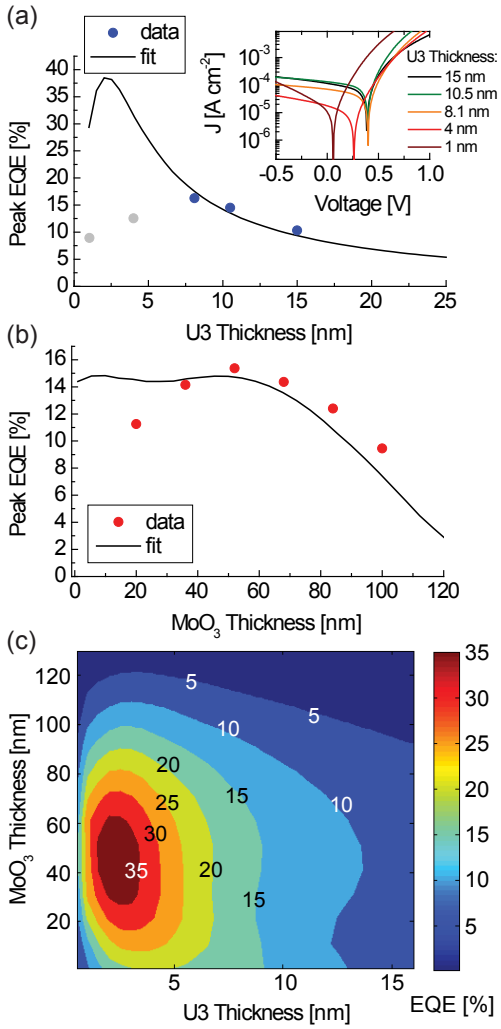

Figure 7.5: (a) EQE as a function of **U3** layer thickness with the MoO_3 thickness fixed at 60 nm. Black line is a fit to the EQE based on the model described in the text with **U3** exciton diffusion length, $L_D = 2.0 \pm 0.4$ nm. Grey circles indicate that the obtained EQE is influenced by a loss of photovoltaic performance in the device, and are not due to optical interference effects (see inset). (inset) J-V characteristics for devices with different **U3** thicknesses under illumination of 1.7 mW cm^{-2} at $\lambda = 785$ nm. (b) EQE as a function of MoO_3 spacer layer thickness with **U3** thickness fixed at 8.1 nm. Black line is a fit with $L_D = 2.0 \pm 0.4$ nm. (c) Contour plot showing EQE as a function of the **U3** and MoO_3 layer thicknesses predicted by the model described in the text.

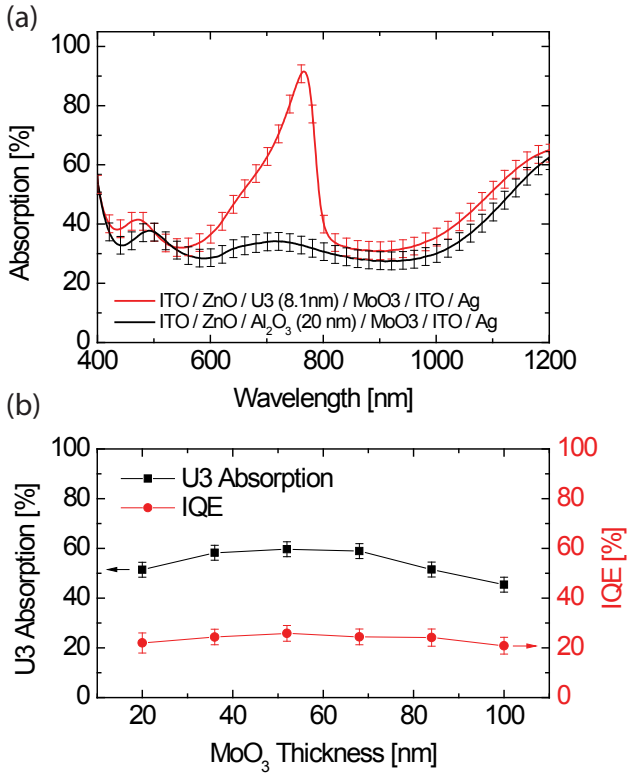

Figure 7.6: (a) Absorption calculated from 1-R in structures consisting of spun-cast **U3** and sputter-deposited Al_2O_3 (reference) films. (b) Absorption and internal quantum efficiency in structures consisting of **U3** films for different MoO_3 thicknesses.

7.3.3 Internal Quantum Efficiency

The peak internal quantum efficiency (IQE) is calculated by dividing the EQE measured in completed photodetector devices by the fraction of light absorbed in the **U3** film. The latter is determined from measurements of optical reflection in test structures identical to the device structure shown in Figure 7.5(a) and in structures in which the **U3** film was replaced by a transparent film of sputter-deposited Al_2O_3. The thickness of the Al_2O_3 layer was selected to approximately match its optical path length with that of the **U3** film near the **U3** absorption peak (λ = 790 nm). This ensures that, apart from its lack of optical absorption, the Al_2O_3 layer will mimic the

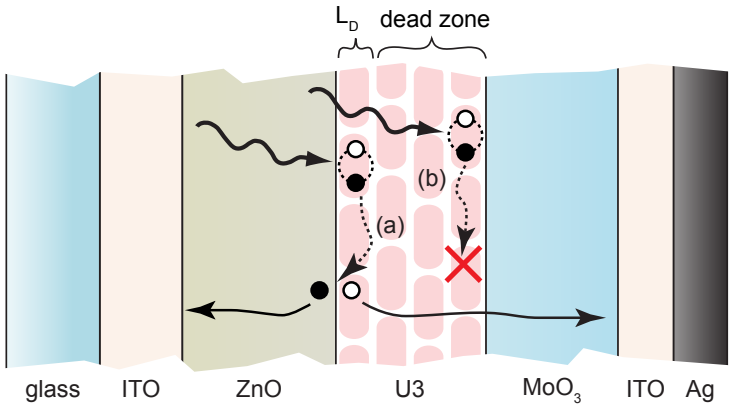

Figure 7.7: Schematic describing the photocurrent generation process in the **U3** photodetector structure. (a) Excitons generated within L_D from the ZnO interface are able to dissociate into free carriers that can be extracted from the device. (b) Excitons generated further than L_D from the ZnO interface recombine (indicated by the red 'X') and do not contribute to photocurrent.

presence of the **U3** film so that non-active layers will be subjected to nearly identical optical fields in both structures. By taking the difference between the magnitudes of the optical absorption in these structures, the fraction of light absorbed within the **U3** film can be determined. The absorption within the **U3** film and the IQE are shown for devices with varying MoO_3 thickness in Figure 7.6. The peak in IQE of $25.8 \pm 3\%$ suggests that there is a substantial loss of photocurrent in the device. This loss is attributed to the generation of excitons too far from the particularly narrow photoactive region of the **U3** film (further than L_D from the ZnO/**U3** interface). Such photo-generated excitons will recombine rather than contribute to photocurrent. This loss mechanism would imply that the exciton diffusion length in the direction normal to the **U3** film is very low, since the total **U3** film thickness is only 8.1 ± 0.3 nm. This situation is depicted in Figure 7.7.

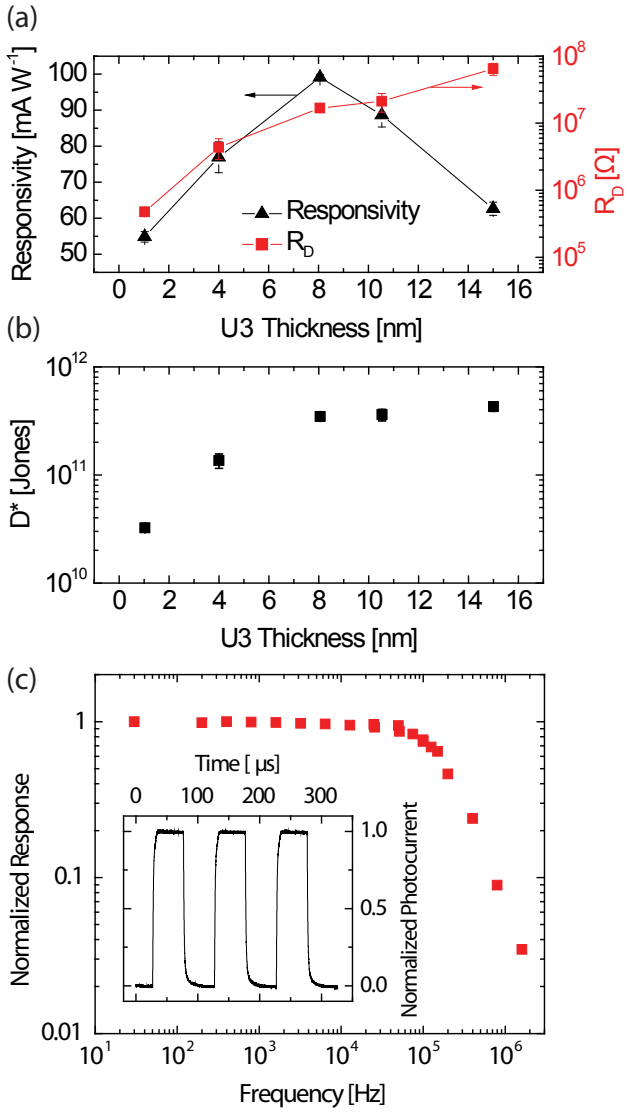

Figure 7.8: (a) Peak responsivity and differential resistance, R_D, as a function of **U3** layer thickness. (b) Specific detectivity as a function of **U3** layer thickness. (c) Bode plot showing roll-off of device performance. (inset) response of device at 10 kHz.

7.3.4 Specific Detectivity

To characterize the performance of this structure for photodetector applications, we calculate the specific detectivity (D*), which is measured in units of cm $Hz^{1/2}$ W^{-1} or "Jones." D* is a metric that describes the signal-to-noise ratio of a photodetector

and that is normalized to the detector area. It can be calculated using the equation, $D^* = (\sqrt{(A_D \Delta f)}/I_n)R$ [60] where A_D is the active area of the device, I_n is the noise current, Δf is the bandwidth over which the noise current is measured, and R is the responsivity. The responsivities for devices of varying **U3** thickness are shown in Figure 7.8(a). Since the present device is characterized with no external bias, the only internal source of noise that we consider is Johnson-Nyquist noise ($i_{J-N} = \sqrt{(4k_B T \Delta f / R_D)}$) [60], which results from random thermally-induced current fluctuations. Measurements of the R_D for different **U3** thicknesses are also plotted in Figure 7.8(a). The resultant calculations for D* are shown in Figure 7.8(b). Despite the fact that the peak responsivity occurs with a **U3** thickness of 8.1 nm, D* is found to increase monotonically and plateau for greater **U3** thicknesses. The maximum D* achieved is $(4.3 \pm 0.4) \times 10^{11}$ Jones at $\lambda = 756$ nm for the device consisting of a 15 nm-thick **U3** film and a 60 nm MoO_3 film. This performance in photosensitivity approaches that of comparable inorganic technologies. For example, commercially available silicon p-n photodiodes exhibit specific detectivity $>10^{12}$ Jones in the near infrared wavelength range [184].

7.3.5 Response Speed

Finally, we characterize the response speed of the device. A Newport LQA-785 diode laser (3.1 mW cm^{-2} at $\lambda = 785$ nm) was modulated with a square wave from a function generator and the response from the device was recorded on a Tektronix TDS3054B oscilloscope. The frequency roll-off at zero applied bias for a device employing an 8.1 nm **U3** film is shown in Figure 7.8(c). The frequency for which the

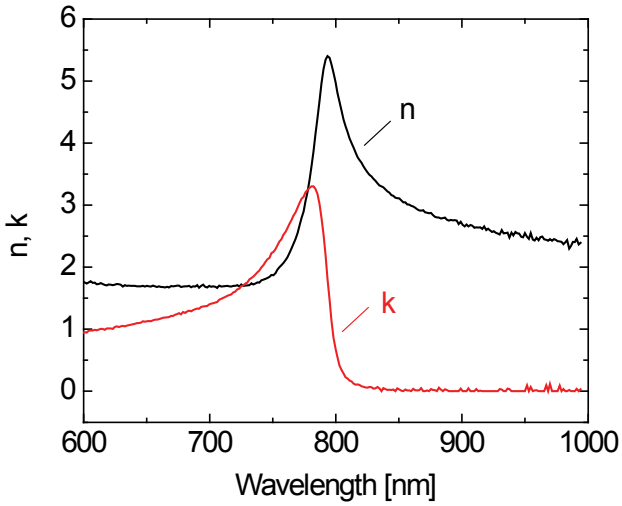

Figure 7.9: Optical constants for spun-cast **U3** films derived from spectroscopic ellipsometry.

response is attenuated by 3-dB is found to be $f_{3dB} = 91.5$ kHz, making the device suitable for a wide range of photodetector applications.

7.4 Optical Modeling to Determine Exciton Diffusion Length

To quantify the exciton diffusion length and to better understand the dependence of device performance on layer thicknesses, experimental EQE data was modeled using the optical transfer matrix formalism coupled with the one-dimensional diffusion equation [98, 185]. Optical constants for **U3** films were measured using a Woollam WVase spectroscopic ellipsometer (see Figure 7.9) and calculations were performed using a custom MATLAB code. The model takes into account optical interference effects within the structure as well as exciton diffusion to an idealized **U3**/ZnO dis-

sociating interface, as described by a parameter for the **U3** exciton diffusion length (L_D). Exciton diffusion lengths were fitted from experimental EQE data using a least-squares algorithm as a function of both **U3** and MoO_3 thickness. We determine the exciton diffusion length within the **U3** film to be $L_D = 2.0 \pm 0.4$ nm (see Figure 7.5(a-b)). We note that EQE data for devices consisting of the two thinnest **U3** films were omitted from this fit as the low performance of these devices is related to degradation of diode rectification (and correspondingly high reverse-bias leakage current), which is not accounted for by our simple model. The data sets representing peak EQE as functions of **U3** thickness and MoO_3 thickness were fit separately and found to be consistent within the reported error. The theoretical EQE as a function of layer thickness, shown in a contour plot in Figure 7.5(c), agrees with our experimental results and suggests that higher EQE could be obtained if **U3** thickness could be reduced further without sacrificing the photovoltaic performance of the device.

We emphasize that the low exciton diffusion length extracted from our model applies for diffusion in the direction normal to the plane of the J-aggregate film. A high exciton diffusion length (>10 nm) is generally expected in J-aggregate materials due to the high degree of crystalline order relative to disordered organic materials [100]. A recent study of exciton-exciton annihilation within a different J-aggregate material, for example, identified L_D in the lateral direction to be greater than 100 nm [177]. The low value for L_D in the present case is likely due to a high degree of directionality in L_D that arises from the lamellar arrangement of the film, with diffusion in the more ordered lateral direction being much more favorable. We note that if J-aggregate systems that possess both large exciton diffusion lengths in the

direction normal to the film and high optical absorption coefficients can be identified, IQEs approaching 100% should be readily achievable in the simple planar architecture described here.

7.5 Conclusion

We have demonstrated a photodetector that employs ZnO and MoO_3 charge transport layers and that is sensitized at near-infrared wavelengths by a thin film of the J-aggregating cyanine dye, **U3**. The magnitude of the EQE is found to be highly sensitive to both the thickness of a MoO_3 optical spacer in the structure as well as to the thickness of the U3 film itself. A maximum specific detectivity of $(4.3 \pm 0.4) \times 10^{11}$ at $\lambda = 756$ nm is obtained for a device consisting of a 15 nm-thick U3 film and a 60 nm MoO_3 film. Modeling of experimental EQE data as a function of layer thicknesses reveals that photocurrent is limited by the diffusion of photo-generated excitons to the ZnO/U3 hetero-interface, and the exciton diffusion length in the U3 film was determined to be $L_D = 2.0 \pm 0.4$ nm. This work provides insights relevant to the use of J-aggregating dyes in photodetector and photovoltaic applications and highlights the importance of engineering the optical field profile within such structures in order to maximize performance.

Chapter 8

Conclusion

8.1 Thesis Summary

This thesis describes the development and detailed characterization of several photodetectors that incorporate colloidal QD and organic semiconductor thin films. Chapter 1 reviews the history of nanostructured NIR/SWIR photodetection. It includes a discussion of potential applications and a comprehensive survey of advancements in the literature. Chapter 2 describes some of the key underlying physics related to the nanostructured materials used in this work, and Chapter 3 describes the experimental techniques that were employed.

In Chapter 4, several SWIR photoconductor structures consisting of PbS QDs are described, and several approaches for improving their performance are investigated. We explored the use of air-annealing treatments to reduce dark current in the QD film and demonstrate that such treatments enable an improvement in photosensitivity. We also introduce an approach for improving the transient response

through the utilization of an organic/QD heterojunction to affect the recombination rate of charge carriers in the device. Specifically, we incorporate a film of the fullerene derivative, [6,6]-phenyl C_{61}-butyric acid methyl ester (PCBM), which creates a type-II hetero-interface with PbS QDs, into a planar PbS QD photoconductor. Fast carrier recombination across the PbS QD/PCBM interface outpaces the slow trap-mediated bulk recombination processes in the QD film, resulting in an improvement in response speed at the expense of photoconductive gain.

The critical importance of charge transport and trapping processes to the performance of QD photoconductors motivates the detailed study of the electronic characteristics of QD films. In Chapter 5, thin films of ethanedithiol-treated PbS QDs are thoroughly investigated in an FET geometry. In particular, we investigate the origin of threshold voltage shifts (bias stress) in top-gated FETs in order to gain insights into the trapping mechanisms present in this system. The FETs exhibit ambipolar operation with typical mobilities on the order of $\mu_e = 8 \times 10^{-3}$ cm^2 V^{-1} s^{-1} in n-channel operation and $\mu_h = 1 \times 10^{-3}$ cm^2 V^{-1} s^{-1} in p-channel operation. When the FET is turned on in n-channel or p-channel mode, the established drain-source current rapidly decreases from its initial magnitude in a stretched exponential decay, manifesting the bias-stress effect. The choice of dielectric is found to have little effect on the characteristics of this bias-stress effect, leading us to conclude that the associated charge trapping process originates within the QD film itself, and not at the dielectric interface. Measurements of bias-stress-induced time-dependent decays in the drain-source current (I_{DS}) are well fit to stretched exponential functions and the time constants of these decays in n-channel and p-channel operation are found

to follow thermally activated (Arrhenius) behavior. Measurements as a function of QD size reveal that the stressing process in n-channel operation is faster for QDs with a smaller core diameter. These observations are consistent with a mechanism in which QD surface-related traps are responsible for the bias-stress effect. This work elucidates aspects of charge transport in chemically treated lead-chalcogenide QD films and is of relevance to on-going investigations toward employing these films in optoelectronic devices.

Chapter 6 introduces a novel lateral heterojunction photoconductor that utilizes an evaporated film of an organic material (spiro-TPD) as a charge transport layer and that is sensitized by the optical response of CdSe QDs. With an electric field of 3.0×10^5 V cm^{-1} applied across the electrodes we measure the external quantum efficiency at the first QD absorption peak (at wavelength $\lambda = 590$ nm) to be 13% corresponding to an internal quantum efficiency of 79%. The advantage of this device structure is that it enables the optical and electronic processes in the photoconductor to be dissociated into different physical layers, which can be independently optimized. It therefore serves as a convenient approach for the realization of photosensitive devices that incorporate absorbing materials with poor electrical characteristics. It is particularly suitable with regard to colloidal QD-sensitized photoconductors, as it obviates the need for aggressive chemical treatments that may compromise the quality of QD surface passivation.

Finally, Chapter 7 presents a photodiode consisting of ZnO and MoO_3 charge transport layers and that is sensitized at NIR wavelengths by a thin film of the J-aggregating cyanine dye, **U3**. The high absorption coefficient of the **U3** film, com-

bined with the use of a reflective anode and optical spacer layer, enables an external quantum efficiency (EQE) of $16.1 \pm 0.1\%$ ($\lambda = 756$ nm) to be achieved at zero-bias in a device consisting of an 8.1 ± 0.3 nm-thick dye film. This is among the highest values of EQE reported for a photovoltaic device that incorporates a neat film of J-aggregating cyanine dye. Modeling of experimental EQE data as a function of layer thicknesses revealed that photocurrent is limited by the diffusion of photo-generated excitons to the ZnO/U3 hetero-interface. The exciton diffusion length in the U3 film was determined to be $L_D = 2.0 \pm 0.4$ nm. This work provides insights relevant to the use of J-aggregating dyes in photodetector and photovoltaic applications and highlights the importance of engineering the optical field profile within such structures in order to maximize performance.

8.2 Outlook and Future Work

Several nanostructured photodetector architectures already exist with key performance metrics that approach those of crystalline inorganic technologies. In particular, PbS and PbSe QD-based photoconductors and photodiodes, as well as several organic-based photodiodes, have been reported with specific detectivities greater than 10^{11} Jones, with a few devices exceeding 10^{12} Jones at infrared wavelengths (see Tables 1.1 and 1.2).

Further improvements in the specific detectivity may be expected as new techniques for increasing responsivity and reducing dark current become established. In the case of photodiodes, future advancements made in the sister field of nanostructured photovoltaics, through the engineering of new active layer materials and device

structures, for example, will likely be directly applicable to efforts to realize high-performance photodiodes. Moreover, the engineering of new materials to serve as blocking layers may enable further reductions in dark current with minimal sacrifice of quantum efficiency [29, 18]. In the case of QD-based photodetectors, one particularly exciting direction is through the use of novel ligand materials. Improved QD surface passivation will likely enable substantial improvements in both detectivity and response speed, as has been shown for CdSe QD-based visible photoconductors [186].

As this field matures, it will become increasingly necessary for groups to collectively adhere to a consistent characterization protocol, in order to ensure meaningful comparisons of device performance. The measurement of specific detectivity, for example, is particularly susceptible to error. It is fairly easy to overestimate responsivity by testing the device under overfill illumination conditions without the use of an aperture to define the device area [101]. Additionally, the assumption of idealized noise sources (i.e. Johnson-Nyquist, Shot, Generation-Recombination, etc.) in the calculation of noise current often results in an underestimation of the total intrinsic noise in the device [104]. These sources of error together may result in a substantial overestimation of the specific detectivity.

Bibliography

[1] S. Kim, Y. T. Lim, E. G. Soltesz, A. M. De Grand, J. Lee, A. Nakayama, J. A. Parker, T. Mihaljevic, R. G. Laurence, D. M. Dor, L. H. Cohn, M. G. Bawendi, and J. V. Frangioni. Near-infrared fluorescent type II quantum dots for sentinel lymph node mapping. *Nat. Biotechnol.*, **22**:93–7, 2004.

[2] J.-E. Källhammer. The road ahead for car night-vision. *Nature Photon.*, **1**:12–13, 2006.

[3] K. Schreiner. Night Vision : Infrared Takes to the Road. *IEEE Comput. Graph.*, pages 6–10, October 1999.

[4] C. Winder, G. Matt, J. C. Hummelen, R. A. J. Janssen, N. S. Sariciftci, and C. J. Brabec. Sensitization of low bandgap polymer bulk heterojunction solar cells. *Thin Solid Films*, **403-404**:373–379, 2002.

[5] L. M. Campos, A. Tontcheva, S. Günes, G. Sonmez, H. Neugebauer, N. S. Sariciftci, and F. Wudl. Extended photocurrent spectrum of a low band gap polymer in a bulk heterojunction solar cell. *Chem. Mater.*, **17**:4031–4033, 2005.

[6] X. Wang, E. Perzon, F. Oswald, F. Langa, S. Admassie, M. R. Andersson, and O. Inganäs. Enhanced photocurrent spectral response in low-bandgap polyfluorene and c_{70}-derivative-based solar cells. *Adv. Funct. Mater.*, **15**:1665–1670, 2005.

[7] F. Zhang, E. Perzon, X. Wang, W. Mammo, M. R. Andersson, and O. Inganäs. Polymer solar cells based on a low-bandgap fluorene copolymer and a fullerene derivative with photocurrent extended to 850 nm. *Adv. Funct. Mater.*, **15**:745–750, 2005.

[8] D. Mühlbacher, M. Scharber, M. Morana, Z. Zhu, D. Waller, R. Gaudiana, and C. Brabec. High photovoltaic performance of a low-bandgap polymer. *Adv. Mater.*, **18**:2884–2889, 2006.

[9] Y. Yao, Y. Liang, V. Shrotriya, S. Xiao, L. Yu, and Y. Yang. Plastic Near-Infrared Photodetectors Utilizing Low Band Gap Polymer. *Adv. Mater.*, **19**:3979–3983, 2007.

[10] X. Gong, M. Tong, Y. Xia, W. Cai, J. S. Moon, Y. Cao, G. Yu, C.-L. Shieh, B. Nilsson, and A. J. Heeger. High-detectivity polymer photodetectors with spectral response from 300 nm to 1450 nm. *Science*, **325**:1665–7, 2009.

[11] R. F. Bailey-Salzman, B. P. Rand, and S. R. Forrest. Near-infrared sensitive small molecule organic photovoltaic cells based on chloroaluminum phthalocyanine. *Appl. Phys. Lett.*, **91**:013508, 2007.

[12] I. H. Campbell. Transparent organic photodiodes with high quantum efficiency in the near infrared. *Appl. Phys. Lett.*, **97**:033303, 2010.

[13] J. B. Wang, W. L. Li, B. Chu, C. S. Lee, Z. S. Su, G. Zhang, S. H. Wu, and F. Yan. High speed responsive near infrared photodetector focusing on 808nm radiation using hexadecafluorocopperphthalocyanine as the acceptor. *Org. Electron.*, **12**:34–38, 2011.

[14] S.-H. Wu, W.-L. Li, B. Chu, Z.-S. Su, F. Zhang, and C. S. Lee. High performance small molecule photodetector with broad spectral response range from 200 to 900 nm. *Appl. Phys. Lett.*, **99**:023305, 2011.

[15] T. P. Osedach, A. Iacchetti, R. R. Lunt, T. L. Andrew, P. R. Brown, G. M. Akselrod, and V. Bulović. Near-Infrared Photodetector Consisting of J-Aggregating Cyanine Dye and Metal Oxide Thin Films. *submitted to Nano Lett.*

[16] H. Bürckstümmer, N. M. Kronenberg, K. Meerholz, and F. Würthner. Near-infrared absorbing merocyanine dyes for bulk heterojunction solar cells. *Org. Lett.*, **12**:3666–9, 2010.

[17] M. Binda, T. Agostinelli, M. Caironi, D. Natali, M. Sampietro, L. Beverina, R. Ruffo, and F. Silvestri. Fast and air stable near-infrared organic detector based on squaraine dyes. *Org. Electron.*, **10**:1314–1319, 2009.

[18] M. Binda, A. Iacchetti, D. Natali, L. Beverina, M. Sassi, and M. Sampietro. High detectivity squaraine-based near infrared photodetector with na/cm^2 dark current. *Appl. Phys. Lett.*, **98**:073303, 2011.

[19] J. D. Zimmerman, V. V. Diev, K. Hanson, R. R. Lunt, E. K. Yu, M. E. Thompson, and S. R. Forrest. Porphyrin-tape/C_{60} organic photodetectors with 6.5% external quantum efficiency in the near infrared. *Adv. Mater.*, **22**:2780–3, 2010.

[20] J. D. Zimmerman, E. K. Yu, V. V. Diev, K. Hanson, M. E. Thompson, and S. R. Forrest. Use of additives in porphyrin-tape/C_{60} near-infrared photodetectors. *Org. Electron.*, **12**:869–873, 2011.

[21] M. S. Arnold, J. D. Zimmerman, C. K. Renshaw, X. Xu, R. R. Lunt, C. M. Austin, and S. R. Forrest. Broad spectral response using carbon nanotube/organic semiconductor/C_{60} photodetectors. *Nano Lett.*, **9**:3354–8, 2009.

[22] S. A. Mcdonald, G. Konstantatos, S. Zhang, P. W. Cyr, E. J. D. Klem, L. Levina, and E. H. Sargent. Solution-processed pbs quantum dot infrared photodetectors and photovoltaics. *Nat. Mater.*, **4**:138–142, 2005.

[23] G. Konstantatos, I. Howard, A. Fischer, Hoogland S., J. Clifford, E. Klem, L. Levina, and E. H. Sargent. Ultrasensitive solution-cast quantum dot photodetectors. *Nature*, **442**:180–183, 2006.

[24] J. P. Clifford, G. Konstantatos, K. W. Johnston, S. Hoogland, L. Levina, and E. H. Sargent. Fast, sensitive and spectrally tuneable colloidal- quantum-dot photodetectors. *Nat. Nanotechnol.*, **4**:3–7, 2009.

[25] K. Szendrei, F. Cordella, M. V. Kovalenko, M. Böberl, G. Hesser, M. Yarema, D. Jarzab, O. V. Mikhnenko, A. Gocalinska, M. Saba, F. Quochi, A. Mura, G. Bongiovanni, P. W. M. Blom, W. Heiss, and M. A. Loi. Solution-Processable Near-IR Photodetectors Based on Electron Transfer from PbS Nanocrystals to Fullerene Derivatives. *Adv. Mater.*, **21**:683–687, 2009.

[26] T. Rauch, M. Böberl, S. F. Tedde, J. Fürst, M. V. Kovalenko, G. Hesser, U. Lemmer, W. Heiss, and O. Hayden. Near-infrared imaging with quantum-dot-sensitized organic photodiodes. *Nature Photon.*, **3**:332–336, 2009.

[27] J. Tang, K. W. Kemp, S. Hoogland, K. S. Jeong, H. Liu, L. Levina, M. Furukawa, X. Wang, R. Debnath, D. Cha, K. W. Chou, A. Fischer, A. Amassian, J. B. Asbury, and E. H. Sargent. Colloidal-quantum-dot photovoltaics using atomic-ligand passivation. *Nat. Mater.*, **10**:765–771, 2011.

[28] X. Jiang, R. D. Schaller, S. B. Lee, J. M. Pietryga, V. I. Klimov, and A. A. Zakhidov. Pbse nanocrystal/conducting polymer solar cells with an infrared response to 2 micron. *J. Mater. Res.*, **22**:2204–2210, 2007.

[29] G. Sarasqueta, K. R. Choudhury, J. Subbiah, and F. So. Organic and Inorganic Blocking Layers for Solution-Processed Colloidal PbSe Nanocrystal Infrared Photodetectors. *Adv. Funct. Mater.*, **21**:167–171, 2011.

[30] O. E. Semonin, J. M. Luther, S. Choi, H.-Y. Chen, J. Gao, A. J. Nozik, and M. C. Beard. Peak external photocurrent quantum efficiency exceeding 100% via meg in a quantum dot solar cell. *Science*, **334**:1530–1533, 2011.

[31] M. Fox. *Optical Properties of Solids*. Oxford University Press, New York, 2001.

[32] J. Tischler, M. S. Bradley, Q. Zhang, T. Atay, A. Nurmikko, and V. Bulović. Solid state cavity QED: Strong coupling in organic thin films. *Org. Electron.*, **8**:94 – 113, 2007.

[33] C. B. Murray, D. J. Norris, and M. G. Bawendi. Synthesis and Characterization of Nearly Monodisperse CdE (E=S, Se, Te) Semiconductor Nanocrystallites. *J. Am. Chem. Soc.*, **115**:8706–8715, 1993.

[34] J.S. Steckel, S. Coe-Sullivan, V. Bulović, and M.G. Bawendi. 1.3μm to 1.55μm Tunable Electroluminescence from PbSe Quantum Dots Embedded within an Organic Device. *Adv. Mater.*, **15**:1862–1866, 2003.

[35] J. Singh. *Semiconductor Devices: Basic Principles*. John Wiley & Sons, New York, 2001.

[36] N. Zhao. *Field-Effect Transistors Based on Microcrystalline Conjugated Polymers*. PhD thesis, University of Cambridge, Cambridge, UK, August 2008.

[37] B. E. A. Saleh and M. C. Teich. *Fundamentals of Photonics*. John Wiley & Sons, New York, 1991.

[38] V. C. Wood. *Electrical Excitation of Colloidally Synthesized Quantum Dots in Metal Oxide Structures*. PhD thesis, Massachusetts Institute of Technology, Cambridge, MA, February 2010.

[39] B.-R. Hyun, Y.-W. Zhong, A. C. Bartnik, L. Sun, H. D. Abruña, F. W. Wise, J. D. Goodreau, J. R. Matthews, T. M. Leslie, and N. F. Borrelli. Electron injection from colloidal PbS quantum dots into titanium dioxide nanoparticles. *ACS Nano*, **2**:2206–2212, 2008.

[40] T. P. I. Saragi, T. Spehr, A. Siebert, T. Fuhrmann-Lieker, and J. Salbeck. Spiro compounds for organic optoelectronics. *Chem. Rev.*, **107**:1011–65, 2007.

[41] Al. L. Efros and M. Rosen. The Electronic Structure of Semiconductor Nanocrystals. *Annu. Rev. Mater. Sci.*, **30**:475–521, 2000.

[42] T. C. Chiang, K. H. Frank, H. J. Freund, A. Goldmann, F. J. Himpsel, U. Karlsson, R. C. Leckey, and W. D. Schneider. Electronic Structure of Solids: Photoemission Spectra and Related Data. In A. Goldmann and E.-E. Koch, editors, *Landolt-Bornstein, New Series*, volume 23. Springer, Berlin, 1989.

[43] P. R. Brown, R. R. Lunt, N. Zhao, T. P. Osedach, D. D. Wanger, L. Y. Chang, M. G. Bawendi, and V. Bulović. Improved Current Extraction from ZnO/PbS Quantum Dot Heterojunction Photovoltaics Using a MoO_3 Interfacial Layer. *Nano Lett.*, **11**:120–126, 2011.

[44] S. R. Forrest. Active Optoelectronics Using Thin-Film Organic Semiconductors. *IEEE J. Sel. Top. Quant.*, **6**:1072–1083, 2000.

[45] M. C. Barr, J. A. Rowehl, R. R. Lunt, J. Xu, A. Wang, C. M. Boyce, S. G. Im, V. Bulović, and K. K. Gleason. Direct Monolithic Integration of Organic Photovoltaic Circuits on Unmodified Paper. *Adv. Mater.*, **23**:3500–3505, 2011.

[46] S. Coe-Sullivan. Quantum dot developments. *Nature Photon.*, **3**:315–316, 2010.

[47] R. R. Lunt, T. P. Osedach, P. R. Brown, J. A. Rowehl, and V. Bulović. Practical Roadmap and Limits to Nanostructured Photovoltaics. *Adv. Mater.*, **23**:5712–5727, 2011.

[48] P. V. Kamat. Quantum Dot Solar Cells. Semiconductor Nanocrystals as Light Harvesters. *J. Phys. Chem. C*, **112**:18737 – 18753, 2008.

[49] A. G. Pattantyus-Abraham, I. J. Kramer, A. R. Barkhouse, X. H. Wang, G. Konstantatos, R. Debnath, L. Levina, I. Raabe, M. K. Nazeeruddin, M. Grätzel, and E. H. Sargent. Depleted-Heterojunction Colloidal Quantum Dot Solar Cells. *ACS Nano*, **4**:3374–3380, 2010.

[50] Y. Liang, Z. Xu, J. Xia, S.-T. Tsai, G. Li, C. Ray, and L. Yu. For the Bright Future - Bulk Heterojunction Polymer Solar Cells with Power Conversion Efficiency of 7.4%. *Adv. Energy Mater.*, **22**:E135 – E138, 2010.

[51] Y. Matsuo, Y. Sato, T. Niinomi, I. Soga, H. Tanaka, and E. Nakamura. Columnar Structure in Bulk Heterojunction in Solution-Processable Three-Layered p-i-n Organic Photovoltaic Devices Using Tetrabenzoporphyrin Precursor and Silylmethyl[60]fullerene. *J. Am. Chem. Soc.*, **131**:16048 – 16050, 2009.

[52] Y. Sun, G. C. Welch, W. L. Leong, C. J. Takacs, G. C. Bazan, and A. J. Heeger. Solution-processed small-molecule solar cells with 6.7% efficiency. *Nat. Mater.*, **11**:44 – 48, 2012.

[53] D. C. Oertel, M. G. Bawendi, A. C. Arango, and V. Bulović. Photodetectors based on treated CdSe quantum-dot films. *Appl. Phys. Lett.*, **87**:213505, 2005.

[54] D. C. Oertel. *Photodetectors Based on Colloidal Quantum Dots*. PhD thesis, Massachusetts Institute of Technology, Cambridge, MA, June 2007.

[55] P. Peumans, V. Bulović, and S. R. Forrest. Efficient, high-bandwidth organic multilayer photodetectors. *Appl. Phys. Lett.*, **76**:3855, 2000.

[56] G. Yu, Y. Cao, J. Wang, J. McElvain, and A. J. Heeger. High sensitivity polymer photosensors for image sensing applications. *Synthetic Met.*, **102**:904 – 907, 1999.

[57] G. Konstantatos and E. H. Sargent. Nanostructured materials for photon detection. *Nat. Nanotechnol.*, **5**:391–400, 2010.

[58] E. H. Sargent. Infrared Quantum Dots. *Adv. Mater.*, **17**:515–522, 2005.

[59] J. Clark and G. Lanzani. Organic photonics for communications. *Nature Photon.*, **4**:438–446, 2010.

[60] A. Rogalski. *Infrared Detectors*. Gordon and Breach, Amsterdam, 2000.

[61] M. Binda, C. Fiorini, A. Iacchetti, D. Natali, V. Pecunia, R. Peloso, M. Sampietro, L. Beverina, and G. Pagani. Squaraine-based Organic Photodetector Coupled to a scintillating Crystal for X-ray Sensing Applications. In *IEEE Nucl. Sci. Conf. R.*, pages 1970–1973, 2009.

[62] M. Binda, D. Natali, M. Sampietro, T. Agostinelli, and L. Beverina. Organic based photodetectors: Suitability for X- and Γ-rays sensing application. *Nucl. Instrum. Meth. A*, **624**:443–448, 2010.

[63] A. L. Washburn and R. C. Bailey. Photonics-on-a-chip: recent advances in integrated waveguides as enabling detection elements for real-world, lab-on-a-chip biosensing applications. *Analyst*, **136**:227–236, 2011.

[64] J. R. Wojciechowski, L. C. Shriver-Lake, M. Y. Yamaguchi, E. Füreder, R. Pieler, M. Schamesberger, C. Winder, H. J. Prall, M. Sonnleitner, and F. S. Ligler. Organic Photodiodes for Biosensor Miniaturization. *Anal. Chem.*, **81**:3455–3461, 2009.

[65] O. Hofmann, P. Miller, P. Sullivan, T. S. Jones, J. C. deMello, D. D. C. Bradley, and A. J. deMello. Thin-film organic photodiodes as integrated detectors for microscale chemiluminescence assays. *Sensor Actuat. B-Chem.*, **106**:878–884, 2005.

[66] X. Wang, O. Hofmann, R. Das, E. M. Barrett, A. J. DeMello, J. C. DeMello, and D. D. C. Bradley. Integrated thin-film polymer/fullerene photodetectors for on-chip microfluidic chemiluminescence detection. *Lab Chip*, **7**:58–63, 2007.

[67] A. Pais, A. Banerjee, D. Klotzin, and I. Papautsky. High-sensitivity, disposable lab-on-a-chip with thin-film organic electronics for fluorescence detection. *Lab Chip*, **8**:794–800, 2008.

[68] O. Hofmann, D. D. C. Bradley, J. C. DeMello, and A. J. DeMello. Lab-on-a-Chip Devices with Organic Semiconductor-Based Optical Detection. In D. A. Bernards, R. M. Owens, and G. G. Malliaras, editors, *Organic Semiconductors in Sensor Applications*, chapter 4, pages 97–140. Springer, Berlin, 2008.

[69] G. Konstantatos, L. Levina, A. Fischer, and E. H. Sargent. Engineering the temporal response of photoconductive photodetectors via selective introduction of surface trap states. *Nano Lett.*, **8**:1446–1450, 2008.

[70] A. C. Arango, D. C. Oertel, Y. Xu, M. G. Bawendi, and V. Bulović. Heterojunction Photovoltaics Using Printed Colloidal Quantum Dots as a Photosensitive Layer. *Nano Lett.*, **9**:860–863, 2009.

[71] S. P. Subbarao, M. E. Bahlke, and I. Kymissis. Laboratory Thin-Film Encapsulation of Air-Sensitive Organic Semiconductor Devices. *IEEE T. Electron Dev.*, **57**:153–156, 2010.

[72] T. W. Kelley, L. D. Boardman, T. D. Dunbar, D. V. Muyres, M. J. Pellerite, and T. P. Smith. High-Performance OTFTs Using Surface-Modified Alumina Dielectrics. *J. Phys. Chem. B*, **107**:5877–5881, 2003.

[73] V. C. Sundar, J. Zaumseil, V. Podzorov, E. Mendard, R. L. Willett, T. Someya, M. E. Gershenson, and J. A. Rogers. Elastomeric Transistor Stamps: Reversible Probing of Charge Transport in Organic Crystals. *Science*, **303**:1644–1646, 2004.

[74] E. E. Jelley. Spectral Absorption and Fluorescence of Dyes in the Molecular State. *Nature*, **138**:1009–1010, 1936.

[75] G. Scheibe. *Angew. Chem.*, **49**, 1936.

[76] R. S. Eachus, A. P. Marchetti, and A. A. Muenter. The Photophysics of Silver Halide Imaging Materials. *Annu. Rev. Phys. Chem.*, **50**:117–144, 1999.

[77] J. Spence. Spectral Sensitization and Special Photographic Materials for Scientific Use. *Appl. Optics*, **11**:4–12, 1972.

[78] T. Tani, K. Seki, K. Yoshihara, and J. Hanna. Thin Organic Layers for Photography and Electronic Devices. *Int. J. Photoenergy*, pages 1–8, 2006.

[79] F. Würthner, T. E. Kaiser, and C. R. Saha-Möller. J-Aggregates: From Serendipitous Discovery to Supramolecular Engineering of Functional Dye Materials. *Angew. Chem. Int. Edit.*, **50**:3376–3410, 2011.

[80] A. P. Alivisatos. Semiconductor Clusters, Nanocrystals, and Quantum Dots. *Science*, **271**:933–937, 1996.

[81] N. N. Ledentsov, V. M. Ustinov, V. A. Shchukin, P. S. Kop'ev, and Zh. I. Alferov. Quantum dot heterostructures: fabrication, properties, lasers (Review). *Semiconductors*, **32**:343–365, 1998.

[82] R. Hanson, L. P. Kouwenhoven, J. R. Petta, S. Tarucha, and L. M. K. Vandersypen. Spins in few-electron quantum dots. *Rev. Mod. Phys.*, **79**:1217–1265, 2007.

[83] N. Zhao, T. P. Osedach, L.-Y. Chang, S. M. Geyer, D. D. Wanger, M. T. Binda, A. C. Arango, M. G. Bawendi, and V. Bulović. Colloidal PbS quantum dot solar cells with high fill factor. *ACS Nano*, **4**:3743 – 3752, 2010.

[84] M. Jarosz, V. Porter, B. Fisher, M. Kastner, and M. Bawendi. Photoconductivity studies of treated CdSe quantum dot films exhibiting increased exciton ionization efficiency. *Phys. Rev. B*, **70**:1–12, 2004.

[85] J. L. Machol and F. W. Wise. Vibronic quantum beats in PbS microcrystallites. *Phys. Rev. B*, **48**:2819–2822, 1993.

[86] S. M. Sze and K. K. Ng. *Physics of Semiconductor Devices*. John Wiley & Sons, Hoboken, 2007.

[87] J. Zaumseil and H. Sirringhaus. Electron and ambipolar transport in organic field-effect transistors. *Chem. Rev.*, **107**:1296–1323, 2007.

[88] D. K. Kim, Y. Lai, T. R. Vemulkar, and C. R. Kagan. Flexible, Low-Voltage, and Low-Hysteresis PbSe Nanowire Field-Effect Transistors. *ACS Nano*, **5**:10074–10083, 2011.

[89] W.-K. Koh, S. R. Saudari, A. T. Fafarman, C. R. Kagan, and C. B. Murray. Thiocyanate-Capped PbS Nanocubes: Ambipolar Transport Enables Quantum Dot Based Circuits on a Flexible Substrate. *Nano Lett.*, **11**:4764–4767, 2011.

[90] A. Salleo, M. L. Chabinyc, M. S. Yang, and R. A. Street. Polymer thin-film transistors with chemically modified dielectric interfaces. *Appl. Phys. Lett.*, **81**:4383, 2002.

[91] A. Virkar, S. Mannsfeld, J. H. Oh, M. F. Toney, Y. H. Tan, G.-Y. Liu, J. C. Scott, R. Miller, and Z. Bao. The role of ots density on pentacene and c_{60} nucleation, thin film growth, and transistor performance. *Adv. Funct. Mater.*, **19**:1962–1970, 2009.

[92] M. Shtein, J. Mapel, J. B. Benziger, and S. R. Forrest. Effects of film morphology and gate dielectric surface preparation on the electrical characteristics of organic-vapor-phase-deposited pentacene thin-film transistors. *Appl. Phys. Lett.*, **81**:268, 2002.

[93] K. K. Ryu, I. Nausieda, D. Da He, A. I. Akinwande, V. Bulović, and C. G. Sodini. Bias-Stress Effect in Pentacene Organic Thin-Film Transistors. *IEEE T. Electron Dev.*, **57**:1003–1008, 2010.

[94] I. Nausieda, K. Ryu, I. Kymissis, A. I. Akinwande, V. Bulović, and C. G. Sodini. An Organic Active-Matrix Imager. *IEEE T. Electron Dev.*, **55**:527–532, 2008.

[95] I. G. Hill. Numerical simulations of contact resistance in organic thin-film transistors. *Appl. Phys. Lett.*, **87**:163505, 2005.

[96] T. J. Richards and H. Sirringhaus. Analysis of the contact resistance in staggered, top-gate organic field-effect transistors. *J. Appl. Phys.*, **102**:094510, 2007.

[97] P. V. Necliudov, M. S. Shur, D. J. Gundlach, and T. N. Jackson. Modeling of organic thin film transistors of different designs. *J. Appl. Phys.*, **88**:6594, 2000.

[98] P. Peumans, A. Yakimov, and S. R. Forrest. Small molecular weight organic thin-film photodetectors and solar cells. *J. Appl. Phys.*, **93**:3693–3723, 2003.

[99] P. Peumans and S. R. Forrest. Separation of geminate charge-pairs at donor-acceptor interfaces in disordered solids. *Chem. Phys. Lett.*, **398**:27–31, 2004.

[100] R. R. Lunt, J. B. Benziger, and S. R. Forrest. Relationship between crystalline order and exciton diffusion length in molecular organic semiconductors. *Adv. Mater.*, **22**:1233–6, 2010.

[101] A. C. Arango. *High open-circuit voltage in heterojunction photovoltaics containing a printed colloidal quantum-dot photosensitive layer*. PhD thesis, Massachusetts Institute of Technology, Cambridge, MA, February 2010.

[102] V. Reipa, G. Purdum, and J. Choi. Measurement of Nanoparticle Concentration Using Quartz Crystal Microgravimetry. *J. Phys. Chem. B*, **114**:16112–16117, 2010.

[103] D. P. Birnie and M. Manley. Combined flow and evaporation of fluid on a spinning disk. *Phys. Fluids*, **9**:870–875, 1997.

[104] S. M. Geyer. *Science and Applications of Infrared Semiconductor Nanocrystals*. PhD thesis, Massachusetts Institute of Technology, Cambridge, MA, September 2010.

[105] E. J. D. Klem, D. D. MacNeil, P. W. Cyr, L. Levina, and E. H. Sargent. Efficient solution-processed infrared photovoltaic cells: Planarized all-inorganic bulk heterojunction devices via inter-quantum-dot bridging during growth from solution. *Appl. Phys. Lett.*, **90**:183113, 2007.

[106] M. Drndić, M. V. Jarosz, N. Y. Morgan, M. a. Kastner, and M. G. Bawendi. Transport properties of annealed CdSe colloidal nanocrystal solids. *J. Appl. Phys.*, **92**:7498–7503, 2002.

[107] V. J. Porter, T. Mentzel, S. Charpentier, M. A. Kastner, and M. G. Bawendi. Temperature-, gate-, and photoinduced conductance of close-packed CdTe nanocrystal films. *Phys. Rev. B*, **73**:24–27, 2006.

[108] V. J. Porter, S. M. Geyer, J. E. Halpert, M. A. Kastner, and M. G. Bawendi. Photoconduction in Annealed and Chemically Treated CdSe / ZnS Inorganic Nanocrystal Films. *J. Phys. Chem. C*, **112**:2308–2316, 2008.

[109] E. J. D. Klem, H. Shukla, S. Hinds, D. D. MacNeil, L. Levina, and E. H. Sargent. Impact of dithiol treatment and air annealing on the conductivity, mobility, and hole density in PbS colloidal quantum dot solids. *Appl. Phys. Lett.*, **92**:212105, 2008.

[110] J. M. Luther, M. Law, Q. Song, C. L. Perkins, M. C. Beard, and A. J. Nozik. Structural, optical, and electrical properties of self-assembled films of PbSe nanocrystals treated with 1,2-ethanedithiol. *ACS Nano*, **2**:271–280, 2008.

[111] M. H. Ettenberg. Solutions for the Electronic Imaging Professional. *Adv. Imaging*, March 2005.

[112] A. E. Elsner, S. A. Burns, J. J. Weiter, and F. C. Delori. Infrared Imaging of Sub-retinal Structures in the Human Ocular Fundus. *Vision Res.*, **36**:191–205, 1996.

[113] Y. T. Lim, S. Kim, A. Nakayama, N. E. Stott, M. G. Bawendi, and J. V. Frangioni. Selection of quantum dot wavelengths for biomedical assays and imaging. *Mol. Imaging*, **2**:50–64, 2003.

[114] S. Hoogland, V. Sukhovatkin, H. Shukla, J. Clifford, L. Levina, and E. H. Sargent. Megahertz-frequency large-area optical modulators at 1.55 micron based on solution-cast colloidal quantum dots. *Optics express*, **16**:6683–6691, 2008.

[115] J. M. Kahn and J. R. Barry. Wireless Infrared Communications. *P. IEEE*, **85**:265–298, 1997.

[116] J. Oh, S. K. Banerjee, and J. C. Campbell. Metal Germanium Metal Photodetectors on Heteroepitaxial Ge-on-Si With Amorphous Ge Schottky Barrier Enhancement Layers. *IEEE Photonic Tech. L.*, **16**:581–583, 2004.

[117] M. Böberl, M.V. Kovalenko, S. Gamerith, E.J.W. List, and W. Heiss. Inkjet-Printed Nanocrystal Photodetectors Operating up to 3μm Wavelengths. *Adv. Mater.*, **19**:3574–3578, 2007.

[118] A. Biebersdorf, R. Dietmüller, A. S. Susha, A. L. Rogach, S. K. Poznyak, D. V. Talapin, H. Weller, T. A. Klar, and J. Feldmann. Semiconductor nanocrystals photosensitize C_{60} crystals. *Nano Lett.*, **6**:1559–1563, 2006.

[119] J. C. Ho, A. Arango, and V. Bulović. Lateral organic bilayer heterojunction photoconductors. *Appl. Phys. Lett.*, **93**:063305, 2008.

[120] T. P. Osedach, S. M. Geyer, J. C. Ho, A. C. Arango, M. G. Bawendi, and V. Bulović. Lateral heterojunction photodetector consisting of molecular organic and colloidal quantum dot thin films. *Appl. Phys. Lett.*, **94**:043307, 2009.

[121] M. V. Jarosz, N. E. Stott, M. Drndic, N. Y. Morgan, M. A. Kastner, and M. G. Bawendi. Observation of bimolecular carrier recombination dynamics in close-packed films of colloidal CdSe nanocrystals. *J. Phys. Chem. B*, **107**:12585–12588, 2003.

[122] T. S. Mentzel, V. J. Porter, S. Geyer, K. MacLean, M. G. Bawendi, and M. A. Kastner. Charge transport in PbSe nanocrystal arrays. *Phys. Rev. B*, **77**:075316, 2008.

[123] M. H. Zarghami, Y. Liu, M. Gibbs, E. Gebremichael, C. Webster, and M. Law. p-Type PbSe and PbS Quantum Dot Solids Prepared with Short-Chain Acids and Diacids. *ACS Nano*, **4**:2475–2485, 2010.

[124] Y. Liu, M. Gibbs, J. Puthussery, S. Gaik, R. Ihly, H. W. Hillhouse, and M. Law. Dependence of Carrier Mobility on Nanocrystal Size and Ligand Length in PbSe Nanocrystal Solids. *Nano Lett.*, **10**:1960–1969, 2010.

[125] M. Law, J. M. Luther, O. Song, B. K. Hughes, C. L. Perkins, and A. J. Nozik. Structural, optical, and electrical properties of PbSe nanocrystal solids treated thermally or with simple amines. *J. Am. Chem. Soc.*, **130**:5974–5985, 2008.

[126] M. S. Kang, A. Sahu, D. J. Norris, and C. D. Frisbie. Size- and Temperature-Dependent Charge Transport in PbSe Nanocrystal Thin Films. *Nano Lett.*, **11**:3887–3892, 2011.

[127] S. J. Zilker, C. Detcheverry, E. Cantatore, and D. M. de Leeuw. Bias stress in organic thin-film transistors and logic gates. *Appl. Phys. Lett.*, **79**:1124–1126, 2001.

[128] H. E. Katz, X. M. Hong, A. Dodabalapur, and R. Sarpeshkar. Organic field-effect transistors with polarizable gate insulators. *J. Appl. Phys.*, **91**:1572–1576, 2002.

[129] A. Salleo, F. Endicott, and R. A. Street. Reversible and irreversible trapping at room temperature in poly(thiophene) thin-film transistors. *Appl. Phys. Lett.*, **86**:263505, 2005.

[130] H. L. Gomes, P. Stallinga, F. Dinelli, M. Murgia, F. Biscarini, D. M. de Leeuw, T. Muck, J. Geurts, L. W. Molenkamp, and V. Wagner. Bias-induced threshold voltages shifts in thin-film organic transistors. *Appl. Phys. Lett.*, **84**:3184–3186, 2004.

[131] R. A. Street, A. Salleo, and M. L. Chabinyc. Bipolaron mechanism for bias-stress effects in polymer transistors. *Phys. Rev. B*, **68**:085316, 2003.

[132] T. Jung, A. Dodabalapur, R. Wenz, and S. Mohapatra. Moisture induced surface polarization in a poly(4-vinyl phenol) dielectric in an organic thin-film transistor. *Appl. Phys. Lett.*, **87**:182109., 2005.

[133] S. G. J. Mathijssen, M. Cölle, H. Gomes, E. C. P. Smits, B. de Boer, I. McCulloch, P. A. Bobbert, and D. M. de Leeuw. Dynamics of Threshold Voltage Shifts in Organic and Amorphous Silicon Field-Effect Transistors. *Appl. Phys. Lett.*, **19**:2785–2789, 2007.

[134] D. Gupta, S. Yoo, C. Lee, and Y. Hong. Electrical-Stress-Induced Threshold Voltage Instability in Solution-Processed ZnO Thin-Film Transistors: An Experimental and Simulation Study. *IEEE T. Electron Dev.*, **58**:1995–2002, 2011.

[135] S. C. Deane, R. B. Wehrspohn, and M. J. Powell. Unification of the time and temperature dependence of dangling-bond-defect creation and removal in amorphous-silicon thin-film transistors. *Phys. Rev. B*, **58**:12625–12628, 1998.

[136] F. R. Libsch and J. Kanicki. Bias-Stress-Induced Stretched-Exponential Time-Dependence of Charge Injection and Trapping in Amorphous Thin-Film Transistors. *Appl. Phys. Lett.*, **62**:1286–1288, 1993.

[137] L. L. Chua, J. Zaumseil, J. F. Chang, E. C. W. Ou, P. K. H. Ho, H. Sirringhaus, and R. H. Friend. General observation of n-type field-effect behaviour in organic semiconductors. *Nature*, **434**:194–199, 2005.

[138] A. Sharma, S. G. J. Mathijssen, E. C. P. Smits, M. Kemerink, D. M. de Leeuw, and P. A. Bobbert. Proton migration mechanism for operational instabilities in organic field-effect transistors. *Phys. Rev. B*, **82**:075322, 2010.

[139] N. B. Pendyala and K. S. R. K. Rao. Identification of surface states in PbS quantum dots by temperature dependent photoluminescence. *J. Lumin.*, **128**:1826–1830, 2008.

[140] D. G. Kim, T. Kuwabara, and M. Nakayama. Photo luminescence properties related to localized states in colloidal PbS quantum dots. *J. Lumin.*, **119-120**:214–218, 2006.

[141] S. Geyer, V. J. Porter, J. E. Halpert, T. S. Mentzel, M. A. Kastner, and M. G. Bawendi. Charge transport in mixed CdSe and CdTe colloidal nanocrystal films. *Phys. Rev. B*, **82**:155201, 2010.

[142] D. S. Ginger and N. C. Greenham. Charge injection and transport in films of CdSe nanocrystals. *J. Appl. Phys.*, **87**:1361–1368, 2000.

[143] J. Aldana, Y. A. Wang, and X. G. Peng. Photochemical instability of CdSe nanocrystals coated by hydrophilic thiols. *J. Am. Chem. Soc.*, **123**:8844–8850, 2001.

[144] S. Jeong, M. Achermann, J. Nanda, S. Ivanov, V. I. Klimov, and J. A. Hollingsworth. Effect of the thiol-thiolate equilibrium on the photophysical properties of aqueous CdSe/ZnS nanocrystal quantum dots. *J. Am. Chem. Soc.*, **127**:10126–10127, 2005.

[145] S. F. Wuister, C. D. M. Donegá, and A. Meijerink. Influence of thiol capping on the exciton luminescence and decay kinetics of CdTe and CdSe quantum. *J. Phys. Chem. B*, **108**:17393–17397, 2004.

[146] J. Gao, J. M. Luther, O. E. Semonin, R. J. Ellingson, A. J. Nozik, and M. C. Beard. Quantum Dot Size Dependent JV Characteristics in Heterojunction ZnO/PbS Quantum Dot Solar Cells. *Nano Lett.*, **11**:1002–1008, 2011.

[147] N. Kawasaki, W. L. Kalb, T. Mathis, Y. Kaji, R. Mitsuhashi, H. Okamoto, Y. Sugawara, A. Fujiwara, Y. Kubozono, and B. Batlogg. Flexible picene thin film field-effect transistors with parylene gate dielectric and their physical properties. *Appl. Phys. Lett.*, **96**:113305, 2010.

[148] Z. Y. Chen, H. Lemke, S. Albert-Seifried, M. Caironi, M. M. Nielsen, M. Heeney, W. M. Zhang, I. McCulloch, and H. Sirringhaus. High Mobility Ambipolar Charge Transport in Polyselenophene Conjugated Polymers. *Adv. Mater.*, **22**:2371–2375, 2010.

[149] M. S. Kang, J. Lee, D. J. Norris, and C. D. Frisbie. High Carrier Densities Achieved at Low Voltages in Ambipolar PbSe Nanocrystal Thin-Film Transistors. *Nano Lett.*, **9**:3848–3852, 2009.

[150] K. S. Leschkies, M. S. Kang, E. S. Aydil, and D. J. Norris. Influence of Atmospheric Gases on the Electrical Properties of PbSe Quantum-Dot Films. *J. Phys. Chem. C*, **114**:9988–9996, 2010.

[151] B. O'Regan and M. Grätzel. A low-cost, high-efficiency solar cell based on dye-sensitized colloidal TiO_2 films. *Nature*, **353**:737 – 740, 1991.

[152] W. U. Huynh, J. J. Dittmer, and A. P. Alivisatos. Hybrid nanorod-polymer solar cells. *Science*, **295**:2425–2427, 2002.

[153] D. J. Milliron, I. Gur, and A. P. Alivisatos. Hybrid OrganicNanocrystal Solar Cells. *MRS Bull.*, **30**:41–44, 2005.

[154] T. Zukawa, S. Naka, H. Okada, and H. Onnagawa. Organic heterojunction phototransistor. *J. Appl. Phys.*, **91**:1171, 2002.

[155] T. P. I. Saragi and J. Salbeck. Organic heterostructure field-effect transistors using C_{60} and amorphous spirolinked compound. *Appl. Phys. Lett.*, **89**:253516, 2006.

[156] C. A. Leatherdale, C. R. Kagan, N. Y. Morgan, S. A. Empedocles, M. A. Kastner, and M. G. Bawendi. Photoconductivity in CdSe quantum dot solids. *Phys. Rev. B*, **62**:2669 – 2680, 2000.

[157] D. Yu, C. Wang, and P. Guyot-Sionnest. n-Type conducting CdSe nanocrystal solids. *Science*, **300**:1277–80, 2003.

[158] L. Kim. Deposition of colloidal quantum dots by microcontact printing for led display technology. Master's thesis, Massachusetts Institute of Technology, Cambridge, MA, February 2006.

[159] L. Kim, P. O. Anikeeva, S. A. Coe-Sullivan, J. S. Steckel, M. G. Bawendi, and V. Bulović. Contact printing of quantum dot light-emitting devices. *Nano Lett.*, **8**:4513–4517, 2008.

[160] A. Rose. Space-Charge-Limited Currents in Solids. *Phys. Rev.*, **97**:1538–1544, 1955.

[161] M. A. Lampert. Simplified Theory of Space-Charge-Limited Currents in an Insulator with Traps. *Phys. Rev.*, **103**:1648 – 1656, 1956.

[162] A. K. Ghosh and T. Feng. Merocynanine organic solar cells. *J. Appl. Phys.*, **49**:5982, 1978.

[163] N. Karl, A. Bauer, J. Holzäpfel, J. Marktanner, M. Möbus, and F. Stölzle. Efficient organic photovoltaic cells. *Mol. Cryst. Liq. Cryst.*, **252**:243–259, 1994.

[164] P. E. Keivanidis, S. H. Khong, P. K. H. Ho, N. C. Greenham, and R. H. Friend. All-solution based device engineering of multilayer polymeric photodiodes: Minimizing dark current. *Appl. Phys. Lett.*, **94**:173303, 2009.

[165] S. C. B. Mannsfeld, B. C.-K. Tee, R. M. Stoltenberg, C. V. H.-H. Chen, S. Barman, B. V. O. Muir, A. N. Sokolov, C. Reese, and Z. Bao. Highly sensitive flexible pressure sensors with microstructured rubber dielectric layers. *Nat. Mater.*, **9**:859–864, 2010.

[166] F. Würthner and K. Meerholz. Systems chemistry approach in organic photovoltaics. *Chem.-Eur. J.*, **16**:9366–9373, 2010.

[167] M.S. Bradley, J.R. Tischler, and V. Bulović. Layer-by-Layer J-Aggregate Thin Films with a Peak Absorption Constant of 106 cm^1. *Adv. Mater.*, **17**:1881–1886, 2005.

[168] A. Ehret, L. Stuhl, and M. T. Spitler. Spectral Sensitization of TiO_2 Nanocrystalline Electrodes with Aggregated Cyanine Dyes. *J. Phys. Chem. B*, **105**:9960–9965, 2001.

[169] Kazuhiro Sayama, Shingo Tsukagoshi, Kohjiro Hara, Yasuyo Ohga, Akira Shinpou, Yoshimoto Abe, Sadaharu Suga, and Hironori Arakawa. Photoelectrochemical Properties of J Aggregates of Benzothiazole Merocyanine Dyes on a Nanostructured TiO_2 Film. *J. Phys. Chem. B*, **106**:1363–1371, 2002.

[170] T. Horiuchi, H. Miura, K. Sumioka, and S. Uchida. High efficiency of dye-sensitized solar cells based on metal-free indoline dyes. *J. Am. Chem. Soc.*, **126**:12218–9, 2004.

[171] X. Chen, J. Guo, X. Peng, M. Guo, Y. Xu, L. Shi, C. Liang, L. Wang, Y. Gao, and S. Sun. Novel cyanine dyes with different methine chains as sensitizers for nanocrystalline solar cell. *J. Photoch. Photobio. A*, **171**:231–236, 2005.

[172] K. Saito. Sensitization of the Photocurrent in C_{60} / Merocyanine J-Aggregate Heterojunction Photovoltaic Cells. *Jpn. J. Appl. Phys.*, **38**:1140–1142, 1999.

[173] M. Kawasaki and S. Aoyama. High efficiency photocurrent generation by two-dimensional mixed J-aggregates of cyanine dyes. *Chem. Commun.*, **1**:988–9, 2004.

[174] F. Meng, J. Hua, K. Chen, H. Tian, L. Zuppiroli, and F. Nüesch. Synthesis of novel cyanine-fullerene dyads for photovoltaic devices. *J. Mater. Chem.*, **15**:979–986, 2005.

[175] F. Nüesch, G. Tornare, L. Zuppiroli, F. Meng, K. Chen, and H. Tian. Interface modification to optimize charge separation in cyanine heterojunction photovoltaic devices. *Sol. Energ. Mat. Sol. C.*, **87**:817–824, 2005.

[176] B. J. Walker, A. Dorn, V. Bulović, and M. G. Bawendi. Color-selective photocurrent enhancement in coupled J-aggregate/nanowires formed in solution. *Nano Lett.*, **11**:2655–9, 2011.

[177] G. Akselrod, Y. Tischler, E. Young, D. Nocera, and V. Bulović. Exciton-exciton annihilation in organic polariton microcavities. *Phys. Rev. B*, **82**:1–4, 2010.

[178] J. Wenus, S. Ceccarelli, D. Lidzey, A. Tolmachev, J. Slominskii, and J. Bricks. Optical strong coupling in microcavities containing J-aggregates absorbing in near-infrared spectral range. *Org. Electron.*, **8**:120–126, 2007.

[179] B. Dandrade, S. Datta, S. Forrest, P. Djurovich, E. Polikarpov, and M. Thompson. Relationship between the ionization and oxidation potentials of molecular organic semiconductors. *Org. Electron.*, **6**:11–20, 2005.

[180] P. I. Djurovich, E. I. Mayo, S. R. Forrest, and M. E. Thompson. Measurement of the lowest unoccupied molecular orbital energies of molecular organic semiconductors. *Org. Electron.*, **10**:515–520, 2009.

[181] R. R. Lunt and V. Bulović. Transparent, near-infrared organic photovoltaic solar cells for window and energy-scavenging applications. *Appl. Phys. Lett.*, **98**:113305, 2011.

[182] J. R. Tischler, M. S. Bradley, and V. Bulović. Critically coupled resonators in vertical geometry using a planar mirror and a 5 nm thick absorbing film. *Opt. Lett.*, **31**:2045–7, 2006.

[183] R. H. Bube and A. L Fahrenbruch. *Advances in Electronics and Electron Physics*. Academic, New York, 1981.

[184] A. Rogalski. Optical detectors for focal plane arrays. *Opto-Electron. Rev.*, **12**:221–245, 2004.

[185] L. A. A. Pettersson, L. S. Roman, and O. Inganäs. Modeling photocurrent action spectra of photovoltaic devices based on organic thin films. *J. Appl. Phys.*, **86**:487–496, 1999.

[186] J.-S. Lee, M. V. Kovalenko, J. Huang, D. S. Chung, and D. V. Talapin. Band-like transport, high electron mobility and high photoconductivity in all-inorganic nanocrystal arrays. *Nat. Nanotechnol.*, **6**:348 – 352, 2011.